TRIBOCHEMICAL STUDIES OF HARD CARBON FILMS AS A FUNCTION OF LOAD AND ENVIRONMENT

Andrew Robert Konicek

A DISSERTATION

in

Physics and Astronomy

Presented to the Faculties of the University of Pennsylvania

in

Partial Fulfillment of the Requirements for the

Degree of Doctor of Philosophy

2010

Supervisor of Dissertation

Signature_____

Robert Carpick, Professor, Mechanical Engineering and Applied Mechanics

Graduate Group Chairperson

Signature_____

Ravi Sheth, Professor, Physics and Astronomy

A.T. Charlie Johnson, Professor, Physics and Astronomy, Committee Chair
Jay Kikkawa, Associate Professor, Physics and Astronomy
Andrea Liu, Professor, Physics and Astronomy
Dan Gianola, Assistant Professor, Materials Science and Engineering

TRIBOCHEMICAL STUDIES OF HARD CARBON FILMS AS A FUNCTION OF LOAD AND ENVIRONMENT

Acknowledgements

This work was supported by the Air Force Office of Scientific Research under contract number FA9550-05-1-0204, and the US Department of Energy, BES-Materials Sciences, under Contracts DE-FG02-02ER46016 and W-13-109-ENG-38.

I acknowledge Dr. Tom Friedmann and Dr. John Sullivan (Sandia National Laboratory) for growing ta-C films.

I acknowledge John Jacobs for his help with XPS and AFM systems training in the Materials Science & Engineering department at UW-Madison.

I acknowledge Mary Severson and Mark Bissen for their help taking NEXAFS data at the Synchrotron Radiation Center.

I acknowledge Rebecca Metzler and Dr. Mike Abrecht for their help with PEEM measurements at the Synchrotron Radiation Center.

I acknowledge Dr. John Carlisle (Advanced Diamond Technologies), and Dr. Anirudha Sumant and Dr. Orlando Auciello (Argonne National Laboratory), for their help providing UNCD samples, and for informative interactions about the characterization and analysis of diamond materials.

I acknowledge Dr. Andreas Schöll and Dr. Andrew Doran for their help taking PEEM data at the Advanced Light Source.

I acknowledge my former group members at UW-Madison, namely Dr. Rachel Cannara, Dr. Erin Flater, Dr. Guoquing Ning, Dr. Nick Smith, Dr. In-Ha Sung, Sean O'Conner, Patrick Heaney, Kevin Gotrik, Jingjing Liu, and Christopher Torres.

I acknowledge my fellow group members at UPenn, namely Dr. Jason Bares, Dr. Christian Greiner, Dr. Matthew Hamilton, Dr. Qunyang Li, Dr. Papot Jaroenapibal, Dr. Hsao Wei Yap, Vivek Adiga, Evan Dvorak, Sina Ghassemi, Tevis Jacobs, Vahid Vahdat, and Graham Wabiszewski.

I acknowledge the good friends who have supported me and kept me ~sane all these years. Thanks to Shawn, Lindsay, Kate, Scott, Dave, Matt, Kelly, Rebecca, Bo, and Brianna.

I acknowledge my previous co-advisor, Prof. Pupa Gilbert, for introducing me to the world of PEEM and motivating me to accomplish more than I thought possible of myself.

I acknowledge my long-time co-worker, Dr. David Grierson. Thanks for teaching me how to be a graduate researcher. Thanks for learning Matlab with me. Thanks for knowing more about math than any one human should. Thanks for the weeks of travel, the days (in a row) spent in synchrotrons, and thanks for always saying the most inappropriate thing at the most inappropriate time.

I acknowledge my advisor, Prof. Robert Carpick. What can I say? I wouldn't be where I am today if not for all of your patient and amazing guidance. Thank you for all the opportunities, the support, the encouragement, the rare kick in the pants. I've always thought it was a happy accident, my coming to work for you. But I can't imagine the last five years having gone any better. I will be forever grateful.

ABSTRACT

TRIBOCHEMICAL STUDIES OF HARD CARBON FILMS AS A FUNCTION OF LOAD AND ENVIRONMENT

Andrew Robert Konicek

Robert William Carpick

Hydrogen-free, hard carbon thin films are exciting material coatings candidates as solid lubricants. Two examples, ultrananocrystalline diamond (UNCD) and tetrahedral amorphous carbon (ta-C), are particularly promising, because their exceptional mechanical and tribological properties are combined with extremely smooth surfaces. However, their tribological performance can be seriously affected by variations in humidity. These materials do not perform well in vacuum or inert environments. The mechanisms controlling the friction and wear of UNCD and ta-C are not well understood because of a fundamental lack of physical understanding of the surface interactions.

The aim of this thesis is to elucidate the fundamental mechanisms of friction and wear in UNCD and ta-C films. An experimental protocol is defined to examine the relationship between the sliding environment, tribological performance, and mechanical and chemical changes to the films. Self-mated reciprocating tribometry in controlled environments measure UNCD and ta-C friction as a function of load and relative humidity (RH). Scanning white light interferometry measures the post-mortem height profile. Finally, chemical changes inside the wear track are characterized by x-ray photoelectron emission microscopy combined with near-edge x-ray absorption fine structure (X-PEEM-NEXAFS) spectromicroscopy. Results for ta-C and UNCD show that

both films, like single crystal diamond, perform better at lower loads or with higher amounts of RH in the environment. Previous hypotheses for this suggested that lubrication for these films either comes in the form of graphitization (converting carbon from diamond-type bonding to graphite-like bonding) or by passivation (the termination of broken carbon bonds by species in the environment, such as water). All spectroscopic evidence shows no evidence of graphitization, but support the passivation hypothesis. Furthermore, the spectroscopy shows that the passivation is in the form of hydroxyl groups, most likely from water. This affects the run-in (period at the start of sliding of high friction as asperities are being smoothed) behavior of these films. The level of passivation also controls whether the films have high or low friction.

TABLE OF CONTENTS

List of Tables

List of Figures

List of Abbreviations

a-C – amorphous carbon

a-C:H – hydrogenated amorphous carbon

ALS – Advanced Light Source

CCD – charge-wcoupled device

CVD – chemical vapor deposition

DI – deionized

DLC – diamond-like carbon

EXAFS – extended x-ray absorption fine structure

FOV – field of view

GUI – graphical user interface

HFCVD – hot filament chemical vapor deposition

HOPG – highly oriented pyrolitic graphite

MCD – microcrystalline diamond

MCP – microchannel plate

MPCVD – microwave plasma chemical vapor deposition

NCD – nanocrystalline diamond

NEXAFS – near-edge x-ray absorption fine structure

NSLS – National Synchrotron Light Source

PECVD – plasma enhanced chemical vapor deposition

PEEM – photoelectron emission microscopy

PEY – partial electron yield

PIID – plasma immersion ion deposition

PLD – pulsed laser deposition

RH – relative humidity

ROI – region of interest

SRC – Synchrotron Radiation Center

SWLI – scanning white light interferometry

ta-C – tetrahedral amorphous carbon

TEM – transmission electron microscopy

TEY – total electron yield

UNCD – ultrananocrystalline diamond

XANES – x-ray absorption near-edge spectroscopy

XPS – x-ray photoelectron spectroscopy

List of Symbols (Latin characters)

d	sliding distance
F	normal force
K	wear rate
V	worn volume

List of Symbols (Greek characters)

μ	friction coefficient
π	denotes pi chemical bonding
π*	denotes pi chemical antibonding
σ	denotes sigma chemical bonding
σ*	denotes sigma chemical antibonding

1. Introduction

1.1 Study of Friction

Tribology is the study of two bodies in contacting, relative motion, and requires knowledge of a vast and varied number of disciplines to fully comprehend [1.1]. Thermodynamics, solid state physics, mechanics, chemistry, and statistical analysis are just a few examples. Considering how persistent tribological challenges have been for mankind (from the discovery of fire and the building of the pyramids to engineering components for satellites in outer space) [1.2], there is still a tremendous amount to be understood about many of the fundamental problems that arise due to adhesion, friction, and wear. In fact, there is a lack of quantitative models that predict macroscopic friction coefficients and wear rates between surfaces given their material type(s), contact geometry, load, sliding speed, and environmental conditions. Friction also varies at different length scales. Single asperities at the nanoscale have a much different tribological behavior than multiple asperities at the macroscale, even for similar materials and environmental conditions [1.3]. Because tribological interfaces are sensitive to sliding conditions (*e.g.*, applied load, contact geometry, sliding velocity, chemical environment), it can often be difficult to perform an experiment in which only one of these variables is carefully controlled and studied. Therefore, experimental design and control is a crucial component of studying any tribological system.

The main goal of this thesis is to discover, explore, and understand fundamental friction and wear mechanisms in ultrastrong carbon-based thin film materials. Potential benefits of this understanding include developing and implementing new technologies (such as microelectromechanical system devices that have contacting, sliding parts) that would have been previously unfeasible because of issues with friction and wear, as well as making existing tribological systems (such as atomic force microscope probes, which can be coated with carbon films) run substantially more efficiently over longer lifetimes.

A major problem in many mechanical systems is energy loss due to friction. Furthermore, as these systems wear and fatigue they break down, which costs time and money to repair or replace. Dr. H. Peter Jost, who chaired the panel that first coined the term 'tribology,' made initial estimates that approximately one percent of the United Kingdom's gross national product could be saved "…by better application of tribological principles and practices." [1.4] Current estimates are as high as two to seven percent [1.5, 6], which for the United States would mean ~$290 billion to over $1 trillion saved, annually. Understanding the way tribological mechanisms work will also aid in developing and designing new technologies, as well as ensuring that mechanical systems suffer fewer losses in efficiency due to friction, have lower wear, and stay operable over a longer lifetime.

Moreover, the lack of fundamental insight into such a common phenomenon presents a remarkable opportunity for scientific exploration. What are the underlying mechanisms that cause friction? How does friction depend on chemical and mechanical

material properties? Can friction be controlled simply by changing the environmental conditions?

Overall, the study of tribology presents a compelling and scientific challenge that has important implications for many technologies and for multiple fields of science and engineering.

1.2 The Ultimate Tribological Material

There are a seemingly infinite number of tribological pairings that could be studied. Thus, it is important to study systems that, while interesting in and of themselves, in the long run will provide a larger benefit beyond simply the immediate knowledge gained. Single crystal diamond is the hardest and stiffest material known, has the highest thermal conductivity, and the highest acoustic velocity [1.7]. It also has excellent optical properties which can be tuned given the right type and quantity of dopants [1.8, 9]. Undoped single crystal diamond is an insulator, but doping with boron or nitrogen can change the electrical properties and increase the conductivity.

In addition to examining its exceptional mechanical characteristics [1.10], the tribological properties of diamond have also been studied. Tools such as diamond cutting wheels or diamond-embedded scaifes are used to shape and polish materials with high hardness, including diamond itself. The friction of single crystal diamond is anisotropic, varying depending on the crystal face and sliding direction. Friction also depends on the sliding environment (*i.e.*, vacuum, ambient, or water). It was already known from previous work that certain facets of diamond were easier to polish than others. Dennings performed experiments to quantitatively compare the relative hardness of polishing

diamond on different facets along all possible directions of that facet [1.11]. He found that the relative frictional hardness between the test sample and a reference (measured simultaneously) varied by 2-2.5 orders of magnitude for the two facets studied. Scientists, as well as researchers in the diamond industry, explained this by considering diamond to have a 'grain'. Certain facets are easily polished as long as the proper polishing direction with respect to the grain is chosen [1.12, 13].

When studying the environmental dependence, Bowden *et al.* found that removing the native surface layer on a diamond sample by heating the sample in medium vacuum increased the friction coefficient by approximately one order of magnitude [1.14]. Introducing pure oxygen reduced friction by forming an adsorbed oxide layer, and this effect was mostly (but not entirely) reversible just by increasing the vacuum again. They explained this by suggesting there must be some physisorbed oxygen on top of the chemisorbed layer. The physisorbed layer, which can be removed by increasing vacuum, has a large effect on the friction. Bowden *et al.* also showed that similar behavior was seen for diamond when performing tribometry tests in ultrahigh vacuum [1.15].

Utilizing single crystal diamond in many applications is not feasible. However, recent advances in the last few decades have developed the ability to grow carbon-based films in thin film form that share many, if not most, of the advantageous properties of diamond [1.16-20]. One obvious way to improve an existing tribological system is by coating the components with a material that has superior tribological properties [1.21]. Sumant *et al.* found that a 2 μm thick coating of ultrananocrystalline diamond reduced friction, lowered wear, and improved the overall performance and life span of pump

seals. Other films comprised of carbon with a moderate-to-high fraction of 'diamond-like' bonding have been shown to have extreme properties, such as low friction coefficients, low wear rates, and chemical inertness, that make them ideal coating candidates, especially when compared to many known materials [1.22-26]. The mechanical and tribological properties depend on the exact composition, morphology, and topology of the material. To this end, this thesis will focus on carbon-based material systems that are considered to be diamond or diamond-like, the varieties of which are discussed next.

1.3 Approaching the Ideal

1.3.1 Categories of Carbon Films

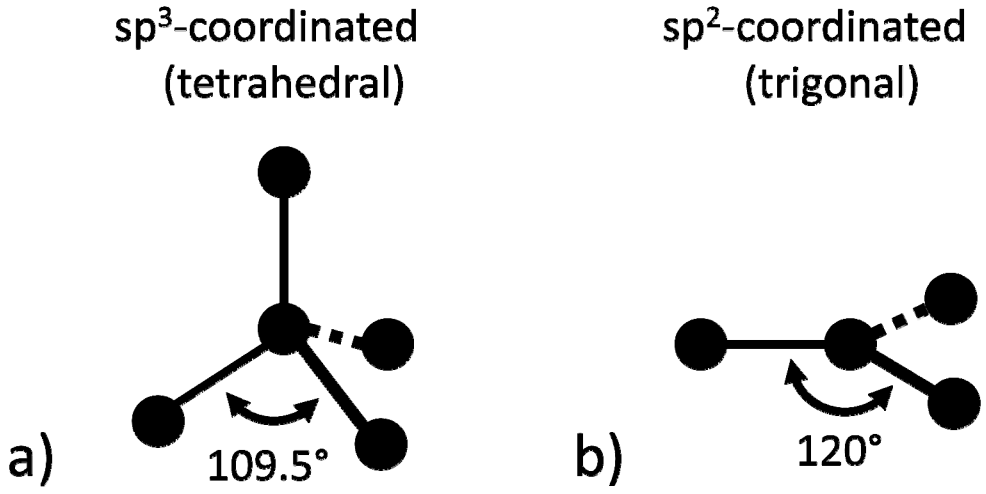

Fig. 1.1: Schematic showing a) tetrahedrally bonded (sp^3-bonded) atoms, such as those found in single crystal diamond, and b) trigonally bonded (sp^2-bonded) atoms, such as those found in highly oriented pyrolytic graphite (HOPG).

Fig. 1.1 is a schematic of the two types of bonding that carbon films are primarily comprised. Carbon atoms have four valence electrons that can form covalent bonds.

There are two electrons in the 2*s* shell and two electrons in the 2*p* shell ($2s^2 2p^2$). When these four electrons form four covalent bonds, the electronic orbitals are said to have *rehybridized* such that the one 2*s* orbital mixes with the three 2*p* orbitals to form four equivalent sp^3-hybridized orbitals. Each of these four orbitals points from the C atom toward the corners of a tetrahedron, with the bond angle between any two bonds being ~109.5°. These bonds are called sigma (σ) bonds because they have an *s* orbital shape when viewed along the bond direction. If only three bonds are formed, the one 2*s* orbital mixes with just two of the 2*p* orbitals to form three sp^2 orbitals. Each orbital points from the C atom toward the corners of an equilateral triangle, with the bond angle between any two bonds being 120°. The remaining electron occupies the unfilled *p* orbital. If this half-filled *p* orbital interacts with another half-filled *p* orbital of a nearby sp^2 bonded carbon atom, as it does in graphite, the bond is referred to as a pi (π) bond. The name comes from the bond shape, as the bond looks like a *p* orbital when viewed along the bond direction, and the bonding direction is not along the orbital direction. Atoms that share both a σ and a π bond are bonded more strongly than atoms that just share a σ bond, due to a stronger overlap of electronic orbitals. The bond length between these atoms is also shorter, as can be seen when comparing the bond length of highly oriented pyrolitic graphite (HOPG), 0.142 nm, with that of single crystal diamond, 0.154 nm. The Young's modulus of graphite, in-plane, is found to be 1 TPa [1.27, 28], similar to diamond. However, in comparison, the out-of-plane modulus for graphite is extremely low. Graphite planes are only weakly bonded to each other through van der Waals forces, and this weak interaction allows them to easily compress, separate, and slip over each other.

It is this behavior that makes graphite such a good solid lubricant. The lack of any weak bonding direction in diamond leads to a directionally-averaged bulk modulus that is much higher than that of graphite. Because of this, films with a higher ratio of sp^2-bonded carbon generally have a lower Young's modulus and lower hardness than those with a higher fraction of sp^3-bonded carbon. For these materials, the order of the Young's modulus and hardness, from lowest to highest, would be amorphous carbon (a-C) and diamond-like carbon (DLC), tetrahedral amorphous carbon (ta-C), and then polycrystalline diamond.

Carbon films can be separated into two broad categories based on their composition and the environments in which they best perform: hydrogenated and non-hydrogenated (H-free) films. Fig. 1.2 is a ternary diagram (adapted from [1.29]) with the corners representing the fraction of sp^2-bonded carbon, fraction of sp^3-bonded carbon, and at.% hydrogen.

Hydrogenated films, which intentionally have hydrogen incorporated as part of the deposition process, typically perform best in inert or vacuum environments [1.30-33]. They are amorphous and have considerable fractions of sp^2-bonded (graphite-like), with the remaining fraction being mostly sp^3-bonded (diamond-like) carbon. Examples of hydrogenated films include DLC and hydrogenated amorphous carbon (a-C:H) (Fig. 1.2, shown at the center).

Non-hydrogenated films, that is, materials with very little or no hydrogen, perform better in environments with a significant partial pressure of hydrogen, oxygen, water vapor, or some other reactive species [1.34-37]. They include both polycrystalline

and amorphous films, and, while they can be amorphous with a significant fraction of sp^2-bonded carbon, the best films, tribologically (highest hardness, lowest wear), have a high fraction of sp^3-bonded carbon. Examples of H-free films with a high fraction of sp^3-bonded carbon include ultrananocrystalline diamond (UNCD) and ta-C (Fig. 1.2).

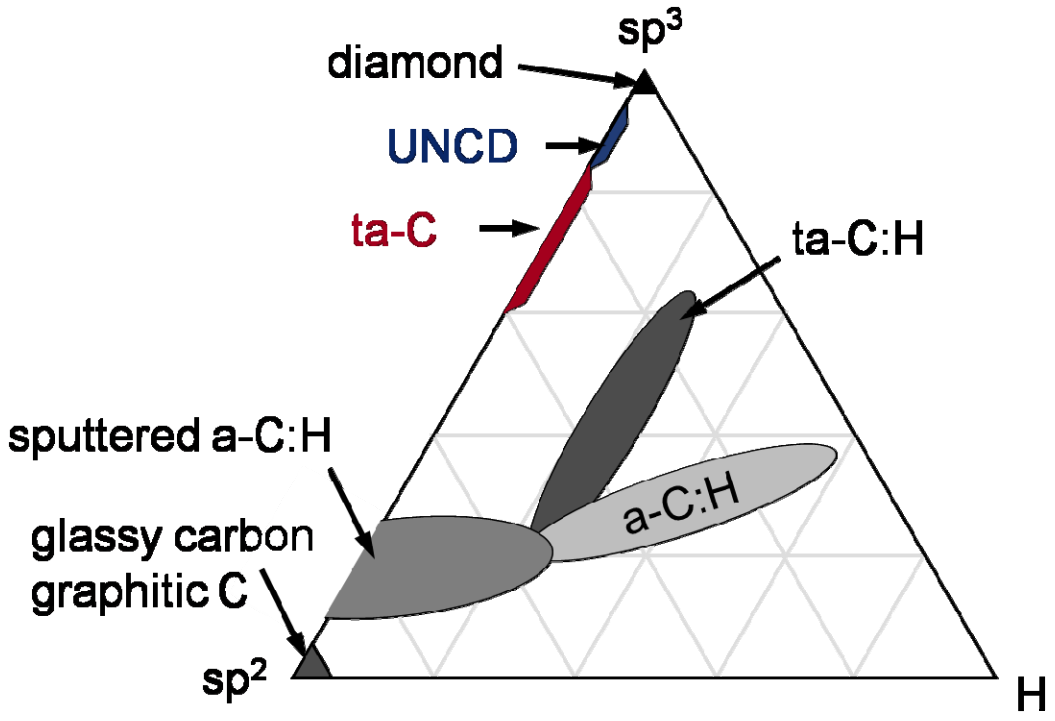

Fig. 1.2: Adapted ternary diagram from [1.38] showing different types of carbon films.

1.3.2 Hydrogenated Films

DLC and a-C:H films can be deposited with a variety of techniques that utilize different conditions and various source gases. The earliest work with these films was in 1971, by Aisenberg and Chabot [1.39]. Hydrogenated carbon films find applications as coatings for razor shaving blades, some components in car engine parts, and, most

notably, as the protective coating on computer hard drives. Common growth techniques include plasma enhanced chemical vapor deposition (PECVD), plasma immersion ion deposition (PIID) ion bombardment, cathodic vacuum arc, pulsed laser deposition, and sputtering [1.40]. The attribute shared by all of these methods is that low energy carbon or hydrocarbon ions are accelerated and deposited onto the surface of the substrate, which leads to the growth of a continuous film. For PECVD and PIID, a source gas, such as acetylene, is used to form a plasma which then condenses onto the substrate. The other techniques utilize a carbon target (usually graphite) as the source material which is then sputtered or ablated to generate carbon ions that are directed toward the substrate. Hydrogen may also be added to some of these systems (or more heavily hydrogenated source gases used) to increase the amount of H in the film. Depositions are typically done at room temperature, though changing the substrate temperature can affect the film properties by changing the energy and mobility of the deposited species.

Because the films are grown from ions impacting into the surface, it is possible that there can be residual stress present in the as-grown film. However, for most techniques there exists a “sweet spot” where the ions have enough energy to both be incorporated into the film and also have the mobility to find a low stress bonding environment. The films are grown in a partial vacuum so that the ionized species will have a longer mean free path. These types of films also have a relatively slow growth rate, meaning they can be grown with extremely good control over the thickness even at the level of a few nanometers (which is important for the hard drive application), and are highly conformal with the substrate. Due to the amorphous nature of the film, and the

growth kinetics, the as-grown film surfaces are very smooth [1.41]. DLC and a-C:H films typically have a high fraction of hydrogen (30-50 at.%) [1.42] incorporated with the carbon atoms (Fig. 1.3). These films are only stable up to 300-400 ºC, after which the hydrogen in the film begins to desorb and the film structure changes [1.43, 44]. Silicon can be doped into a-C:H structures to improve the thermal stability [1.45]. Studies have shown that there is both atomic hydrogen and H_2 molecules that are unbound and trapped inside the material [1.46]. There is also a significant fraction of sp^2-bonded carbon in these films.

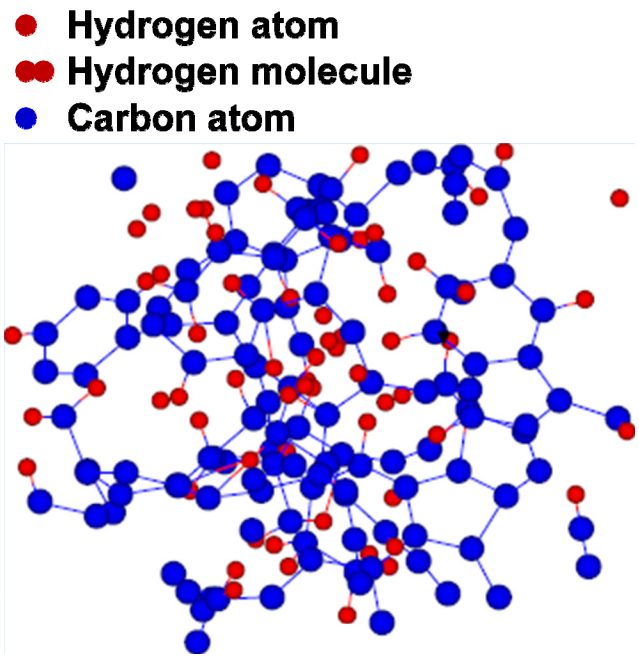

Fig. 1.3: Molecular dynamics simulation of the bonding and structure of a hydrogenated DLC film [1.47]. The lines represent bonds.

Hydrogenated films typically perform best in vacuum or inert environments. Hydrogen in these films is responsible for the low friction, as dangling carbon bonds

formed during sliding are quickly passivated by available hydrogen [1.48]. As shear stresses and wear break carbon bonds on the surface, the hydrogen in the film migrates to the surface. This passivates the dangling bonds, inhibiting them from bonding across the interface, and reduces friction and wear [1.49]. It has been shown that if the surface of the film has a lower hydrogen concentration, or if the hydrogen in that region is depleted (thermally, by wear, or by diffusion) then the friction will increase. This was demonstrated by Eryilmaz *et al.*, who deposited H-free DLC films and then tested their friction performance before and after treating the surface with hydrogen plasma [1.50]. The as-grown films had a friction coefficient of 0.1 and the film was worn through after ~12 m of sliding. After 3 min. of hydrogen plasma treatment on the same surfaces, the friction coefficient was ~0.02 and lasted for over 400 m of sliding. Also supporting this hypothesis, performing tribometry tests in the presence of atomic (from dissociated molecular) hydrogen leads to lower friction and wear by replenishing the surfaces with atomic H [1.51].

However, introducing other gaseous species (namely water and molecular oxygen) into the environment can have a strong effect on the tribological performance [1.52-54]. Both of these species interact with the surface and negatively impact the friction performance. For DLC, this effect can be understood as a fractional coverage process, whereby the surface has some coverage of species that provide low friction, and the remaining coverage causes high friction [1.55, 56]. Each sliding pass over an area has the potential to remove some fraction of either type of species, after which there will be passivation by the high friction species. The friction coefficient is then governed by the

relative fractions of low and high friction species. In this way, the system can be seen to be dependent on load (how many species are removed per pass), sliding velocity (time between passes during which passivating species can bond to the surface), and partial pressure of ambient species (impingement rate onto the surface). These films will also have low friction in inert environments when run against other counterfaces (*e.g.*, steel). However, the initial friction will be high as wear of the DLC film occurs. This is followed by a transfer of the DLC material from the substrate to the counterface until a transfer film has built up. In this case, it is a process by which the interface effectively becomes self-mated again, resulting in good tribological behavior [1.57-59].

Overall, DLC and a-C:H films have many advantages. They are very smooth as-grown and can be grown thin and conformal to substrates. With the correct growth parameters, these films have very low as-grown stress. Because they are grown with an implantation process, often with a bonding layer, they can be applied to a range of substrate materials. They perform extremely well in vacuum or inert environments and have been shown to have one of the lowest friction coefficients (as low as 0.003) and wear rates ($3x10^{-10}$ $mm^3N^{-1}m^{-1}$) of any material pair [1.60, 61].

	a-C:H soft	a-C:H hard	ta-C:H	ta-C	Diamond
Hardness (GPa)	<10	10-20	50	80	100

Table 1.1: Comparison of hardnesses for hydrogenated and non-hydrogenated carbon materials.

The drawbacks of DLC films are found in their mechanical properties and ambient environment sensitivity. Because of the large fraction of hydrogen and sp^2-

hybridized carbon, DLC films have a lower hardness than H-free carbon films (Table 1.1). Since they are softer, they are more susceptible to abrasive forms of wear. This is especially true when run in environments known to cause higher levels of wear. Non-ideal environments include those containing oxygen, water vapor, or other reactive, non-hydrogen species. Studies have shown (Fig. 1.4) that exposure to water and oxygen poisons the film surface, increasing friction and wear [1.62]. This increased activity makes interfacial bonding stronger and increased friction and wear are seen. There is also an issue with the film properties being sensitive to the specific growth parameters. Changing how the carbon ions are generated, changing their kinetic energies, biasing the sample, and changing the substrate temperature, will affect the film composition. Altering the composition changes the mechanical and tribological properties. Care must be taken to optimize and then maintain constant growth parameters so that the films are consistent. However, when growing these films it is nearly impossible to change one property independently of all others. For instance, if one film is grown with 35 at.% hydrogen and has a certain sp^2/sp^3 carbon bonding ratio, it is not easy to grow another film with 45 at.% hydrogen and maintain the same sp^2/sp^3 ratio. All of these properties depend on one another, which makes growing a specific type of film very difficult.

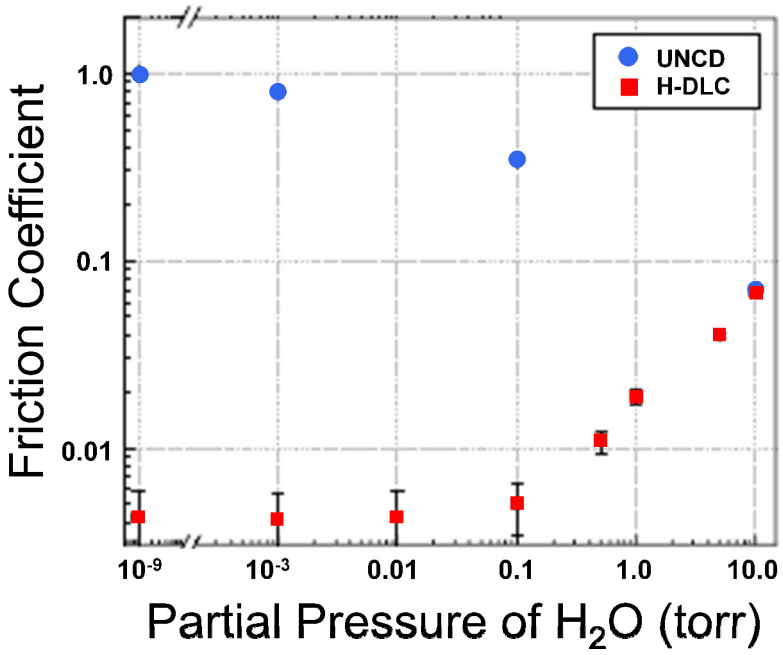

Fig. 1.4: Plot showing friction coefficient dependence on partial pressure of water for UNCD and H-DLC [1.63].

1.3.3 Amorphous Carbons and Polycrystalline Diamond

a-C and ta-C are closely related to DLC films with the difference being the lack of a significant fraction of hydrogen. Unlike DLC, however, these films perform best in environments that contain water vapor (including humidified ambient environments) or molecular hydrogen vapor. They also perform well when fully immersed in water [1.64]. The growth processes can be similar to that discussed above for DLC films, except that little hydrogen (at most a few at.%) is incorporated into the materials. The typical methods for growing ta-C are either with a pulsed laser deposition (PLD) technique or cathodic arc. For PLD, a highly pure graphite target is ablated with an excimer laser. The evaporated species from the target forms a plume that falls on the substrate for

deposition. These films are extremely smooth as-grown, with 0.1 nm r.m.s. roughness [1.65].

As their name suggests, a-C and ta-C are amorphous materials with only short range bonding order. a-C films have a significant (> 30%) fraction of sp^2-bonded carbon, while ta-C (which has 'tetrahedral' in its name to distinguish it from a-C) has 75-90% sp^3-bonded carbon [1.66-68]. Due to its high fraction of sp^2-bonded carbon, a-C, like DLC and a-C:H, has a lower hardness and Young's modulus. Because of the high fraction of sp^3-bonded carbon, ta-C has a modulus that has been measured as high as 759 GPa [1.69]. One disadvantage of the high sp^3 bonding fraction of ta-C is the high compressive stress that exists in the as-grown films (~2-8 GPa). This stress adversely affects applications that require free-standing microstructures since the coated portions will deform to accommodate the stress. However, this stress can be relieved by a post-growth annealing of the film. Annealing can either be accomplished in a vacuum furnace or with a pulsed laser technique. After annealing, the stress in the film is nearly zero [1.70, 71].

The first polycrystalline films developed were micro- and nanocrystalline diamond (MCD and NCD, respectively). Both are grown by chemical vapor deposition. These films are comprised of phase-pure (consisting of ordered, crystalline bonding) diamond grains that can range from several micrometers down to tens of nanometers in size (Fig. 1.5). These grains are connected by grain boundaries that are comprised of both sp^2- and sp^3-bonded carbon, and possibly H. A larger grain size equates to a higher sp^3 fraction for the film, since all of the sp^2-bonded carbon for these films resides in the grain boundaries (the exception being any reconstructed carbon bonds on the free surface of the

film and non-diamond carbon bonding at the interface between the film and the substrate). As the grain size decreases, the relative volume fraction between grains and boundaries decreases, thus increasing the sp^2 fraction of the film. The growth pattern of these films tends to be columnar (Fig. 1.6), with the grains coarsening considerably as the film thickness increases. This means that thicker films are inherently rougher. Like a-C and ta-C, MCD and NCD have the best tribological performance in ambient or humidified environments. During stress and wear, the same bond breaking process occurs and dangling carbon bonds are formed. Bonds that are not passivated will interact strongly with a counterface. Additionally, since these films are much rougher, there is a noticeable period of run-in when fresh surfaces interact [1.72]. During this period, the highest asperities come into mechanical contact and are broken off or smoothed. However, if the films are sufficiently rough, they never run in and are extremely abrasive.

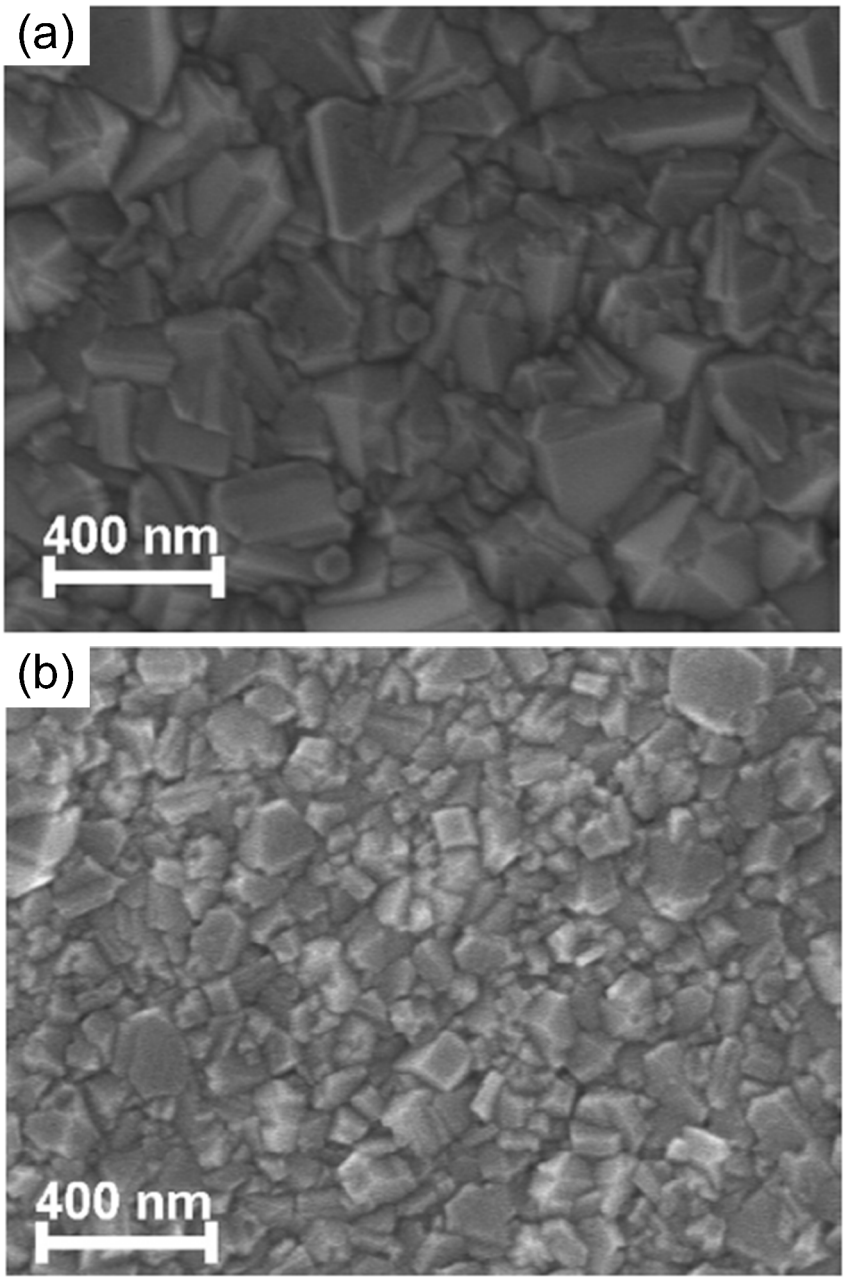

Fig. 1.5: SEM images of NCD for (a) ~600 nm thick coating, and (b) ~200 nm thick coating [1.73].

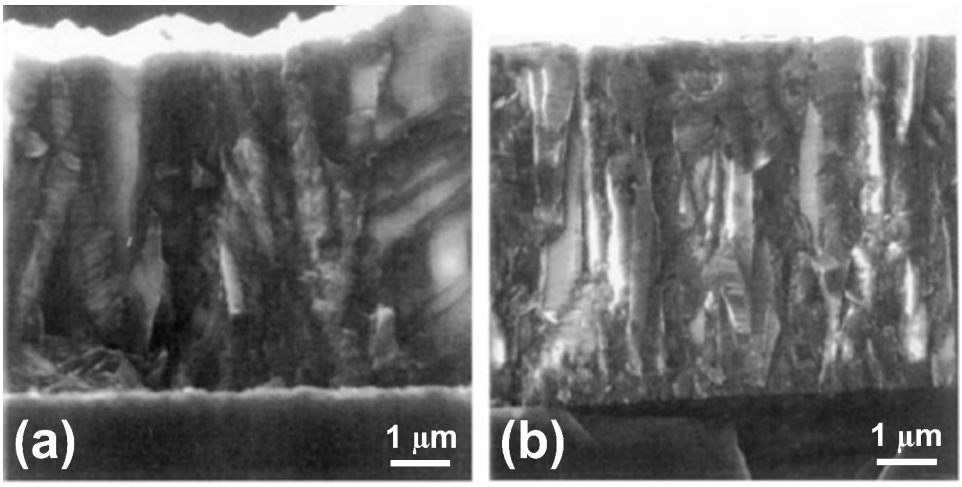

Fig. 1.6: Cross-section SEM [1.74] of two NCD films showing columnar structure grown with (a) 1% CH_4, 2% Ar, and 97% H_2, and (a) 1% CH_4, 80% Ar, and 19% H_2

UNCD is grown by either microwave plasma or hot filament CVD (MPCVD or HFCVD respectively). A methane source gas dissociates and forms reactive carbon species. The film grows as these carbon species arrange themselves on the surface in a diamond-like configuration, with the hydrogen in the environment stripping away non-diamond species. The main difference between the growth of MCD/NCD and of UNCD is the renucleation rate of the diamond grains. MCD and NCD have less hydrogen available near the surface during growth, which means the hydrocarbon species that adsorb have more time to rearrange into a continuous diamond grain before renucleation occurs. Due to the higher amount of atomic hydrogen presence during UNCD growth, there is a much higher rate of hydrogen abstraction (interaction of atomic hydrogen that removes a terminal hydrogen from the diamond surface), and adsorbed carbon species are more likely to become a defect site for the renucleation of a new grain [1.75]. The current state-of-the-art for UNCD growth yields a typical as-grown surface roughness of ~5 nm

r.m.s. over a 1 x 1 μm^2 area, characteristic 2-5 nm grains (Fig. 1.7), and exhibits 95-98% sp^3 bonding [1.76]. Unlike MCD and NCD, which are rougher due to both grain size and grain coarsening with film thickness, UNCD retains its small grain size and low roughness independent of film thickness. These films can also be doped (boron for MCD, NCD, and UNCD, and nitrogen for UNCD) to increase their conductivity.

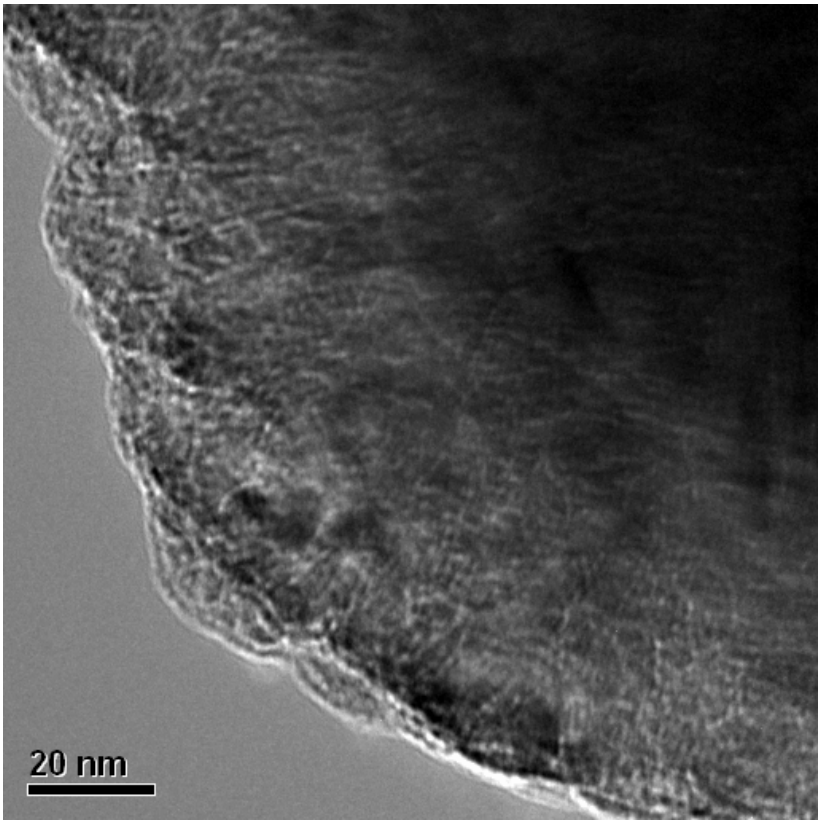

Fig. 1.7: Transmission electron microscope image of UNCD-coated atomic force microscope probe showing small (~3-5 nm) grain size, courtesy of Tevis Jacobs.

Historically, there have been two main hypotheses to explain the wear behavior of H-free materials. The remarkably low friction and wear of diamond, particularly in humid environments, is postulated to be due to either: 1) rehybridiziation [1.77-79] or 2) passivation [1.80, 81] of dangling bonds formed during sliding. Firstly, rehybridization to

ordered sp^2 bonding is plausible because graphite is the thermodynamically stable form of carbon at room temperature and ambient pressure, and is lubricious due to its layered structure. Rehybridization may also involve the formation of lubricious amorphous sp^2-containing carbon [1.82]. The significant energy barrier that must be overcome in order to convert diamond to graphite or amorphous carbon (~1.0 eV/atom) [1.83] may be lowered by shear, frictional heating, or the introduction of oxygen and water vapor. Secondly, passivation has been proposed by others [1.84-86] because friction and wear for diamond are lower in environments containing H_2 or H_2O than they are in a vacuum. Desorption, induced either mechanically or thermally, creates dangling carbon bonds that increase friction and wear due to interfacial bonding [1.87]. A sufficient supply of passivating species overcomes this by preemptively terminating the dangling bonds. In ambient environments containing water and other molecules, as bonds are broken they can be passivated by the dissociative adsorption of hydrogen, oxygen, and water molecules. The C-H and C-O bonded surfaces then have reduced interfacial interactions, resulting in lower friction and thus wear. For water, we have shown that this concentration can be as little as 1.0% relative humidity (RH) [1.88]. Previous work has shown that it is energetically favorable for these species to dissociate (water into H- and OH- groups, hydrogen into two H-) and bond to an unterminated diamond surface [1.89, 90]. However, no previous studies presented spectroscopic evidence to clearly validate either hypothesis. As well, no previous studies have fully explored the range of conditions for which the low friction and wear behavior can be maintained, nor explained the underlying mechanisms that determine the limits to this behavior.

This main purpose of this thesis is to investigate the environmental dependence of two hydrogen-free, hard carbon thin films: UNCD and ta-C. The specific focus will be on the tribological behavior in dry and humid environments, with the key question being what role water plays as a potential lubricant. Since friction and wear are dependent on bond breaking and formation, the effects of contact pressure are also studied. A formalized approach is developed that methodically examines: 1) tribological performance in a controlled environment with calibrated tribometers, 2) topographic characterization with optical interferometry to measure wear, and 3) chemical characterization including spatially resolved x-ray absorption techniques. Conclusions are drawn from the data as to specific wear and lubrication mechanisms for these materials and comparisons to previous experiments and to relevant simulations and theory are discussed.

Chapter 2 puts forth a detailed description of the various sample preparation techniques, the experimental equipment and settings, and specific analysis methods. A set of experiments for ta-C and UNCD that varies both contact pressure and RH is described in Chapter 3. Chapter 4 covers a peculiar phenomenon seen for UNCD whereby decreasing the RH during sliding below a certain threshold causes friction to increase by 1-2 orders of magnitude. Increasing the RH again over the threshold (with some hysteresis) recovers the system to low friction. The origins of this dramatic and newly observed behavior are also discussed. Chapter 5 describes a newly-built instrument at the National Synchrotron Light Source that was used to examine both counterfaces of a UNCD self-mated contact after tribological testing. Finally, the conclusions that connect

all of these results are examined in Chapter 6, and these conclusions are related to the larger scope of carbon film tribology. The Appendix lists publications by the author as well as analysis code written to support this work.

1.4 Chapter 1 References

[1.1] H. P. Jost, Tribology and Lubrication Technology **62**, 24 (2006).
[1.2] D. Dowson, *History of tribology* (Longman, London; New York, 1979).
[1.3] B. Bhushan, (ASME, New York, NY, USA, 1998), pp. 265.
[1.4] H. P. Jost, Tribology and Lubrication Technology **62**, 24 (2006).
[1.5] P. Daic, F. Franek, E. Assenova, and M. Radovanovic, Industrial Lubrication and Tribology **55**, 287 (2003).
[1.6] B. Bhushan, *Fundamentals of tribology and bridging the gap between the macro- and micro/nanoscales* (Kluwer Academic Publishers, Dordrecht; Boston, 2001).
[1.7] J. E. Field, *The Properties of diamond* (Academic Press, London; New York, 1979).
[1.8] V. G. Vins, and E. V. Pestryakov, Diamond and Related Materials **15**, 569 (2006).
[1.9] W. Jin-Hui, A. Raczynski, J. Zaremba, S. Zielinska-Kaniasty, M. Artoni, and G. C. La Rocca, Journal of Modern Optics **56**, 768 (2009).
[1.10] R. F. Davis, *Diamond films and coatings : development, properties, and applications* (Noyes Pub., Park Ridge, N.J., 1993).
[1.11] R. M. Denning, American Mineralogist **38**, 108 (1953).
[1.12] M. Seal, Philosophical Magazine A (Physics of Condensed Matter, Defects and Mechanical Properties) **43**, 587 (1981).
[1.13] F. P. Bowden, C. A. Brookes, and A. E. Hanwell, Nature **203**, 27 (1964).
[1.14] F. P. Bowden, and J. E. Young, Proceedings of the Royal Society of London, Series A (Mathematical and Physical Sciences) **208**, 444 (1951).
[1.15] F. P. Bowden, and A. E. Hanwell, Nature **201**, 1279 (1964).
[1.16] T. A. Friedmann, J. P. Sullivan, J. A. Knapp, D. R. Tallant, D. M. Follstaedt, D. L. Medlin, and P. B. Mirkarimi, Applied Physics Letters **71**, 3820 (1997).
[1.17] J. Robertson, Materials Science and Engineering: R: Reports **37** (2002).
[1.18] S. Cho, I. Chasiotis, T. A. Friedmann, and J. P. Sullivan, Journal of Micromechanics and Microengineering **15**, 728 (2005).
[1.19] A. V. Sumant, D. S. Grierson, J. E. Gerbi, J. Birrell, U. D. Lanke, O. Auciello, J. A. Carlisle, and R. W. Carpick, Advanced Materials **17**, 1039 (2005).
[1.20] O. Auciello *et al.*, IEEE Microwave Magazine **8**, 61 (2007).
[1.21] A. V. Sumant, A. R. Krauss, D. M. Gruen, O. Auciello, A. Erdemir, M. Williams, A. F. Artiles, and W. Adams, Tribology Transactions **48**, 24 (2005).
[1.22] A. V. Sumant, A. R. Krauss, D. M. Gruen, O. Auciello, A. Erdemir, M. Williams, A. F. Artiles, and W. Adams, Tribology Transactions **48**, 24 (2005).
[1.23] D. S. Grierson *et al.*, Journal of Vacuum Science and Technology B: Microelectronics and Nanometer Structures **25**, 1700 (2007).
[1.24] A. R. Konicek, D. S. Grierson, P. U. P. A. Gilbert, W. G. Sawyer, A. V. Sumant, and R. W. Carpick, Physical Review Letters **100**, 235502 (2008).
[1.25] C. Matta, M. I. De Barros Bouchet, T. Le-Mogne, B. Vachet, J. M. Martin, and T. Sagawa, Lubrication Science **20**, 137 (2008).

[1.26] C. Matta, O. L. Eryilmaz, M. I. De Barros Bouchet, A. Erdemir, J. M. Martin, and K. Nakayama, Journal of Physics D: Applied Physics **42** (2009).
[1.27] B. T. Kelly, *Physics of graphite* (Applied Science, London; Englewood, N.J., 1981).
[1.28] L. Changgu, W. Xiaoding, J. W. Kysar, and J. Hone, Science **321**, 385 (2008).
[1.29] J. Robertson, Materials Science and Engineering: R: Reports **37** (2002).
[1.30] J. A. Heimberg, K. J. Wahl, I. L. Singer, and A. Erdemir, Applied Physics Letters **78**, 2449 (2001).
[1.31] A. Erdemir, and C. Donnet, Journal of Physics D (Applied Physics) **39**, 311 (2006).
[1.32] A. Erdemir, O. L. Eryilmaz, I. B. Nilufer, and G. R. Fenske, Surface & Coatings Technology **133-134**, 448 (2000).
[1.33] J. Andersson, R. A. Erck, and A. Erdemir, Surface & Coatings Technology **163-164**, 535 (2003).
[1.34] A. V. Sumant, A. R. Krauss, D. M. Gruen, O. Auciello, A. Erdemir, M. Williams, A. F. Artiles, and W. Adams, Tribology Transactions **48**, 24 (2005).
[1.35] R. R. Chromik, A. L. Winfrey, J. Luning, R. J. Nemanich, and K. J. Wahl, Wear **265**, 477 (2008).
[1.36] A. R. Konicek, D. S. Grierson, P. U. P. A. Gilbert, W. G. Sawyer, A. V. Sumant, and R. W. Carpick, Physical Review Letters **100**, 235502 (2008).
[1.37] M. A. Hamilton, A. R. Konicek, D. S. Grierson, A. V. Sumant, O. Auciello, W. G. Sawyer, and R. W. Carpick, (ASME, Miami, FL, United states, 2009), pp. 9.
[1.38] J. Robertson, Materials Science and Engineering: R: Reports **37** (2002).
[1.39] S. Aisenberg, and R. Chabot, Journal of Vacuum Science and Technology **8**, 112 (1971).
[1.40] J. Robertson, Materials Science and Engineering: R: Reports **37** (2002).
[1.41] J. Robertson, Materials Science and Engineering: R: Reports **37** (2002).
[1.42] J. Robertson, Materials Science and Engineering: R: Reports **37** (2002).
[1.43] J. W. Zou, K. Reichelt, K. Schmidt, and B. Dischler, Journal of Applied Physics **65**, 3914 (1989).
[1.44] C. Wild, and P. Koidl, Applied Physics Letters **51**, 1506 (1987).
[1.45] S. S. Camargo, Jr., A. L. Baia Neto, R. A. Santos, F. L. Freire, Jr., R. Carius, and F. Finger, Diamond and Related Materials **7**, 1155 (1998).
[1.46] C. Donnet, J. Fontaine, F. Lefebvre, A. Grill, V. Patel, and C. Jahnes, Journal of Applied Physics **85**, 3264 (1999).
[1.47] A. Erdemir, and C. Donnet, Journal of Physics D (Applied Physics) **39**, 311 (2006).
[1.48] A. Erdemir, and C. Donnet, Journal of Physics D (Applied Physics) **39**, 311 (2006).
[1.49] O. L. Eryilmaz, and A. Erdemir, Surface & Coatings Technology **203**, 750 (2008).
[1.50] O. L. Eryilmaz, and A. Erdemir, Surface & Coatings Technology **203**, 750 (2008).
[1.51] F. Gao, A. Erdemir, and W. T. Tysoe, Tribology Letters **20**, 221 (2005).

[1.52] J. Andersson, R. A. Erck, and A. Erdemir, Surface & Coatings Technology **163-164**, 535 (2003).
[1.53] H. I. Kim, J. R. Lince, O. L. Eryilmaz, and A. Erdemir, Tribology Letters **21**, 53 (2006).
[1.54] O. L. Eryilmaz, and A. Erdemir, Wear **265**, 244 (2008).
[1.55] P. L. Dickrell, W. G. Sawyer, and A. Erdemir, Journal of Tribology **126**, 615 (2004).
[1.56] P. L. Dickrell, W. G. Sawyer, J. A. Heimberg, I. L. Singer, K. J. Wahl, and A. Erdemir, Transactions of the ASME. Journal of Tribology **127**, 82 (2005).
[1.57] K. Holmberg, J. Koskinen, H. Ronkainen, J. Vihersalo, J. P. Hirvonen, and J. Likonen, Diamond Films and Technology **4**, 113 (1994).
[1.58] A. Erdemir, F. A. Nichols, X. Z. Pan, R. Wei, and P. Wilbur, Diamond and Related Materials **3**, 119 (1994).
[1.59] K. Jia, Y. Q. Li, T. E. Fischer, and B. Gallois, Journal of Materials Research **10**, 1403 (1995).
[1.60] A. Erdemir, O. L. Eryilmaz, I. B. Nilufer, and G. R. Fenske, Surface & Coatings Technology **133-134**, 448 (2000).
[1.61] A. Erdemir, O. L. Eryilma, and G. Fenske, (AIP for American Vacuum Soc, Seattle, WA, USA, 2000), pp. 1987.
[1.62] H. I. Kim, J. R. Lince, O. L. Eryilmaz, and A. Erdemir, Tribology Letters **21**, 53 (2006).
[1.63] H. I. Kim, J. R. Lince, O. L. Eryilmaz, and A. Erdemir, Tribology Letters **21**, 53 (2006).
[1.64] S. E. Grillo, and J. E. Field, European Physical Journal B **13**, 405 (2000).
[1.65] Y. Lifshitz, G. D. Lempert, and E. Grossman, Physical Review Letters **72**, 2753 (1994).
[1.66] T. A. Friedmann, J. P. Sullivan, J. A. Knapp, D. R. Tallant, D. M. Follstaedt, D. L. Medlin, and P. B. Mirkarimi, Applied Physics Letters **71**, 3820 (1997).
[1.67] S. Cho, I. Chasiotis, T. A. Friedmann, and J. P. Sullivan, Journal of Micromechanics and Microengineering **15**, 728 (2005).
[1.68] C. Matta, M. I. De Barros Bouchet, T. Le-Mogne, B. Vachet, J. M. Martin, and T. Sagawa, Lubrication Science **20**, 137 (2008).
[1.69] S. Cho, I. Chasiotis, T. A. Friedmann, and J. P. Sullivan, Journal of Micromechanics and Microengineering **15**, 728 (2005).
[1.70] T. A. Friedmann, J. P. Sullivan, J. A. Knapp, D. R. Tallant, D. M. Follstaedt, D. L. Medlin, and P. B. Mirkarimi, Applied Physics Letters **71**, 3820 (1997).
[1.71] T. M. Alam, T. A. Friedmann, P. A. Schultz, and D. Sebastiani, Physical Review B (Condensed Matter and Materials Physics) **67**, 245309 (2003).
[1.72] I. P. Hayward, I. L. Singer, and L. E. Seitzman, Wear **157**, 215 (1992).
[1.73] C. D. Torres, P. J. Heaney, A. V. Sumant, M. A. Hamilton, R. W. Carpick, and F. E. Pfefferkorn, International Journal of Machine Tools and Manufacture **49**, 599 (2009).
[1.74] D. M. Gruen, Annual Review of Materials Science **29**, 211 (1999).
[1.75] P. W. May, J. N. Harvey, J. A. Smith, and Y. A. Mankelevich, Journal of Applied Physics **99** (2006).

[1.76] A. V. Sumant, O. Auciello, H. C. Yuan, Z. Ma, R. W. Carpick, and D. C. Mancini, (SPIE - The International Society for Optical Engineering, USA, 2009), p. 731817 (7 pp.).
[1.77] M. N. Gardos, and B. L. Soriano, Journal of Materials Research **5**, 2599 (1990).
[1.78] A. Erdemir, G. R. Fenske, A. R. Krauss, D. M. Gruen, T. McCauley, and R. T. Csencsits, (Elsevier, Switzerland, 1999), pp. 565.
[1.79] S. E. Grillo, and J. E. Field, Journal of Physics D (Applied Physics) **33**, 595 (2000).
[1.80] M. N. Gardos, and S. A. Gabelich, Tribology Letters **6**, 103 (1999).
[1.81] H. I. Kim, J. R. Lince, O. L. Eryilmaz, and A. Erdemir, Tribology Letters **21**, 53 (2006).
[1.82] A. Erdemir, O. L. Eryilma, and G. Fenske, (AIP for American Vacuum Soc, Seattle, WA, USA, 2000), pp. 1987.
[1.83] L. Sun, Q. Wu, Y. Zhang, and W. Wang, Journal of Materials Research **14**, 631 (1999).
[1.84] M. N. Gardos, and S. A. Gabelich, Tribology Letters **6**, 103 (1999).
[1.85] H. I. Kim, J. R. Lince, O. L. Eryilmaz, and A. Erdemir, Tribology Letters **21**, 53 (2006).
[1.86] M. N. Gardos, Tribology Letters **2**, 173 (1996).
[1.87] G. T. Gao, P. T. Mikulski, G. M. Chateauneuf, and J. A. Harrison, Journal of Physical Chemistry B **107**, 11082 (2003).
[1.88] A. R. Konicek, D. S. Grierson, P. U. P. A. Gilbert, W. G. Sawyer, A. V. Sumant, and R. W. Carpick, Physical Review Letters **100**, 235502 (2008).
[1.89] Y. Qi, E. Konca, and A. T. Alpas, Surface Science **600**, 2955 (2006).
[1.90] O. Manelli, S. Corni, and M. C. Righi, The Journal of Physical Chemistry C (2010).

2. Experimental Methods

2.1 Film Growth

This thesis focuses on two ultra-hard, nearly hydrogen-free (H-free) carbon films, tetrahedral amorphous carbon (ta-C) and ultrananocrystalline diamond (UNCD). These are two of the smoothest carbon films of their respective types. ta-C is characterized by extremely low roughness, and UNCD is the smoothest (independent of total thickness) as-grown polycrystalline diamond film yet developed. Since they both are predominantly comprised of sp^3-bonded carbon, they have higher moduli and hardnesses [2.1-3] than DLC or a-C films, and, for some UNCD films, the values approach that for single crystal diamond [2.4].

All studies conducted herein investigate self-mated interfaces. This means both counterfaces are coated with the same material (in most cases at the same time in the particular deposition system). Typically, Si flats (1x1 cm^2) and Si_3N_4 spheres (Cerbec, 3 mm diameter, high polish grade) are simultaneously coated with either ta-C or UNCD. Si3N4 spheres are used since they are relatively inexpensive and easily attainable. They are also polished to a ~4 nm r.m.s. roughness during the manufacturing process. To create a reference mark for subsequent processes such as film growth, the spheres are polished using a polishing wheel with 180 grit SiC paper to produce a small flat spot. The spheres are adhered to a metal stub using a meltable epoxy and then pressed against the polishing wheel and worn until a flat portion ~1.5 mm across is discernible by the naked eye. During subsequent growth, this flat portion is placed away from the growth source. For

tribometry the flat portion is mounted on a flexure (described below), away from the contact. Since the coating is thin and often indistinguishable from the sphere, this polishing step removes the uncertainty of knowing which side the coating is on for tribometer experiments. After tribometry, the wear scar will be nearly opposite the polished flat, providing a reproducible spot for mounting the sphere to measure topography or chemistry.

The ta-C films are deposited at Sandia National Laboratory using pulsed laser deposition [2.5, 6]. Typically, ta-C has an as-grown surface roughness of ~1 nm root-mean-squared (r.m.s.) roughness (measured over a 1x1 μm^2 area [2.7]) and can be as low as 0.1 nm or as high as 30 nm. The film is comprised of an amorphous network of carbon that is 80% sp^3-bonded (characterized by nuclear magnetic resonance spectroscopy), with the remaining 20% being sp^2-bonded [2.8]. Fig. 2.1 shows a simulated bonding structure of ta-C made up of 64 total atoms, using Car-Parrinello first principles molecular dynamics. In this simulation, 42 sp^3-bonded carbon atoms form groups of three or four atoms in rings, and the 22 sp^2-bonded carbon atoms cluster into extended networks [2.9].

Growth is carried out at room temperature using a KrF excimer laser (248 nm). A pure graphite target is rotated and ablated as the carbon source. Carbon ions with energies centered at 100 eV are deposited onto the surface. Deposition is typically carried out at room temperature, though varying the substrate temperature can change the properties of the film, such as conductivity [2.10]. As-grown ta-C films have a relatively high amount of residual compressive stress (typically 8 GPa for the growth conditions used here), so a post-growth, rapid thermal annealing treatment at 600 °C for 5 minutes is applied to all

ta-C films in order to relieve the stress [2.11]. This annealing process causes a restructuring of the film that relieves stress by reordering the bonds without significantly changing the bonding hybridization [2.12]. This step is especially important for fabricating devices out of ta-C. If annealing is not performed, patterned structures that are released after growth will deform due to the residual stresses and stress gradients, which can render a device useless. Additionally, for the case where the ta-C film is used as a tribological coating, film failure by delamination is more likely to occur when the film contains a high amount of stress [2.6].

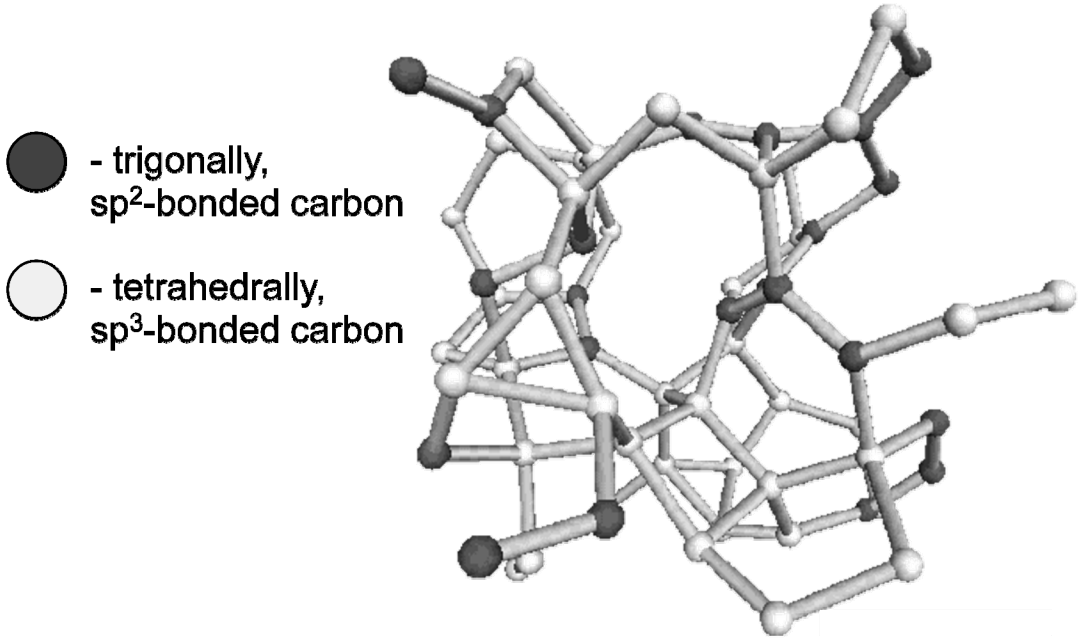

Fig. 2.1: Representative section of a ta-C network comprised of 64 atoms. Dark spheres are trigonally (3-fold) coordinated and light spheres are tetrahedrally (4-fold) coordinated [2.13]

UNCD is deposited at Argonne National Laboratory using a 2.45 GHz microwave plasma chemical vapor deposition technique, in a commercial IPLAS (Innovative Plasma

Systems GmbH, Troisdorf, Germany) system [2.14]. The current state-of-the-art for UNCD growth yields a film with 2-5 nm diamond grains and grain boundaries less than 1 nm wide. UNCD has 95-98% sp^3 bonding, with the remaining fraction of sp^2-bonded carbon in the grain boundaries and on the surface [2.15]. Typical as-grown surface roughness is ~5 nm r.m.s. over a 1x1 μm^2 area.

Substrates are ultrasonically pretreated with nanodiamond suspension in dimethyl sulfoxide (minimum grain size ~4 nm diameter; ITC, Inc., Raleigh, NC) [2.15]. Gas flow rates during growth are 49.2/0.8 using an argon/methane (Ar/CH_4) gas chemistry. The chamber pressure is 140 mbar and the substrate temperature is set to 780 °C. Film growth occurs using the diamond-seeded surface as a nucleation layer. The plasma dissociates the methane and produces atomic hydrogen as well as energetic carbon species (primarily C_1). The carbon species bond to the surface in a diamond-like fashion, growing phase pure diamond grains separated by grain boundaries that are a fraction of a nm thick (Fig. 2.2) [2.16]. Hydrogen abstraction plays in an important role during this process by preferentially attacking sp^2-bonded carbon atoms and removing them from the surface, as well as aiding the addition of C_1 species to the growing film. High renucleation rates (a function of the growth temperature and available hydrogen) are the key to keeping the grain size low, as well as the grain boundary width small, for these films. Unlike nanocrystalline diamond (NCD) films, which suffer from grain coarsening as a function of film thickness (eventually becoming microcrystalline), UNCD grains remain the same size independent of film thickness.

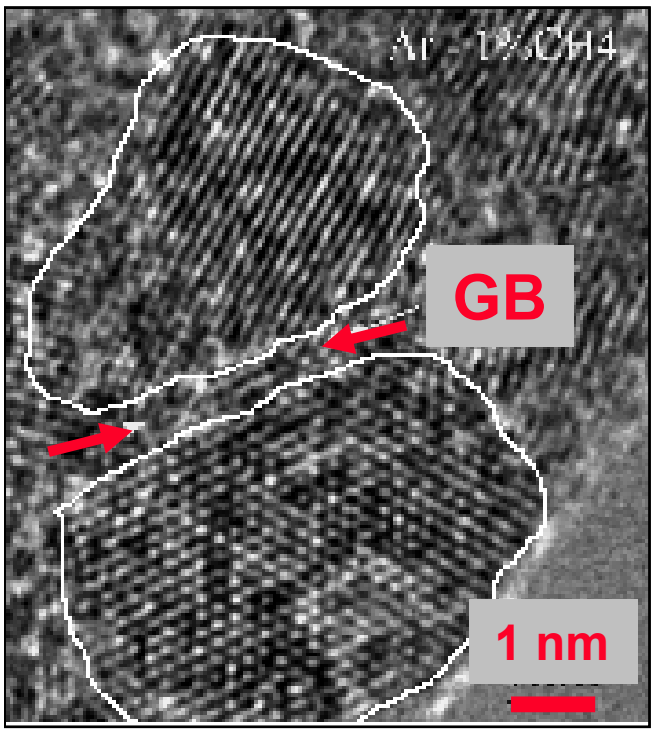

Fig. 2.2: High resolution TEM image showing UNCD grains and grain boundary (GB) [2.17]

2.2 Tribometry

After deposition on the flats and spheres, these films are used for self-mated tribometry tests that were carried out in the lab of Prof. W.G. Sawyer at the University of Florida by other personnel (Prof. W.G. Sawyer, Dr. M.A. Hamilton, Dr. P.L. Dickrell, A.C. Dunn, and J.H. Keith) as well as the author himself. Self-mated interfaces are simpler and better suited for basic studies of tribological behavior, since they avoid the complexities that arise from having to consider additional materials, chemical compositions, and mechanical properties.

Tribometers are devices that allow for the study of friction and wear at the macroscale for a range of material pairings while under controlled conditions. These conditions include load, contact geometry, sliding geometry, temperature (of either the environment or the substrate), and environment (*e.g.*, vacuum, controlled partial pressure of gas). Typically, a spherical pin is brought into contact with a flat substrate under a fixed load. The substrate and pin can be made of or coated by the same material (meaning the interface is 'self-mated') or they can be different materials. After contact is established, the substrate and pin are then put into relative motion. This motion can be either linear or circular (pin-on-disk). The resulting worn region on the substrate will henceforth be referred to as a wear track. This is distinguished from the worn region on the sphere, which will be referred to as a wear scar. Linear motion can be either unidirectional or reciprocating. With unidirectional sliding, the pin makes one linear sliding pass, is brought out of contact at the end of the wear track, and then is brought back into contact where the sliding pass first began. With reciprocating motion, the pin never leaves contact with the substrate, and a full sliding cycle involves two back-and-forth passes in opposite directions along the same track. Circular or pin-on-disk motion involves the substrate rotating at a constant specified angular velocity such that the pin will prescribe a circular wear track on the substrate about the center axis of rotation.

There are several benefits to pin-on-disk experiments. One is that the sliding speed is constant along every point of the track. In contrast, during linear sliding there must necessarily be acceleration and deceleration periods at the beginning and ending of the track. The sliding velocity during linear sliding is determined by the maximum

velocity that is reached and maintained through the middle portion of the track. The other benefit of pin-on-disk motion is a fixed exposure time. The exposure time is the amount of time that elapses between the pin contacting the same portion of the track. Since the pin-on-disk configuration has a constant sliding velocity, there is a well-defined, constant exposure time that is equal to the inverse of the rotation frequency. Reciprocation only has one well-defined point of constant exposure time, located at the center of the track. All other points experience staggered times between sliding passes. However, linear wear tracks are easier to create and can be packed on a sample with a much higher density, which makes subsequent topographic and chemical analysis easier. For this reason, all of the tracks discussed in this document are made in a linear fashion.

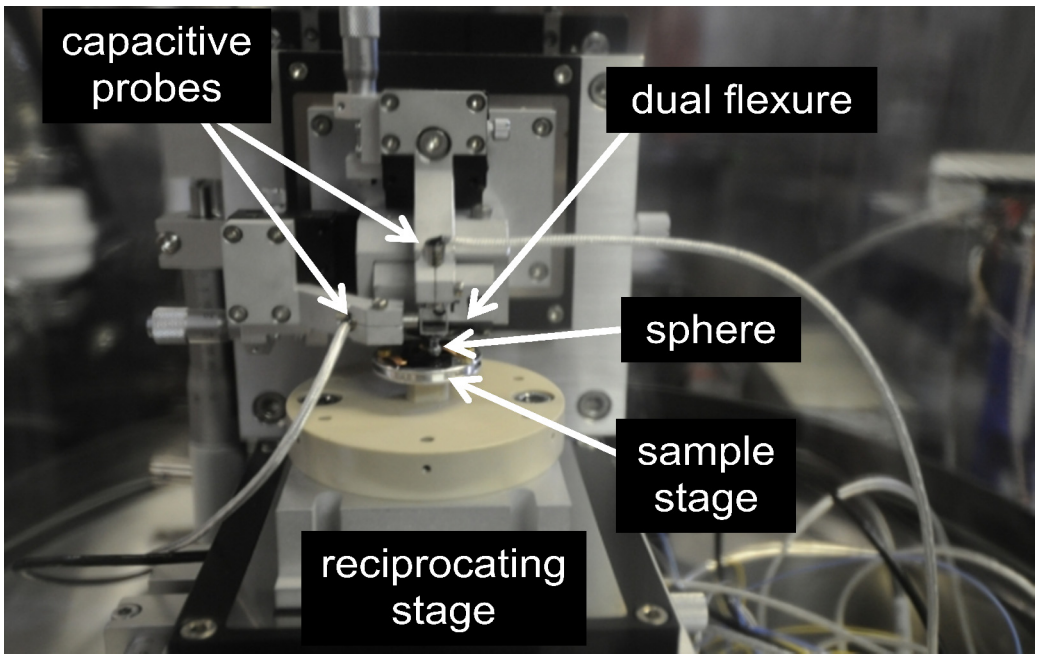

Fig. 2.3: Picture of tribometer setup. This version is using capacitive probes to detect normal and lateral deflections of the dual flexure.

The substrate is placed on an *x*-*y* micrometer stage that is used to position the sample laterally under the pin and set the location for the wear tracks (Fig. 2.3). Using super glue, the pin is affixed to the end of a dual flexure cantilever that can bend both normal and transverse to the surface. Displacement sensors are mounted at the end of the flexure. The original tribometer design involved two mirrors [2.18], one each mounted such that the surface normal of the mirrors was along the normal and lateral bending direction of the flexure, respectively. A schematic of this is shown in Fig. 2.4. Lasers reflect off the mirror surfaces and detect displacements of the flexure both normal and transverse to the substrate. The mirror/laser setup was used to take the data in Chapter 3. The current design utilizes capacitive probes instead of lasers [2.19] (Fig. 2.3), and a metal box is affixed to the end of the flexure instead of mirrors. In this case, the displacement is detected by the change in capacitance as measured between the probe and the side of the metal box. The capacitive setup was used to take the data in Chapter 4 and Chapter 5. A *z*-micrometer is used for coarse positioning of the flexure away and toward the substrate. The flexure deflection normal to the sample surface is calibrated (displacement as a function of force), and this deflection is used to measure the normal load applied to the substrate as the pair is brought into contact. A software-driven stepper motor controls the fine positioning necessary to apply the initial load and also to control the displacement to keep the load at the desired set point during the testing. As the pin slides along the track, the tribometer records, as a function of position, the normal force (measured from the normal deflection of the cantilever) and lateral force (caused by the friction between the pin and substrate, and measured by the lateral deflection of the

cantilever). Dividing this friction force by the normal force yields the friction coefficient as a function of position. Friction coefficient measurements are obtained from data averaged over the middle 90% of the track, where the velocity is nominally constant, ignoring the endpoints of the track where the sample is accelerating or decelerating. The total number of sliding cycles is set in the software by the user, as well as how many data sets of the individual cycles to save. The program records sliding time, cycle number, calculated friction coefficient, lateral force, normal force, wear track position, sliding speed, *z*-stage displacement, and humidity for every point along the wear track (typically ~500 measured points per sliding cycle). Saving all of the data for every sliding cycle quickly fills up hard drive space. To reduce data storage needs, usually only every 20^{th} cycle has the full cycle data saved. The main output file contains just the average quantities for each entire cycle.

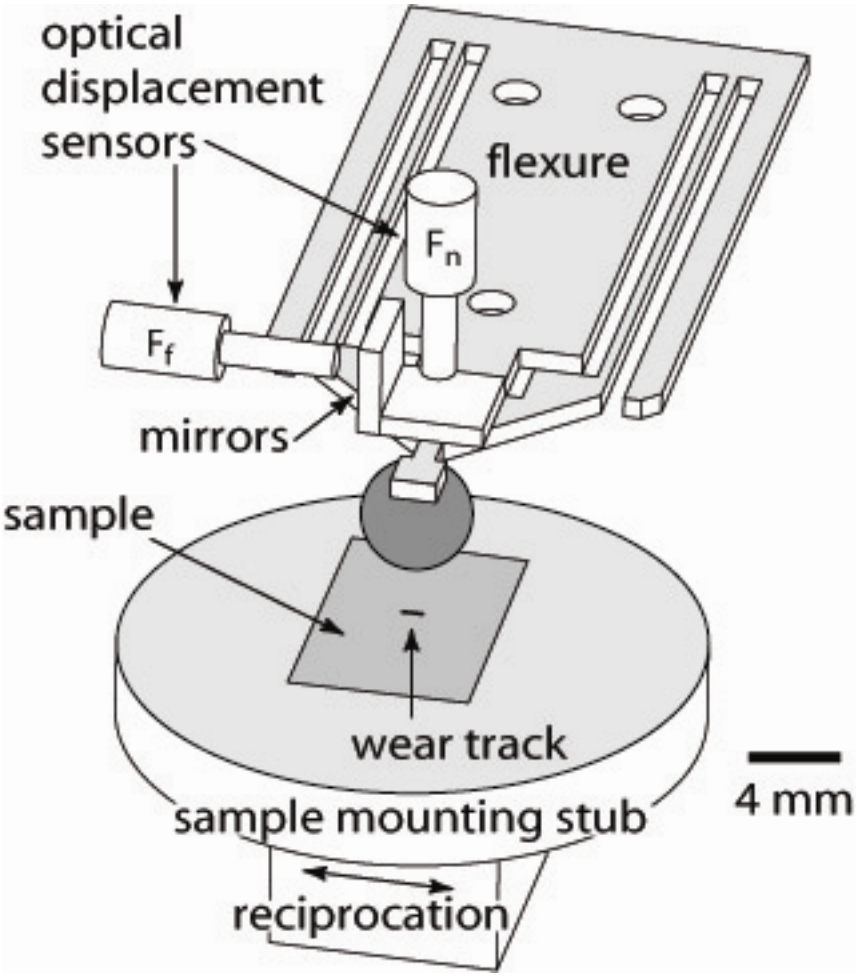

Fig. 2.4: Tribometer schematic showing dual flexure, optical displacement sensors, mirrors, and reciprocating substrate holder.

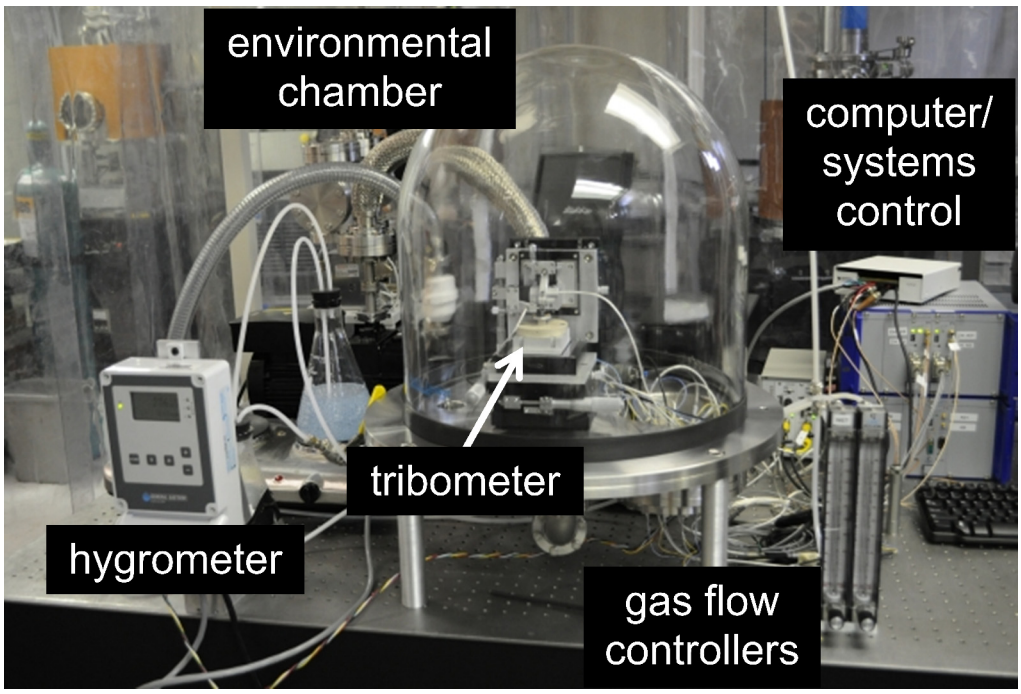

Fig. 2.5: Experimental tribometer setup. Gas flow controllers, one for dry Ar and one for Ar bubbled through de-ionized (DI) water, control relative humidity (measured with a hygrometer) in environmental chamber. Computer controls tribometer and records data.

The reciprocating tribometer (described in more detail here [2.18]) is housed inside an environmentally-controlled chamber (Fig. 2.5). Humidity is introduced by controlling the flow of dry Ar first through a beaker containing DI water, then into an empty beaker (to prevent water droplets from being blown directly near the tribometer), and finally fed into the chamber. This occurs in parallel with a flow of dry Ar alone. The Ar source is blowoff from a dewar that is research-grade quality to ensure the lowest possible levels of contaminants (*e.g.* water). Extremely dry tests (relative humidity (RH) below 1.5%) require a dry Ar source that is absent of any residual water. Even with a research-grade source, it takes several hours of flowing Ar to reduce the RH to these low

levels. RH is measured with a DewPro MMY 2650 hygrometer that is accurate to ±0.1% with a lower detection limit of 0.1%. The user must manually control the RH by adjusting the two sources to the correct levels. The software records the value from the hygrometer while measuring the other parameters.

A close-up of a UNCD sample mounted on the reciprocating stub is shown in Fig. 2.6. As mentioned, the micrometer control of the stage position ensures the location of the tracks can be carefully and precisely placed. This increases the density of tracks on the sample, and makes further measurements easier. This is especially important in photoelectron emission microscopy (discussed in Section 2.5) where the field of view (FOV) is only ~40x80 μm^2. Scanning an 8x8 mm^2 region with this small FOV looking for 40x500 μm^2 tracks is bad enough. If they are randomly placed, it would only be worse.

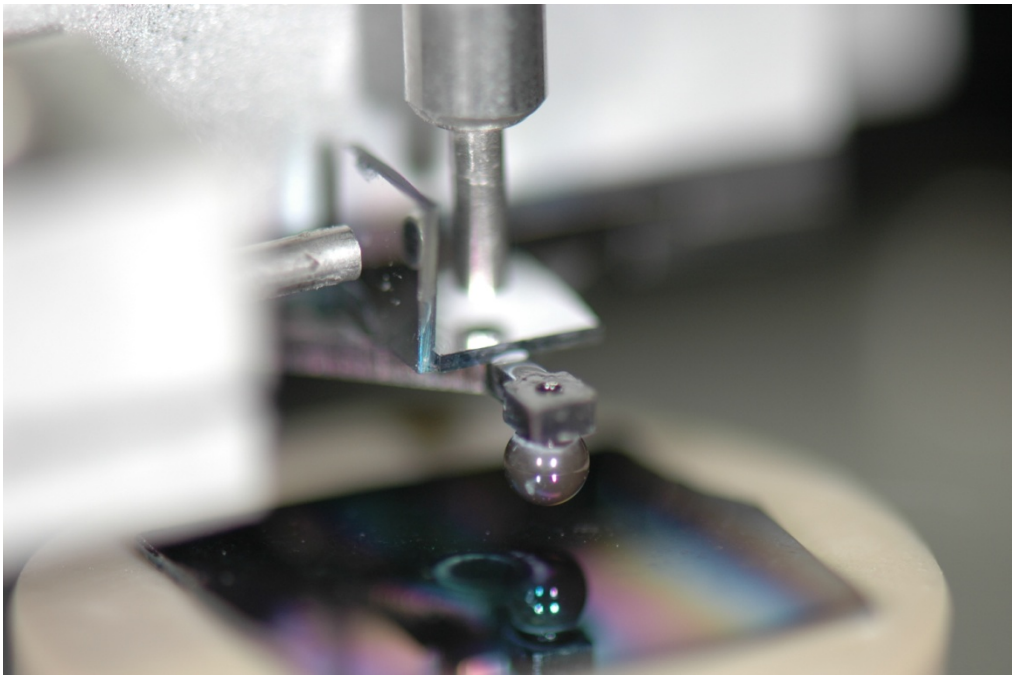

Fig. 2.6: Zoomed image showing UNCD-coated sphere and flat in tribometer.

Fig. 2.7 shows an optical image of an array of tracks made on a UNCD sample. This shows the high areal density of making linear wear tracks. They are spaced 1 mm in both directions to prevent any wear debris from a track affecting other areas of the sample. The debris rarely is more than 100 μm away from a track, except in the case of extreme wear (*e.g.* Fig. 2.7, right column, top and bottom tracks).

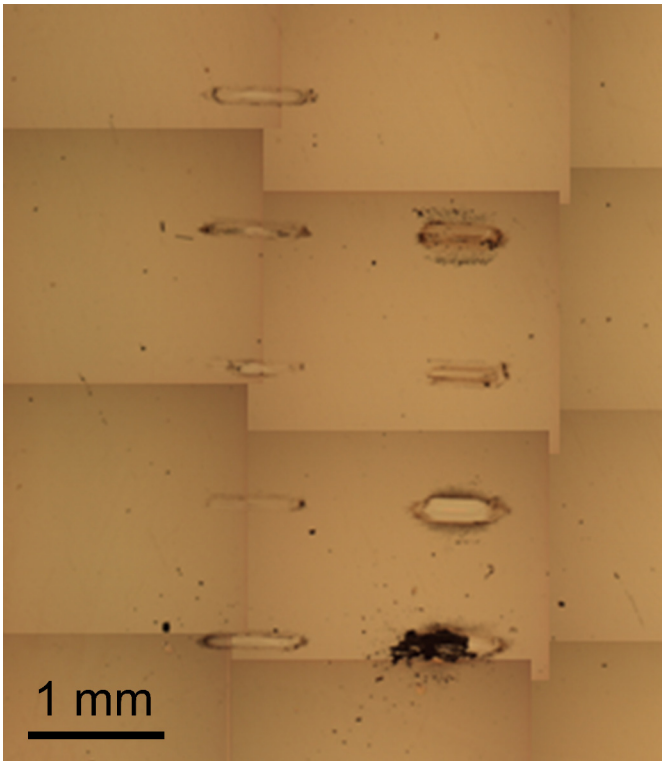

Fig. 2.7: Optical images of reciprocating wear tracks on a UNCD film

2.3 Profilometry

Scanning white light interferometry (SWLI) is a large area imaging technique that measures the 3D height profile of a surface with nanometer-level accuracy. It can be used

to measure the height of the debris and worn areas on the film surface. In addition to being a fast and reproducible, SWLI is a non-contact measurement method. This is especially important for tribological experiments because it means the height characterization will not affect the sample surface topography or chemistry, which would reduce the value of subsequent chemical measurements. The vertical resolution for this method is high (< 1 nm), but the lateral resolution is dependent on the optics and charge-couple device (CCD) camera used. For typical lens settings (20x objective, 0.5x internal magnification), one pixel encompasses ~1.1 x ~1.1 μm^2. This relatively large pixel size, combined with the smoothness of ta-C and UNCD, means that SWLI cannot accurately measure the surface roughness of these films below a ~1 μm lateral dimension. Wear tracks are typically ~50 μm wide (determined by the applied load and corresponding amount of contact area and wear) and ~600 μm long (determined by the stroke of the reciprocating wear tests). The optical objectives available allow measurements of the entire wear track in one FOV. Plotting the height profile in 3D shows the track profile (Fig. 2.8). From this, the average and maximum wear depth of different tracks can be compared. Additionally, by summing the volume of every pixel that has depth below the initial height, one can calculate the wear volume.

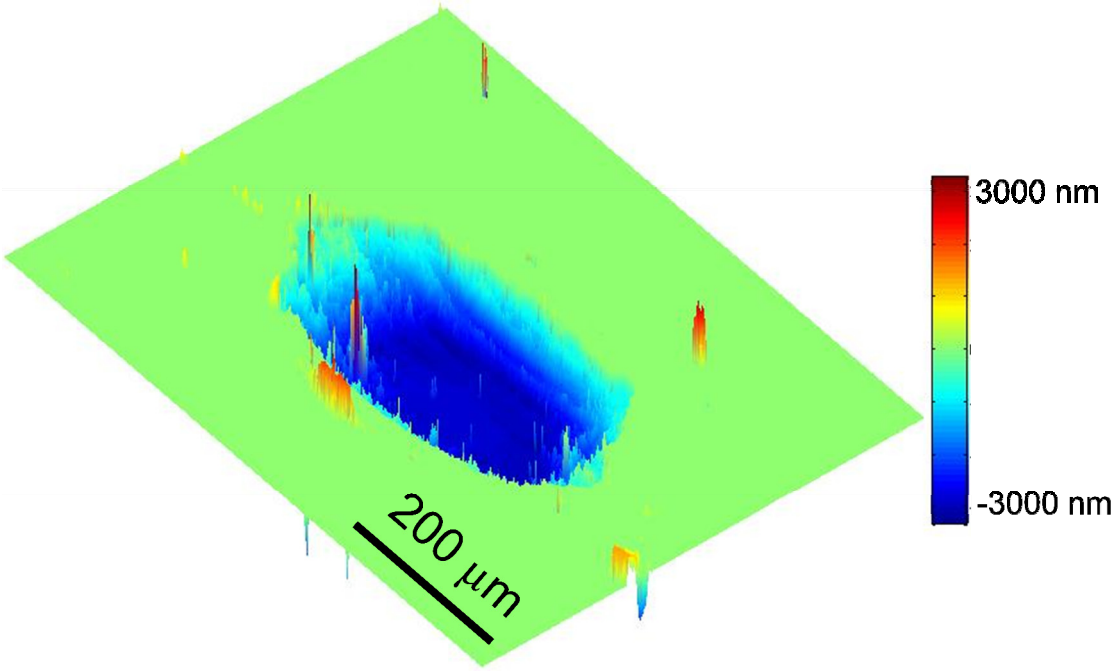

Fig. 2.8: Profilometry image of a UNCD wear track created at 1.0N, 1.0% relative humidity. The height scaling is amplified by a factor of 40 compared to the lateral dimensions.

The SWLI technique obtains height information as follows. An interference pattern is produced between light reflected from the test surface and the reflected light from a flat reference surface. This summed image is measured by a camera as a series of fringes caused by the constructive or destructive interference of light from the two surfaces. The technique is referred to as 'white light' because it is a light source with center wavelength of 546 nm, but has a 120 nm full width, so it emits a range of frequencies. Because of this, the beam has a finite coherence length. As the piezo motor ramps the objective and reference surface through a range of distances from the test surface, each point on the surface will have several heights with constructive interference (fringe maxima). However, due to the coherent nature of the beam, only one height will

give the brightest maximum. The software finds the height at which each pixel has a calculated maximum coherent interference with the light from the reference mirror, and then backs out a relative height value for that point. Because this technique relies on the intensity of the interference signal, sections of the surface that have poor reflection due to roughness or extreme geometry, such as a debris particle or the sidewall of a wear track, can sometimes produce dropped pixels.

To find the wear volume removed for each track, optical profilometry measurements are performed using a Zygo New View 6300 SWLI profilometer. An analysis routine with a graphical user interface (GUI) was designed as part of this thesis to convert the raw height data into a wear rate for the track. Data from a SWLI image are loaded in ASCII format, with the *x*- and *y*-dimension of the matrix representing CCD camera pixels, and the matrix value representing height in nm. The header file contains the conversion factors from pixel value to lateral dimensions. The images are then processed to remove artifacts and enable analysis of the wear volume. The first processing step is a plane fit. Due to the flatness and low roughness of the substrate, as well as the low roughness of these coatings, the as-grown film surrounding the wear track is treated as a plane. The user selects a region that includes all points in the image inside the wear track, and then these values are excluded from the plane fit. This fit is then subtracted from the data set, leaving the surface with the average of all non-wear track pixels centered at zero height. Any errant or missing points anywhere in the image are then flagged. Nonsensical data is identified by finding any pixel that is different in height by more than three times the standard deviation of the average of the surrounding pixels

in a 25x25 grid (excluding the center point itself). If a point is dropped during the initial measurement, meaning the Zygo output software sets the height value to be '2147483640', the Matlab code sets the value to not-a-number (NaN).

Then all of the flagged points are replaced by values determined from an interpolation using a spline fit curve (one for each orthogonal direction of the data set) to find the best estimate for the actual height. Only the heights of non-flagged data points are used in the interpolating fit. The two values from the interpolation are compared. If they are similar, the average of the two is used for the height. If they are very dissimilar, the one that is closer to the neighboring average is used. This may not be the most rigorous way to fix dropped data points, but the bulk of these errant points occur on areas of debris where the true height is above the zero plane. Profilometry analysis is mostly used for wear volumes and wear rates, and thus is only concerned with points below the zero plane. Finally, the user inputs the load used during tribometry, the track length, and the number of cycles.

Wear rate is then calculated using Archard's law, which states,

$$K = \frac{V}{N \cdot d} \tag{1}$$

where K is the wear rate, V is the volume removed (in mm^3), N is the normal load (in Newtons), and d is the sliding distance (in meters). The wear volume of the track is calculated by summing the depths of every pixel inside the track that is below the plane of the surrounding surface, and then multiplying those depths by the area of a pixel.

For a wear track that is 600 μm long and 50 μm wide, assuming the uncertainty in the height of every pixel is 1 nm, the number of pixels is determined by finding the total

area of the wear track. The shape is assumed to be a 600x50 μm^2 rectangle with two hemispherical ends with radius 25 μm. Then, using the 1.1x1.1 μm^2 pixel size with uncertainty of 3%, the total number of pixels in the wear track is found by dividing the wear track area by the pixel area. Finally, the uncertainty in the volume is calculated by multiplying the number of pixels in the wear track by the area of a pixel and the 1 nm uncertainty in height, giving 3.2×10^{-8} mm^3. Considering a track with the tribometry parameters that would give the highest uncertainty in the wear rate (ta-C with a minimum load of 0.05 N) for 5000 cycles and a 600 μm track length, this would be an uncertainty in the wear rate of 1.1×10^{-7} $mm^3N^{-1}m^{-1}$.

We also use the calibrated profilometry data to ascertain the worn area of the sphere. Wear scar diameter is found from a sphere height profile across the center of the scar. A good approximation for the wear scar is a circular shape. Assuming this, the wear volume for the sphere is calculated from the diameter of the wear scar and using basic geometry to calculate the removed volume. Since the sphere and the films are not ductile materials, plastic deformation is considered unlikely and the change in volume is entirely attributed to wear (removed volume).

Since the volume measurements are performed only once, at the end of the tribometer test, they are referred to as ‘single point’ wear rate values. As the majority of wear occurs in the first few cycles (typically the first 10 – 100), single point measurements do not provide steady-state wear rate information. Instead, they provide only an upper-bound value.

2.4 Near-edge X-ray Absorption Fine Structure Spectroscopy

The primary method used in this thesis for investigating the chemical structure of the surfaces of these materials is a synchrotron radiation technique, near-edge x-ray absorption fine structure (NEXAFS) spectroscopy [2.20]. This is an x-ray in, electron out spectroscopy technique. Monochromatic x-rays are incident on the sample. X-ray energies start below the ionization potential (*i.e.* absorption edge) of the specific element in question, and are increased until they are above the edge (hence the 'near-edge' in the name). Electron yield is collected as a function of incident x-ray energy, producing a spectrum. This technique reveals chemical information regarding the chemical makeup (the type of atoms) and chemical bonding state (how the atoms are bonded to other atoms) since the shape of the near-edge region is very sensitive to the local bonding. These spectra can be used as a chemical fingerprint of each film's surface character. Because synchrotron light is polarized, the spectra can also show differences based on bond orientation. The ordering that occurs in crystalline structures, as well as any ordered bonding between the surface atoms and adsorbates, produces a different electron spectrum depending on the angle between various bond directions and the light polarization vector. Electrons that make up the signal in an electron-yield NEXAFS spectrum come primarily from the surface of a material (top ~10 nm). Changes to the surface composition or bonding, as caused by friction and wear, show up in the spectra as variations in peak heights and locations. Comparisons of spectra before and after modification can then be related to the sliding conditions and environment. The surface

sensitivity is particularly important because it is the surface (or very near-surface) atoms that will govern the tribochemical interactions during sliding.

The measurement setup is designed to count the electrons emitted from the sample (*e.g.* as a drain current measurement obtained by connecting an ammeter to the conducting sample holder). The resultant data is plotted as the electron yield versus the incident photon energy. Electrons in the sample are excited into unoccupied anti-bonding states, given the right photon energy. They are usually excited from core-shell levels (Fig. 2.9a). For the carbon and oxygen data in this thesis all of the NEXAFS data will be *K*-edge data, meaning the first excited electrons come from the K shell of the atom. After this first electron is excited, a second electron from a higher level in the same atom will then relax into the hole that has been created (Fig. 2.9b). The Auger process is completed when a third electron (the Auger electron), at the same or lower binding energy as the second, absorbs the energy released by the relaxing electron and is ejected from the atom (Fig. 2.9c,d). By taking the binding energy of the first electron and subtracting the binding energies of the second and third electrons, one can calculate the initial kinetic energy of the Auger electron. For carbon, the typical *KLL* Auger electron energy is ~240-270 eV [2.21, 22]. In diamond, the inelastic mean free path of electrons with this energy is ~0.5 nm. In order to escape from the material and be collected as part of the measurement, the starting atom must be located very near the film's free surface. Electrons deeper in the sample will lose all of their kinetic energy before escaping.

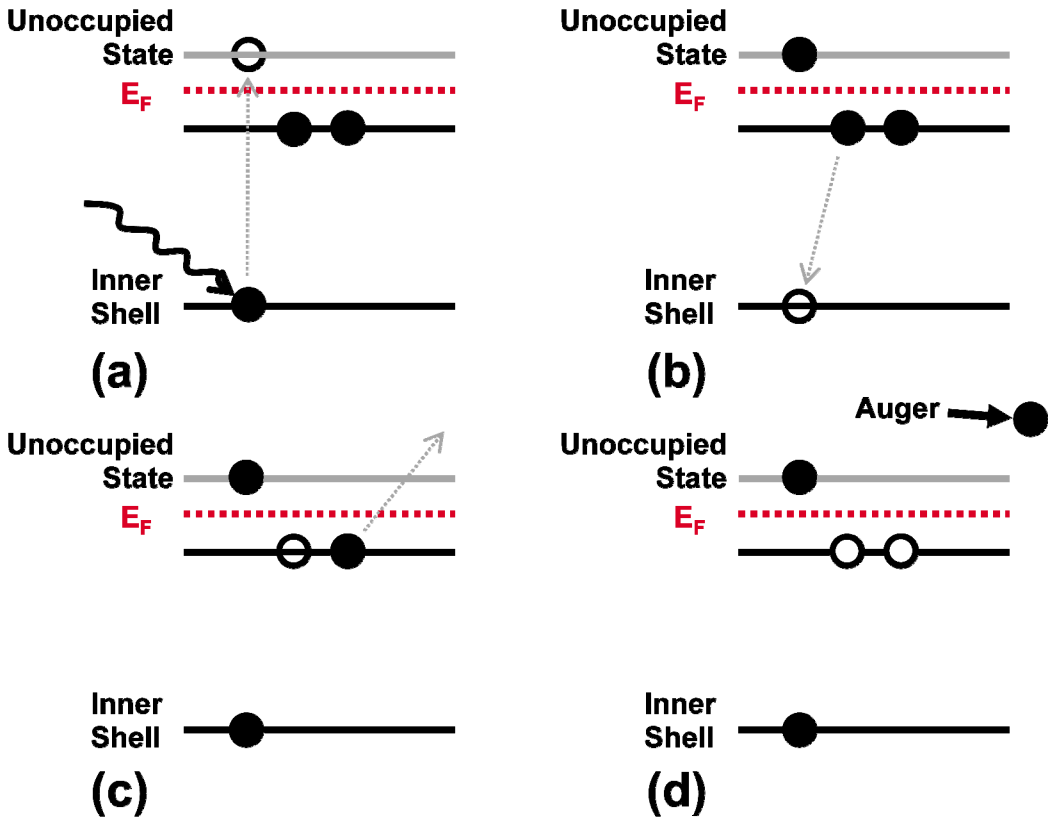

Fig. 2.9: Schematic of the NEXAFS electron process, showing (a) a photon excites a core shell electron to an unoccupied state, (b) an electron from a bound state relaxes down and fills the created hole, (c) because of the relaxation, an Auger electron is ejected, (d) this Auger electron inelastically scatters to produce further secondaries.

However, the bulk of the measured signal does not come from the Auger electrons, but from the secondary electrons produced during subsequent inelastic scattering events. As many as 40 electrons can be produced in cascade events resulting from the initial Auger electron [2.23]. These electrons will have lower energy than the Auger electron and have longer mean free paths. The effect of separating the contribution of these secondary electrons from the Auger electrons will be discussed below.

Much of the early NEXAFS work for this thesis was taken at the Synchrotron Radiation Center (SRC), Stoughton, WI, on the Hermon beamline, port 33. This beamline has an energy range of 62-1400 eV, with a photon flux (photons/second/mA) of ~$2x10^6$ at the carbon edge (300 eV). The beam size on the sample is ~1x3 mm^2. The later NEXAFS work was performed at the National Synchrotron Light Source (NSLS), Brookhaven National Laboratory, Upton, NY. The instrument is on a National Institute of Standards and Technology owned beamline, U7A, and is pictured in Fig. 2.10. The photon source is a bending magnet, and covers an energy range from 180-1600 eV. The flux is $2x10^{11}$ photons/second/0.1% bandwith, and resolution ($\Delta E/E$) of ~$1x10^{-3}$.

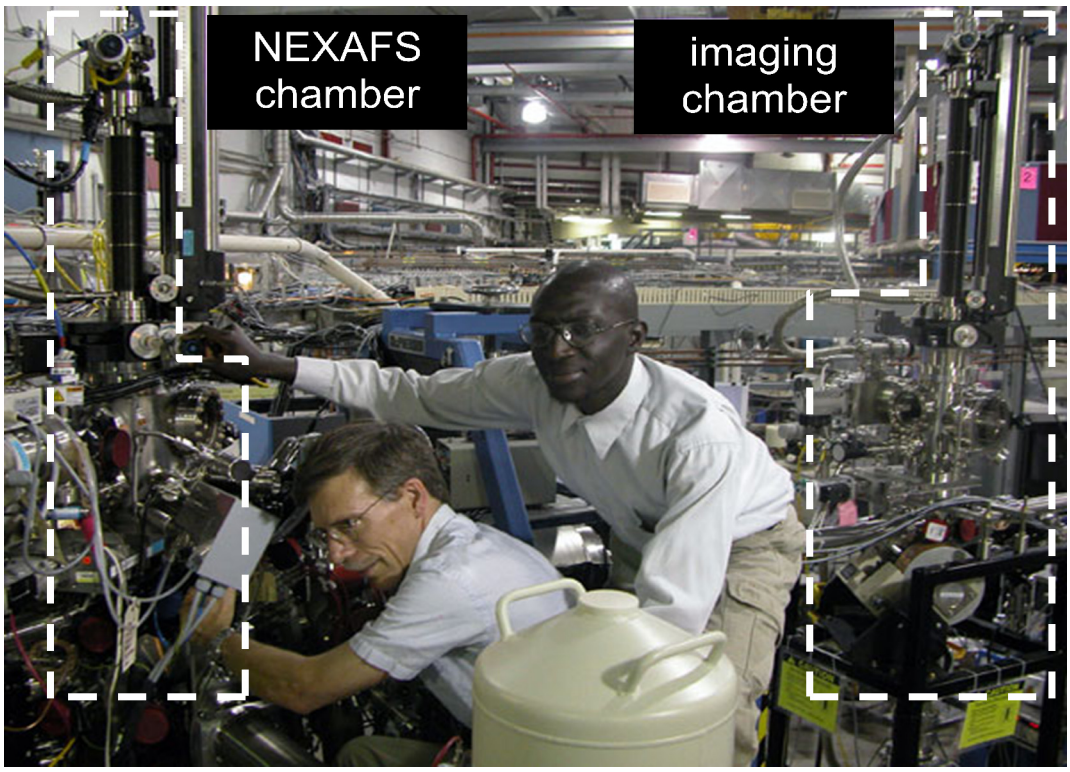

Fig. 2.10: Photograph of the NEXAFS chamber (left) and imaging chamber (right) at the NSLS, beamline U7A. Shown are the beamline manager, Dan Fischer (left), and his postdoc, Cherno Jaye (right).

The current state-of-the-art in NEXAFS modeling makes predicting these spectra very difficult, and existing models are often only semi-quantitative, if at all [2.24]. One method that uses *ab initio* single-scattering calculations, FEFF [2.25], has gone through several revisions over the last ~20 years. The name FEFF comes from the theory's effective curved-wave scattering amplitude, f_{eff}. With knowledge of the atomic numbers, coordination numbers, and nearest-neighbor distance of each atom, the model produces a simulated NEXAFS spectrum that has many of the same features as the measured spectrum (though the agreement is worse at energies near the adsorption edge). This model can often correctly assign the absolute energy scale for the spectra (as this is a variable in the calculation). Predicting the relative peak heights is generally accurate. However, the absolute peak positions and heights do not fully agree between calculated and measured spectra. This is due to the complexity involved in solving the equations for the photon adsorption and electron emission of the system. As the authors themselves state, "An adequate molecular potential based on relativistic atomic potentials is found to be essential for an accurate description of [NEXAFS spectra]." [2.26]

As previously mentioned, the photoelectrons can be collected with an ammeter measuring a current. The ammeter replenishes the electrons that have been emitted from the sample. This collection mode is known as total electron yield (TEY) as all electrons that leave the sample are measured. In some systems there is a positively biased grid placed near the sample surface that further attracts electrons. This grid is intended to reduce noise by preventing the electrons from interacting with the sample after they are emitted. A second collection method involves a collector that faces the sample and is

screened by a grid with a negative bias. This method is called partial electron yield (PEY) since the negative grid bias prevents low energy electrons from reaching the collector. The bias voltage is usually set to a level that is high enough to repel the low energy secondary electrons, but will still allow the primary and Auger electrons to pass. The main effect of PEY is to increase the surface sensitivity of the measurement by removing most of the secondary electrons from the signal. These electrons were produced by the inelastic scattering of the higher energy Auger electrons and emerge from further in the bulk of the sample because these lower energy electrons have longer mean free paths. In this thesis, all NEXAFS spectra reported are total electron yield unless specified otherwise.

A critical step when mounting the samples to the sample holder for measurement is proper grounding of the sample surface. Synchrotrons are an extremely bright source of photons. Because of this, the number of photoemitted electrons from the sample surface, at photon energies higher than the adsorption edge, is also high. Since most of these films are coated on silicon substrates, there is a very poor conduction path through the film, the silicon substrate, and to the sample holder. Carbon tape is placed so that it provides a better conduction path between the sample holder and the surface of the film (where the electrons are leaving). While the carbon film might not be very conducting (undoped UNCD, for example, is not much more conducting than single crystal diamond), the conduction path over the sample surface a better alternative. Failure to ground the sample can cause errant data due to discharges of electrons as the sample becomes positively charged.

Upstream from the sample and collector is a gold mesh which absorbs a fraction (usually ~ 15%) of the incident x-rays. An ammeter is connected to this mesh and the photocurrent is measured as a function of photon energy. This spectrum (called the normalization spectrum, reference spectrum, or I0 spectrum) is needed to properly normalize the electron spectrum from the sample. Due to contamination in the beamline optics, as well as a decreasing synchrotron ring current as a function of time, the photon fluence on the sample surface is not a constant. Normalizing the measured sample signal by the simultaneously-acquired reference signal removes these effects. This is done by dividing the sample spectrum, point-by-point, by the reference spectrum.

A specific normalization process is performed on all samples. First, the raw sample and I0 spectra (Fig. 2.11a,b) are normalized such that intensity values (at all photon energies) for the spectra are divided by the value of the average intensity of their pre-edge region (flat region before any adsorption features, *e.g.*, 275-280 eV in Fig. 2.11). Obviously, this normalizes the pre-edge region of both spectra to unity (Fig. 2.11c). The raw intensity of the pre-edge for either the sample or the reference depends on several factors, such as the synchrotron ring current, the beam dispersion character, and the monochromator profile. However, by dividing every spectrum such that the pre-edge is at the same value, all of these effects have nominally been normalized out. At this point, when the sample spectrum is divided by the I0 spectrum, the absolute intensity of the normalized spectrum is related to the chemical content of the sample. To then compare different spectra specifically to look at ratios of bonding changes in the pre-edge region, the final step is to subtract the pre-edge region to zero and then divide the post-

edge region (typically an average around 320 eV for carbon) to one (Fig. 2.11d). If necessary, a linear fit is performed on the pre-edge and subtracted from the entire spectrum. This removes effects from the different absorption profile between the sample electron collector and the reference electron collector. Finally, the energy axis for the data is corrected. Due to the nature of the beamline optics, the absolute photon energies are never exactly correct. This shift can be corrected in some cases by using known features in the reference spectrum. For example, the main dip in a carbon I0 spectrum taken on the Hermon beamline at the SRC is located at 284.57 eV. By calculating the difference between the dip in the measured I0 spectrum and this known value, both the I0 spectrum and the sample spectrum can be shifted to the correct energy. For most beamlines this type of feature isn't well known. In that case the spectra are shifted using known features of the unmodified material, such as the C 1s→π* transition for ta-C at 285.0 eV, or the location of the exciton feature at 289.3 eV for UNCD.

The above normalization process works very well for elements in abundance, but it should be noted that it is not always possible for other elements that have a lower concentration. For instance, oxygen is a small component of as-grown ta-C and UNCD films. Taking oxygen *K*-edge data on these samples will measure a weak signal that is less distinguishable from the background shape of the x-ray flux. Because of this, the line shape overall is tilted, mirroring the profile of the incident beam flux. When this occurs it rarely makes sense to attempt to linear fit or post-edge normalize these spectra. As such, they are often presented as only processed after the I0 normalization (right after the division in Fig. 2.11c).

Fig. 2.11: Example of NEXAFS data taken at the SRC showing (a) raw sample data measured as current vs. photon energy, (b) I0 spectrum as current vs. photon energy, (c) sample and current spectrum after pre-edge division to one, and (d) normalized spectrum with pre-edge subtraction to zero and post-edge division to one

A second critical processing step is determining the absolute energy position of the spectrum. There is always some variability (as high as ~5 eV) in the absolute energy set for the monochromator as compared to the actual photon energy. There are different techniques for correcting this discrepancy. In some beamlines, the absorption features in

the reference spectrum are well defined and the energy axis can be shifted to line up these features with known values. In other beamlines, there are additional transmissive references placed upstream of the sample with features at known energies. When neither of these are feasible, it is possible to shift the energy based on knowledge of the known features of the samples being measured.

The ‘near-edge’ part of NEXAFS refers to the fact that the photon energies are selected near the absorption edge for the element being probed. For carbon, these energies are generally between 280-320 eV; for oxygen, between 520-560 eV. The unoccupied anti-bonding energy levels of covalent bonds are very sensitive to the local bonding environment. This phenomenon is what causes the spectra to depend markedly on the bonding configuration. In essence, a NEXAFS spectrum is a plot of the core-hole perturbed density of unoccupied states, using core electrons as a fine-tuned probe of the available states near and above the Fermi level. The anti-bonding levels are near the absorption edge for an element. This absorption edge, or 'edge jump', is a sharp increase in the number of electrons that occurs at the ionization energy for the atom. Incident photons with this energy or higher can ionize electrons completely from the atom, and not just into bound, unoccupied states.

NEXAFS is the exact same process as x-ray absorption near-edge spectroscopy (XANES) except that, by convention, NEXAFS is the term used for spectroscopy performed at lower x-ray energies (less than 1000 eV). It is distinguished from extended x-ray absorption fine structure (EXAFS) spectroscopy, which measures the absorption spectrum over a much wider energy range, including energies more than 50 eV above the

absorption edge. NEXAFS also is distinguished from x-ray photoelectron spectroscopy (XPS). XPS typically uses monochromatic x-rays of a fixed energy to excite and collect primary electrons. By energy analyzing the emitted electrons, an XPS spectrum is a plot of number of emitted electrons versus their binding energy. XPS is less sensitive to local bonding changes than NEXAFS, since the core electron levels measured in XPS do not vary as much depending on the type of bond and to what the atom is bonded.

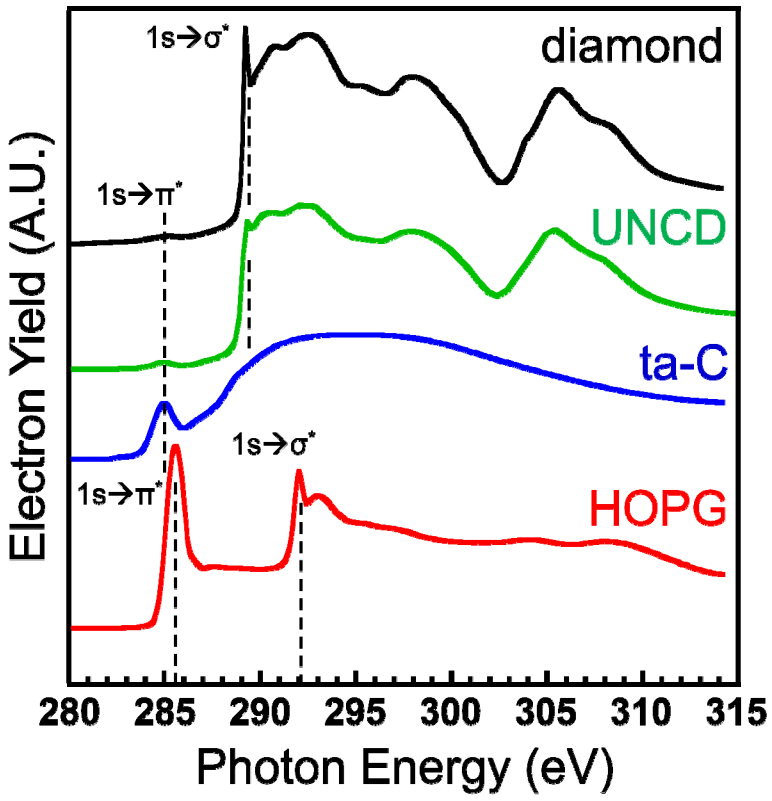

Fig. 2.12: Reference NEXAFS spectra for relevant carbon materials

Fig. 2.12 is a plot of reference spectra for single crystal diamond, UNCD, ta-C, and HOPG taken at the SRC. The HOPG spectrum has a strong peak at 285.5 eV which

is due to a C 1s→π* transition for ordered sp^2-hybridized carbon [2.27, 28]. This is a transition of an electron from a 1s core state to an unoccupied π anti-bonding state, referred to as π*. The spectrum also has a peak for the C 1s→σ* transition at ~292 eV. These relative peak positions can be understand from a bonding energetic standpoint. The σ bonding state is the lowest energy, with π bonding states being slightly higher. The corresponding anti-bonding states are in reverse order, with π* states being lower than the σ*. This is because the low energy state for a bond depends on the amount of overlap of the molecular orbitals. A bonding state is shaped like the sum of the two orbitals, and the anti-bonding state is shaped like the difference. Two atoms sharing a σ bond, with orbitals pointing along the bond direction, have a larger degree of overlap than two atoms sharing a π bond, with orbitals pointing perpendicular to the bond direction. Likewise, the anti-bonding states for either σ* levels have a greater energy disparity from their σ levels than π* levels from π. This also explains why the HOPG σ* feature (~292 eV) is at a higher energy than the diamond σ* feature (~289 eV), as the shorter HOPG bond length means that the orbitals overlap more than in diamond.

Typical carbon 1s spectra for ta-C have two primary identifying spectroscopic features. The first is a peak at 285.0 eV due to the C 1s→π^* transition for disordered sp^2-hybridized carbon atoms. There is a distinct shift that exists for energy of the π* orbital for ordered versus disordered sp^2-bonded carbon, with the peak for disordered bonds being 0.5 eV lower. This can be explained by the fact the ordered bonding in graphite has π orbitals with a lower energy state than those for amorphous carbon. This means the anti-bonding state for graphite will be at a slightly higher energy. Since the binding

energy of the primary electron is at approximately the same level for all transitions, the difference in anti-bonding energies is seen as a peak shift. The second feature is a broad hump due to the C 1s→σ^* transitions for both sp^2- and sp^3-hybridzed C atoms that begins at ~289.0 eV. Since ta-C is amorphous and contains a range of bond lengths, the C 1s NEXAFS spectra lack any sharp post-edge resonances.

For as-grown UNCD, the small peak at 285.0 eV is due to the C 1s→π* transition for disordered sp^2-hybridzed carbon, as in ta-C. Analyzing the intensity of this peak allows one to determine the amount of sp^2-bonded carbon in the region of the film sampled by the NEXAFS measurement, which is found to be ~5%, similar to all UNCD films [2.29]. The sources of this sp^2-bonded carbon are surface contamination, surface reconstruction, and grain boundaries. The edge jump at ~289.0 eV, the exciton peak at ~289.3 eV, and the second band gap at 302.5 eV are all due to the C 1s→σ* transition for ordered sp^3-hybridized carbon-carbon bonds [2.20]. Single crystal diamond shares the same features as UNCD, except that the peak at 285.0 eV is even less pronounced. Since diamond is, ideally, composed of 100% sp^3-bonded carbon atoms, there should be no feature related to π-bonded carbon. However, there is still some intensity at that energy, and it is likely due to surface reconstruction and some surface contamination. Hydrogen terminating a single crystal diamond sample leaves the surface entirely in the sp^3 coordination, and in that case, the C-H bonding C 1s→σ* feature appears at 287.5 eV.

There is a method to calculate the fraction of sp^2-bonded carbon in polycrystalline diamond samples. It is based on the ratio of the C 1s→π* peak area and the area after the

C 1s→σ* transition for the sample spectrum and for a randomly oriented, 100% sp^2-bonded carbon reference film. The equation for the sp^2 fraction is

$$f_{sp^2} = \frac{I^{\pi^*}_{sam} I_{ref}(\Delta E)}{I^{\pi^*}_{ref} I_{sam}(\Delta E)} \tag{2.1}$$

where $I^{\pi^*}_{sam}$ and $I^{\pi^*}_{ref}$ are the areas of the C 1s→π* peaks for the sample and reference, respectively, as fitted by Gaussian peaks to the data line shape. $I_{sam}(\Delta E)$ and $I_{ref}(\Delta E)$ are the areas under the curve from 288.6 eV to 325 eV for the sample and reference, resepectively [2.30]. The higher energy cutoff is chosen rather arbitrarily, and is generally determined by the energy range over which NEXFAS data was taken. While not quantitative, a qualitative assessment of changing the cutoff energy results in little variation of the calculated sp^2 fraction. While the areal intensity of the spectrum will increase or decrease with a higher or lower cutoff energy, it also increases and decreases for the reference spectrum. An example of this calculation is shown in Fig. 2.13 for a UNCD spectrum. The calculated sp^2 fraction for this UNCD spectrum is 4.8%.

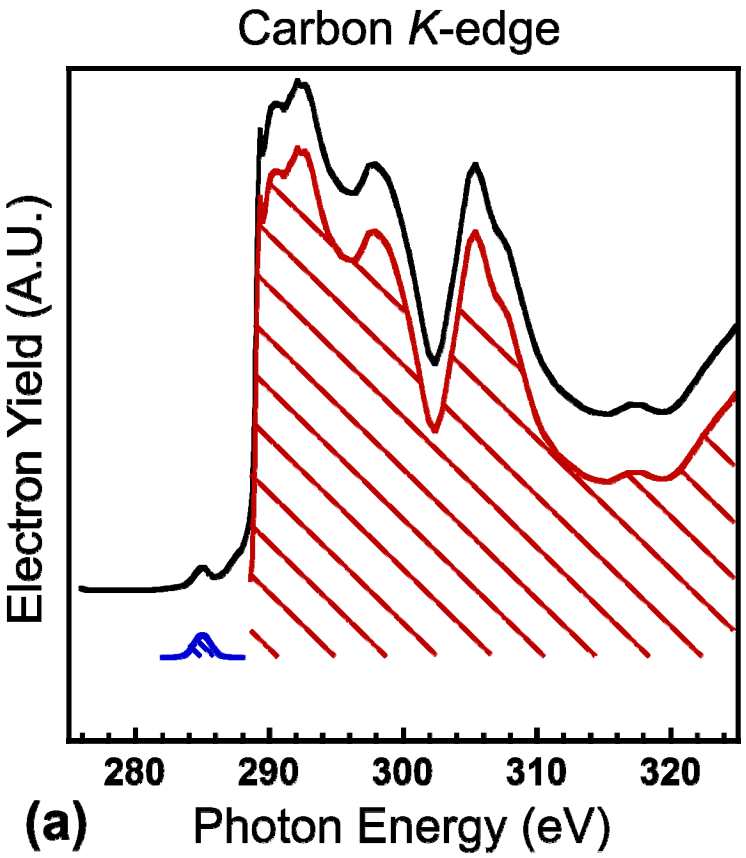
Carbon K-edge
Electron Yield (A.U.)
280
290
300
310
320
(a)
Photon Energy (eV)

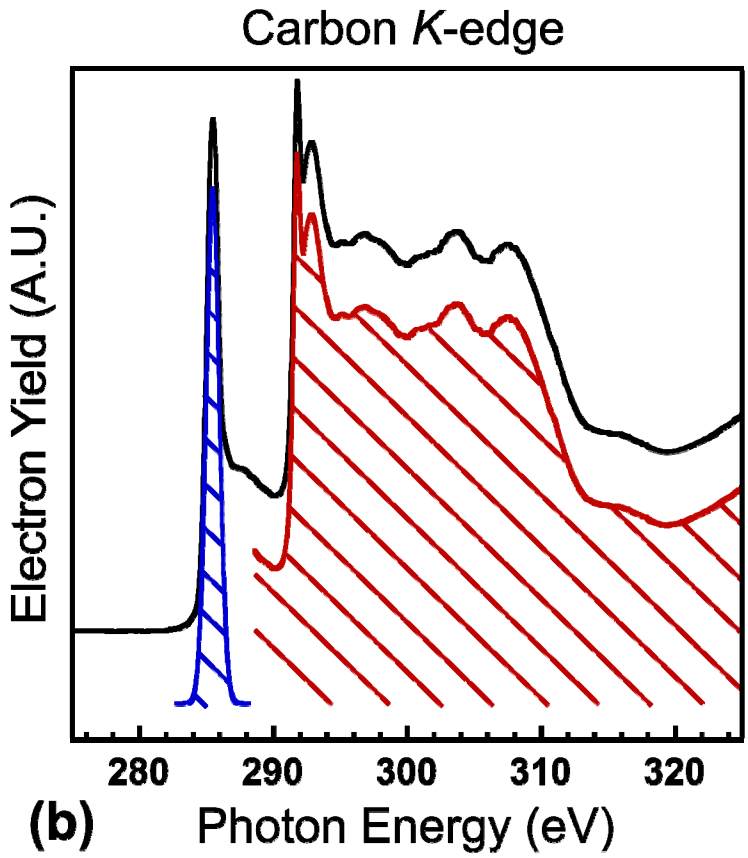

Fig. 2.13: (a) UNCD spectrum (black). The blue and red curves have been shifted down for clarity. The blue lined area is a Gaussian fit to the C 1s→π* peak, and the red lined area is from 288.6 eV to 325 eV. (b) HOPG spectrum (black). Blue and red sections are the respective HOPG regions.

2.5 PEEM

Wear tracks are analyzed *ex-situ* using photoelectron emission microscopy (PEEM). PEEM is a surface-sensitive technique that characterizes the top few nm of a sample with high lateral resolution [2.31]. Lateral resolution better than 50 nm can be routinely achieved, and resolving features as small as 10 nm have been reported [2.32]. The benefit PEEM yields for tribochemical studies, beyond high spatial and energy

resolution, is its ability to produce full-field spectroscopic images that include both worn and unworn regions of a sample (Fig. 2.14).

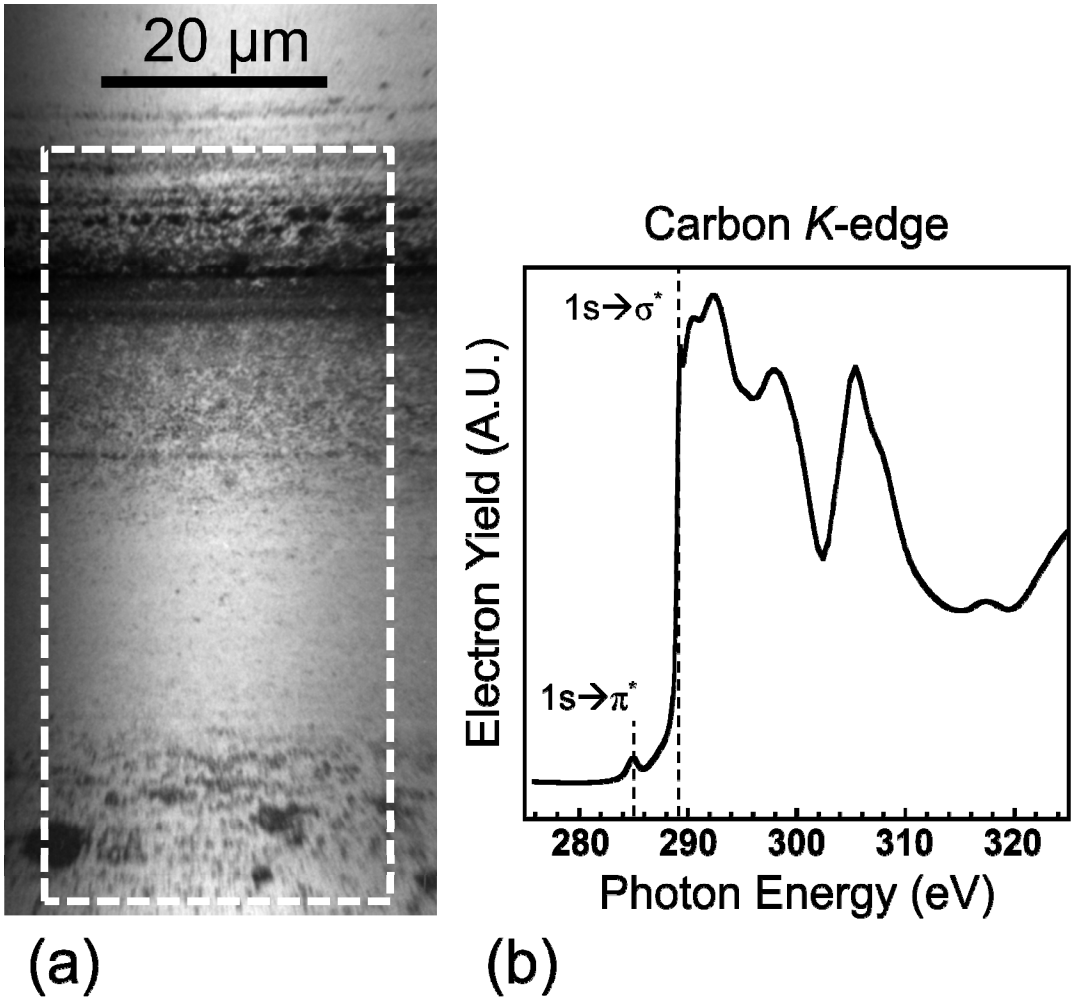

Fig. 2.14: (a) Example PEEM image (taken at 289 eV), and (b) extracted and normalized spectrum from highlighted region in (a)

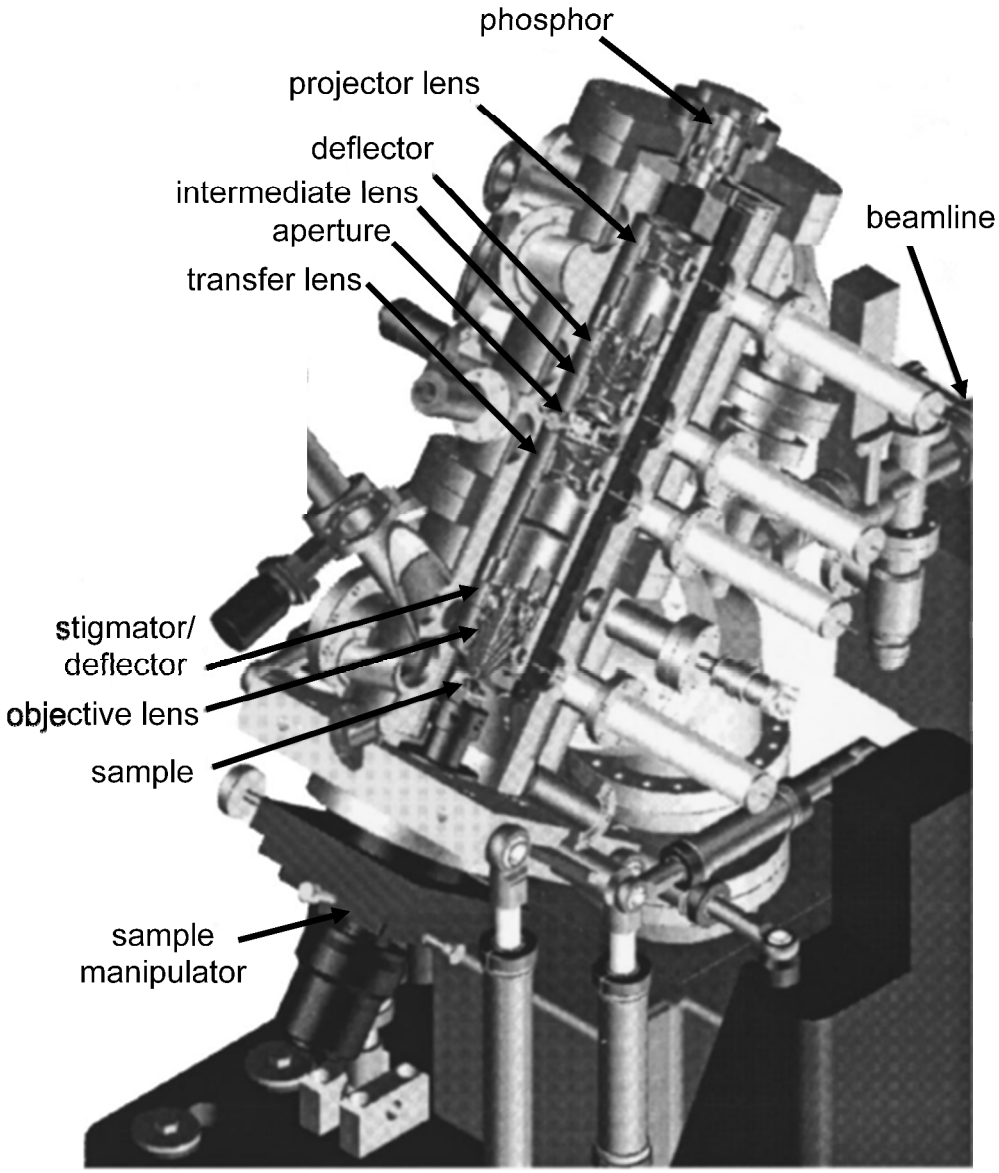

Fig. 2.15: Image of the optics column layout for PEEM2 [2.31]

The particular system used for the work presented here is called "PEEM2" and it is located on beamline 7.3.1.1 at the Advanced Light Source, Berkeley, CA. This beamline utilizes a bending magnet source with a spherical grating monochromator for photon energies between 175-1500 eV. The flux is $3x10^{12}$ photons/s, with a 0.1%

bandwidth at 800 eV, where the resolving power ($E/\Delta E$) is 1800. The quoted spatial resolution is 100 nm for typical samples. Previous work was performed on the spectromicroscope for the photoelectron imaging of nanostructures with x-rays (SPHINX) instrument on the varied line space plane grating monochromator (VLS-PGM) line, port 41, at the SRC. The VLS-PGM beamline supplies photons between 70-2000 eV from a permanent magnet undulator source. The flux is ~$4x10^{11}$ photons/second/mA at the carbon edge.

PEEM can be combined with NEXAFS to study tribological systems [2.33-35], and has been previously used to study UNCD [2.36, 37]. A schematic of the technique is shown in Fig. 2.16. Monochromatized x-rays are incident at a glancing angle on the sample (a geometric concern since the measured area is only a couple millimeters below the electron optics column). The sample is held at a large negative bias (-15 to -20 kV). Because of this large bias, samples need to be flat or nearly flat, as any features on the surface with even mild aspect ratios will locally concentrate the electric field. At such points, the bias causes field emission which, at best, distorts the electron images and, at worst, causes arcing between the sample and microscope. These effects prevent imaging due to aberrant electron emission.

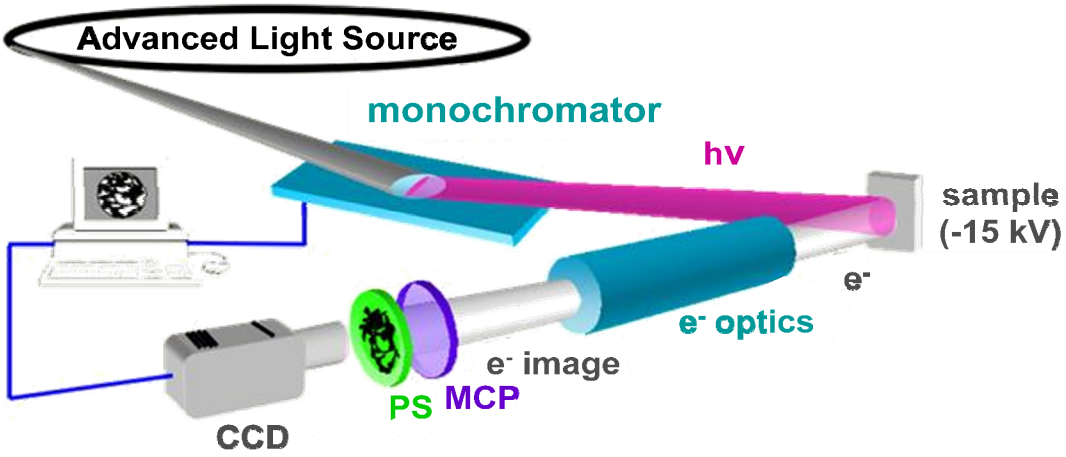

Fig. 2.16: Schematic of the PEEM data collection process

Photoelectrons are produced in the same process as described in Section 2.4 and accelerated by the applied field from the sample toward the electron optics column. For PEEM, the entire range of primary, Auger, and secondary electrons are sent through the aperture of the first lens of the microscope. Because of the spherical and chromatic aberrations of the electron optics, electrons emitted from the sample that have higher kinetic energy (primary and Auger electrons emitted near the sample surface), or are emitted at angles other than the surface normal, have different focal lengths. [2.38]. In order to obtain higher resolution images, the optics column for PEEM2 has an aperture located in the back focal plane of one of the lenses. Electron efficiency of the optical column is traded for spatial resolution in the final image by physically stopping those electrons that do not focus at the plane of this aperture. The path of these electrons take them further outside the circle of confusion (a measure of the area and depth of field that electrons with different energies/trajectories will be collected from), and the aperture prevents them from being imaged. In this way the aperture acts like a partial bandpass

filter for the electrons, accepting the largest part of the signal from the secondary electrons that have kinetic energy roughly equal to the work function of the sample. However, electrons that are emitted near the center of the image and leave the sample normally, regardless of energy, will be imaged. The aperture acts only as a spatial filter in the back focal plane, and thus is not a true energy bandpass filter.

Overall, the signal from PEEM is closest to TEY, since excluding the higher energy electrons does not noticeably change the spectral character. The secondary electrons still account for the largest fraction of all collected electrons, for both NEXAFS and PEEM. After the optics column accelerates, filters, and focuses the electrons (Fig. 2.15), they are directly converted to visible light by a phosphor coated fiber optic bundle. The resulting image is captured by a charge coupled device (CCD) camera (Fig. 2.15). The photon energy is incremented and another image is captured. By varying the photon energy over the same range as a typical NEXAFS spectrum for a given element, a stack of images (referred to as a 'movie') is captured where each pixel represents a spatially resolved NEXAFS spectrum.

In this work, prior to inserting a sample in the PEEM, the entire sample is coated with platinum except for the areas with wear tracks which are typically masked off by pieces of silicon or machined flat screw heads Fig. 2.17. This is, in part, to help with the same grounding issues described in Section 2.4. As with NEXAFS experiments, sample surfaces should be grounded with carbon tape. Careful grounding is even more important in the case of PEEM. While photons will cause photoelectrons to be ejected from the sample, there is also a high bias that is pulling the electrons into the microscope to be

imaged. Without a suitable path to replenish electrons to the sample, the system can build up a positive charge (causing image artifacts and drift) or arc due to a burst of emitted electrons. The other reason for the platinum coating is to provide *in-situ* normalization for the data acquired on the regions of interest. A fresh platinum coating should contain only trace amounts of carbon and oxygen (the main species that contaminate beamlines, and of extreme importance to this work). Similar to the gold mesh normalization discussed in Section 2.4, a movie taken on a platinum coated region of the sample will provide a spatially resolved, pixel-to-pixel, normalization for the data. This is important because in PEEM-II there is some degree of energy dispersion of the incoming photons along one axis of the image. However, by using an exit slit in the beamline before the chamber to fix the specific range of photon energies, and by using the sample-microscope distance to locate the beam, the ~exact same range of photons can be used on different samples. The microscope optics are used to fine-tune the objective focus. In this way, a movie taken on an area of interest and a movie taken on a Pt calibration area will have the exact same energy dispersion.

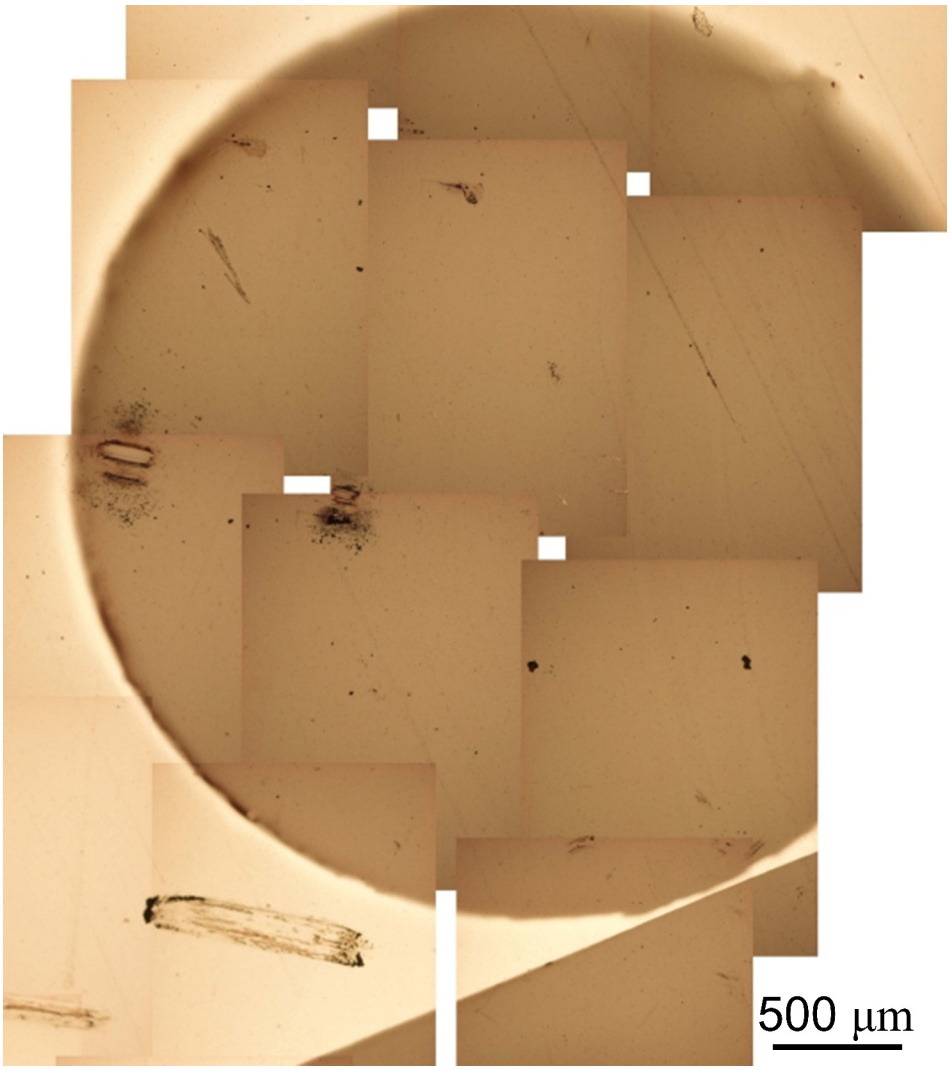

Fig. 2.17: Optical image of UNCD substrate coated with platinum (light colored areas)

The movies acquired in these studies are normally chosen to come predominantly from the center of each track. Due to the acceleration and deceleration at the ends of each track, the center is where the exposure time and friction are best controlled and measured. The edges of the track are also investigated in order to characterize the debris. The

chemical changes between outside the track and inside the track are related to the sliding conditions.

PEEM data analysis involves extracting spectra from regions of interest (ROIs) in each movie of interest. The software sums the intensity of every pixel from inside the ROI of each image, and then divides the sum by the number of pixels to get an average intensity. Each spectrum is plotted as the averaged intensity versus photon energy. Then the exact same ROIs are extracted from the platinum movie (which has been taken with the exact same magnification, photon energy steps, and will have the same photon energy dispersion characteristics). Normalization to the photon flux occurs by dividing each sample spectrum by its respective I0 spectrum, just like as described in Section 2.4 for bulk NEXAFS data. This step is required to allow spectra to be acquired between different movies or even from different ROIs within the same movie because the photon flux at a given point on the sample may not be uniform. There are also factors that affect the electron emission character from a sample, such as local topography. Key ROIs are from areas such as parts of the wear track, debris, or the unmodified film. During analysis, there is also one ROI that encompasses every part of the wear track visible in the movie. This is to obtain the average chemical signature of the wear track. Often, certain striations in the wear track (from points that were in intimate contact or not in contact) can have significantly different chemical signatures. Comparing different tracks with such ‘extreme’ spectra would prove meaningless. However, comparing average changes is both meaningful and reproducible.

A way of intelligently selecting the ROIs is to make an image that is the division of an image at an energy of a specific spectral feature by an image that is in the pre-edge region. These images are called division maps, or “div maps” for short. Each spectrum from every pixel has its own relative intensity profile that can be affected by the beam shape, local topography, and chemical content. By dividing the images pixel-by-pixel between two energies on and off bonding features, each pixel then shows the relative amount of the 'on' feature content. A single image can be used, or an average of a small range of images centered around the energy of interest. Fig. 2.18 shows this process for an 'on' feature energy of 287.8, representing carbon-oxygen bonding, and the 'off' image at 279 eV. The lighter areas in Fig. 2.18c are stronger outside the track, showing that it is likely debris that has been oxidized and shows a stronger signal. These div maps can then be used to draw ROIs on images of actual data. In this case, Fig. 2.18b shows that the image at 279 eV displays some contrast, but if the image at just 287.8 eV alone was looked at, these regions would not stand out.

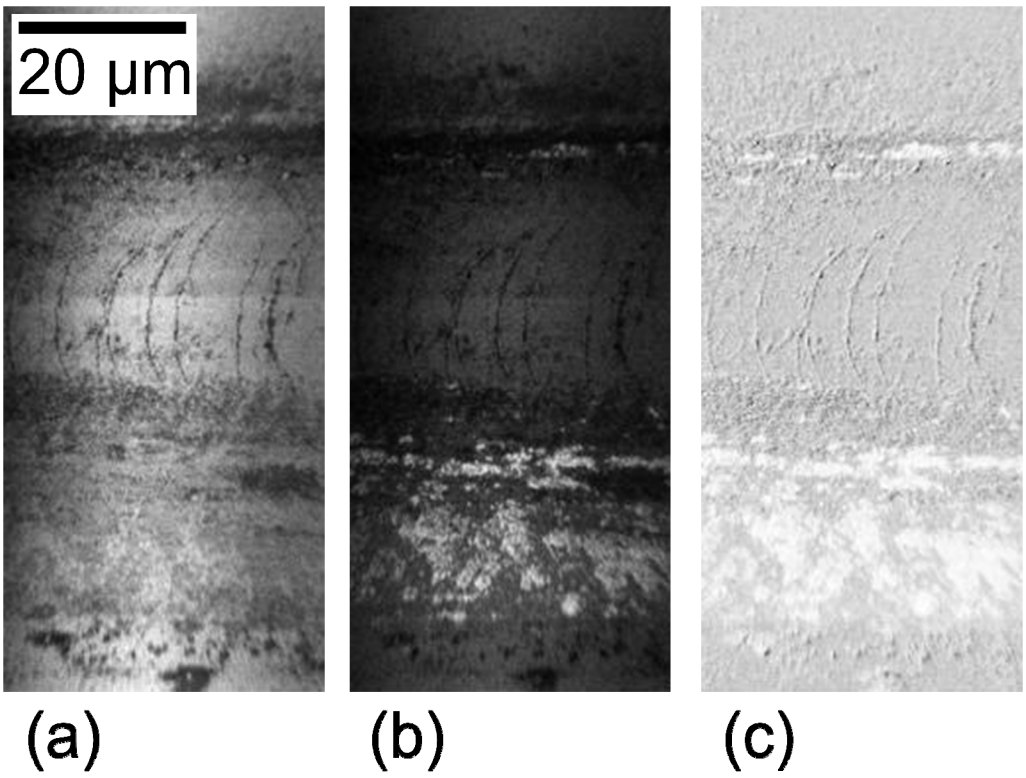

Fig. 2.18: Images used to create a division map. (a) Image at 287.8 eV, (b) image at 279 eV, and (c) division of (a) by (b) with the gray scale such that bright areas have more intensity at the 287.8 feature

For this thesis, a batch processing software routine with a GUI was written in MatLab to perform all analysis. The software code is included in the Appendix. Spectral data from files that have been systematically named according to a convention specified in the Appendix are stored in matrices in pairs. One contains the sample spectra and the other the platinum spectra. The code then automatically normalizes each sample spectrum with its respective platinum spectrum. Subsequent processing of PEEM data is performed in the same manner described in Section 2.4 for NEXAFS data. There are four plots produced from the resultant normalized data. The first is simply a plot of the normalized spectra with the pre-edge of each subtracted to zero (after the division in Fig. 2.11c). The

second plot has had an additional linear fit to each pre-edge which is then subtracted from the entire spectrum. When there is a significant amount of the element being probed, this is often an unnecessary step. However, when there are only trace amounts of the element, the ratio between the absorption in this pre-edge area for the sample is different enough compared to the reference spectrum that the slope of the pre-edge is not zero. Part of this comes from the fact that the electron emission profile decays as x-ray energy increases, and the other factor is the difference in the absorption/emission profiles between the sample spectrum and the reference spectrum. A linear fit corrects for this difference. The third spectrum is after the post-edge (region ~30-40 eV after the absorption feature) has been normalized to unity. In this post-edge region (EXAFS), the spectral features are typically oscillating around a slowly decaying value due to modulation of the transition probability of electrons by the interference of electron waves scattering inside the material [2.39]. By normalizing this region to the same value, relative differences in the pre-edge features are more easily distinguished by the unaided eye. This is essentially a simple way to determine which pre-edge features are different by simply examining their respective peak heights, since this step effectively normalizes all spectra to the area under the curve. The final plot uses the same data from the third plot, but vertically separates each spectrum by an additive factor. This is so that features between spectra can be compared without the spectra overlapping and hiding details of their line shapes. All of this processing and plot creation is done to present the researcher with various ways to examine the data with a range of processing levels.

After the pre-edge normalization and division of the spectra (described as the 'first plot' just above), the only remaining differences will be line shape anomalies (different peaks relating to unique chemical bonding compositions of the sample) and total spectrum intensity (due to amount of atomic content). This is useful to compare if different regions of a sample have more or less of a certain element. For the carbon tribology studies in this thesis, it is often an indication of oxidation. As an example, consider a carbon film that has part of the FOV oxidized. The C 1s spectrum from the oxidized region would have an overall lower intensity than the spectrum from the non-oxidized region because there fewer C atoms sampled in the former spectrum (Fig. 2.19a). The O 1s NEXAFS spectra would show the opposite trend (Fig. 2.19b).

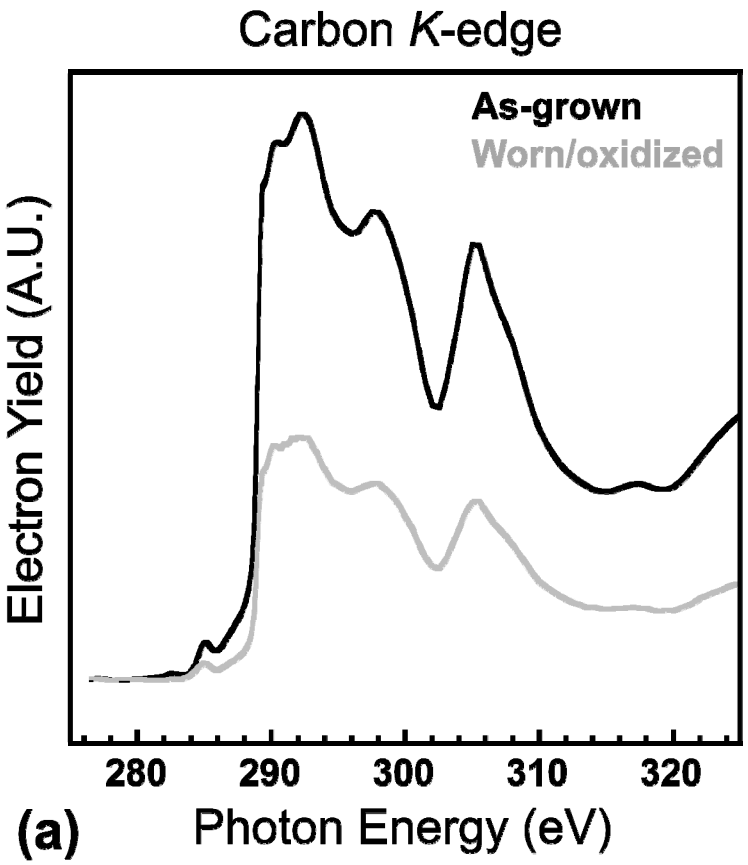

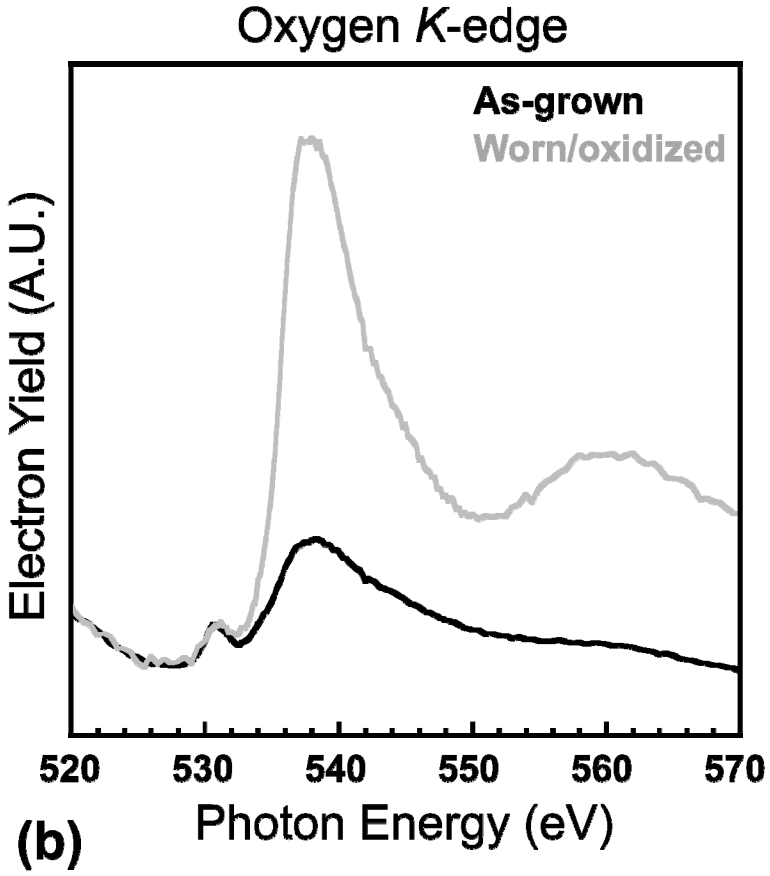

Fig. 2.19: NEXAFS data on as-grown and a worn/oxidized UNCD sample where (a) shows that the carbon intensity from the oxidized region is weaker than the as-grown spectrum, and (b) shows the opposite trend for the oxygen spectra

2.6 Chemical Mapping

Part of this thesis work involved writing computer code to take the idea of division maps (discussed in Section 2.5) a step further. Division maps are rather limited in that only specific spectral features can be highlighted. Division maps do not allow for complex calculations, such as ratios of different areas, or using Gaussian fits of certain

peaks, or simply using the entire area of the spectrum (which is related to the amount of a certain atom type).

This code produces what are called chemical maps. The first step in using the code is to load the entire data movie along with the entire I0 movie. Just as described in Section 2.4, the images corresponding to the first few eV of the spectrum are averaged (separately for the sample movie and the I0 movie), and then each movie is normalized by its pre-edge average. The images are then normalized one-by-one. Next the image is analyzed pixel-by-pixel. For every point there is a range of pixels averaged in all directions (window size set by user) to reduce the noise level involved in selecting just one pixel. This does reduce the effective resolution of the chemical map, but the variations across the entire scale of the image are generally significant enough for the averaging to not matter. For carbon, each spectrum is also has a linear fit performed to the pre-edge. After these steps the code is designed to create a series of chemical maps. Except for chemical maps that represent the total intensity of the spectrum (a Riemann sum of all area under the curve), each map is always normalized by the total area under the spectrum. This is done to compare relative changes in certain spectral features between different parts of the image. As an example for carbon, a map could be produced that reflects the amount of C=C bonding by taking the ratio of a Gaussian fit of the peak at 285.0 eV and the area of the entire spectrum. Regions of the sample with more C=C bonds would have a larger ratio, and would be colored differently than areas with a smaller ratio. An example chemical map for the sp^2-fraction of a UNCD wear track is shown in Fig. 2.20.

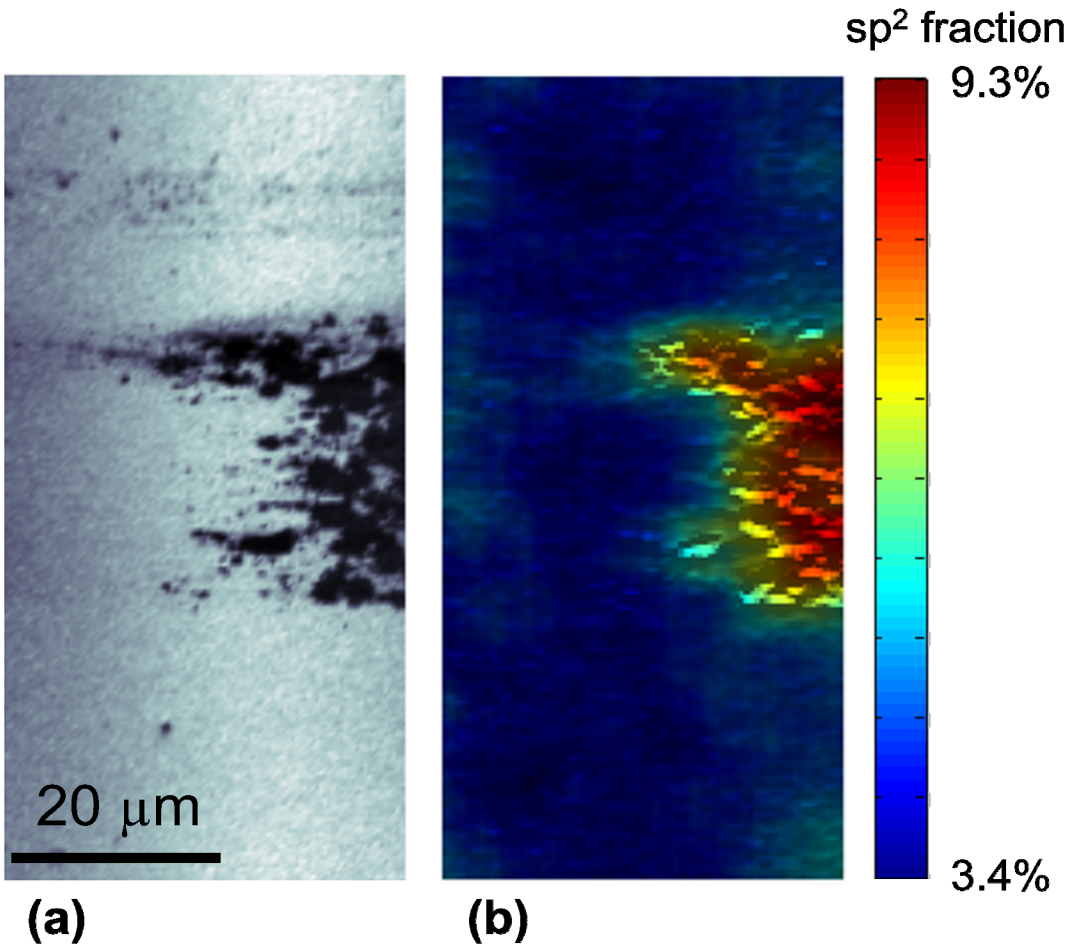

Fig. 2.20: Example of chemical map. (a) PEEM image at the carbon *K*-edge from the end of a UNCD wear track, and (b) chemical map of the sp^2-fraction showing higher sp^2-fraction inside the wear track

This can be taken a step further to correlate the chemical information with local topography in the track. A separate code was written that allows a PEEM image to be spatially aligned with a topographic image (such as that from SWLI or atomic force microscopy) from the same area of a sample. An example for SWLI from a UNCD sample is shown in Fig. 2.21(a). The user identifies four points on each image as being at identical locations. The code rotates and stretches/shrinks the topographic data to match

the orientation and scaling of the PEEM image. Then a colored 3D image is produced where the height of the data represents the physical topography of the sample, and the color map is derived from a chemical map made from the PEEM data (Fig. 2.21b). This allows the researcher to visually explore the rich array of information that PEEM and topographic images contain and to search for correlations of interest. This technique was used to a limited extent in the analysis presented in this thesis; future work would benefit from utilizing this software more extensively.

Fig. 2.21: (a) Topographic data from the end of a UNCD wear track. (b) Chemical map from Fig. 2.20b applied to the topographic data in Fig. 2.21a. The height of the image uses the same scale as in (a).

2.7 Magnetic Imaging with NEXAFS

As previously mentioned, the large negative bias in PEEM prevents measurement of non-planar surfaces. This means that the counterfaces in tribological contacts, usually spherical in shape, can not be characterized. As well, debris and roughness can be problems for obtaining a PEEM image at all. A new spatially-resolved spectroscopy tool has been designed at the NSLS and does not suffer these limitations [2.40]. Unlike PEEM, the new spectroscopic imaging technique at the NSLS can handle samples of a non-planar geometry. That makes this technique very attractive for the *ex situ* characterization of both the flat and the counterface (often a sphere) that comprise a tribological interface during testing.

The imaging NEXAFS measurements were performed using the parallel processing imaging system located at the National Synchrotron Light Source (also the NIST beamline U7A). This synchrotron-based system collects electrons in a PEY mode, with a retarding bias of 150V, while magnetically guiding the emitted electrons to form an image of the NEXAFS signal from a ~13 x 18 mm region. The technique combines near edge x-ray absorption fine structure (NEXAFS) spectroscopy and a parallel process magnetic field electron yield optics detector. The rapid parallel processing optics detector produces a series of NEXAFS images (similar to PEEM) as the x-ray energy is scanned from below to above an elemental absorption edge. The image stack reveals information about the bond chemistry at the surface with 50 μm spatial resolution. Absorption spectra are taken using a photon energy range of 270-340 eV for the carbon *K*-edge, and 520-570 eV for the oxygen *K*-edge, yielding energy resolutions of 0.1 eV and 0.2 eV, respectively.

To eliminate the effects of beam intensity fluctuations and absorption features in the beamline optics, the PEY signals are normalized by the absorption profile of a clean gold mesh located upstream from the analysis chamber.

Data are analyzed much the same way as described in Section 2.5. In this case the entire image is normalized by the same reference spectrum. The ROI selection process is identical. As this technique uses PEY, there are differences when comparing spectra to those measured in PEEM, even from the same sample. The higher surface sensitivity for PEY results in the spectra showing an increased amount of disordered sp^2 bonding. These samples are all prepared *ex situ*, and though pains are taken to keep them as clean as possible, there is still a certain small amount of well-adhered contamination at the surfaces. However, the trends are still the same, and, if anything, the increased surface sensitivity means that smaller changes to the surface chemistry are more easily detected.

Fig. 2.22 shows example data from the NSLS imaging setup. Fig. 2.22a shows a full-field image of eleven UNCD-coated Si_3N_4 spheres mounted and imaged at the same time. The image is ~10x12 mm^2, and the illumination is centered on the middle column of spheres. Fig. 2.22b shows just one sphere (middle column, second sphere from the bottom in Fig. 2.22a), and Fig. 2.22c is the extracted spectrum from the wear scar on the sphere. As mentioned, since this technique measures the PEY signal from the sample, the spectrum has a larger contribution from the surface, including any surface contamination. This shows up as a higher peak at ~285 eV, representing the C 1s$\rightarrow\pi^*$ transition for disordered carbon-carbon double bonds, as well as a significant carbon-oxygen feature at ~286.7 eV.

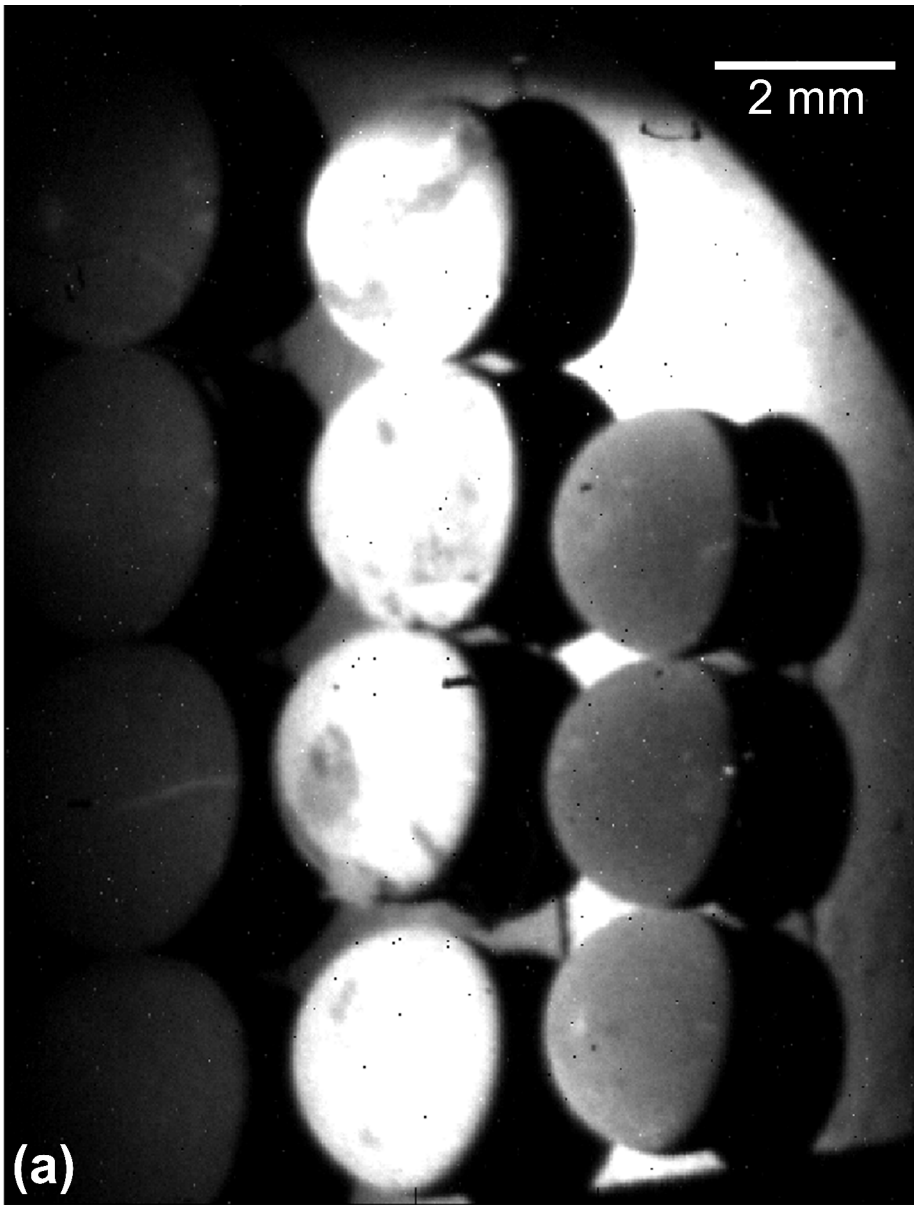
2 mm
(a)

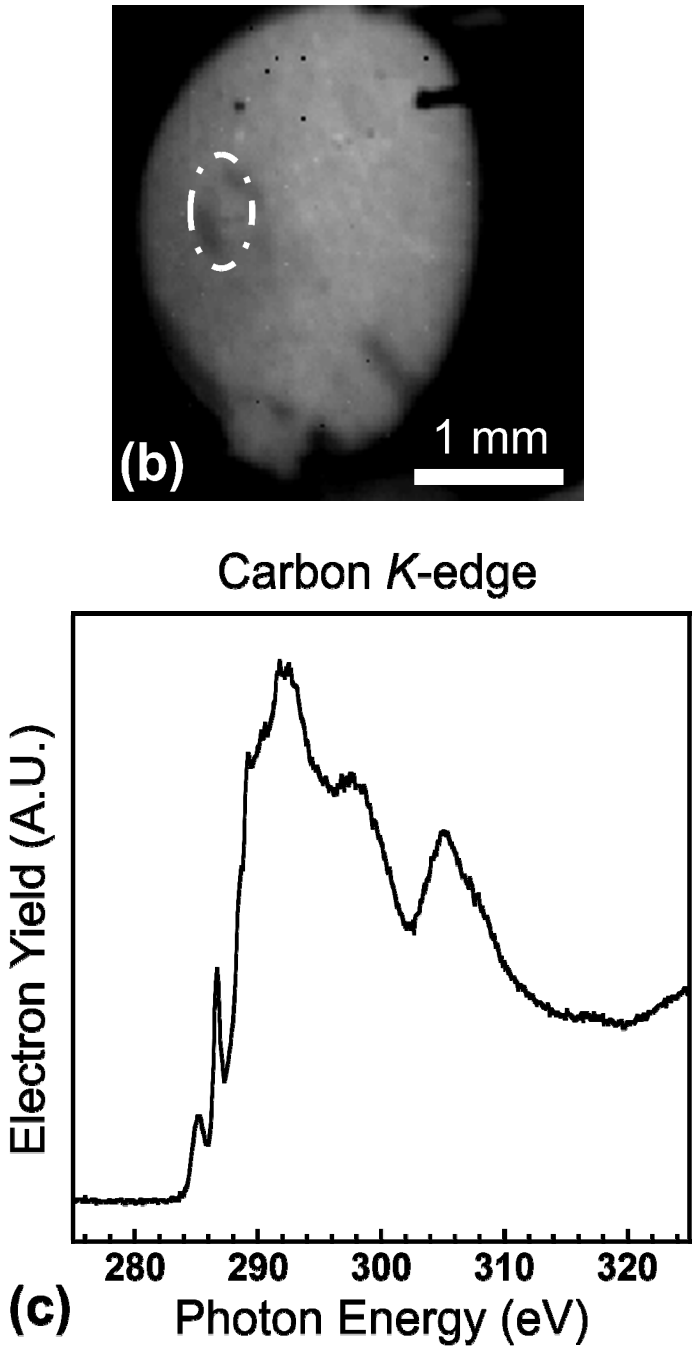

Fig. 2.22: (a) Example image of 11 UNCD-coated Si_3N_4 spheres used in tribometry tests (from averaged images between 285.6 eV and 286.5 eV), (b) single UNCD-coated Si_3N_4 sphere with ROI around wear scar, and (c) extracted carbon spectrum from ROI in (b)

2.8 Chapter 2 References

[2.1] X. Shi, D. Flynn, B. K. Tay, S. Prawer, K. W. Nugent, S. R. P. Silva, Y. Lifshitz, and W. I. Milne, Philosophical Magazine B (Physics of Condensed Matter: Statistical Mechanics, Electronic, Optical and Magnetic Properties **76**, 351 (1997).
[2.2] A. C. Ferrari, J. Robertson, M. G. Beghi, C. E. Bottani, R. Ferulano, and R. Pastorelli, Applied Physics Letters **75**, 1893 (1999).
[2.3] H. D. Espinosa, B. C. Prorok, B. Peng, K. H. Kim, N. Moldovan, O. Auciello, J. A. Carlisle, D. M. Gruen, and D. C. Mancini, Experimental Mechanics **43**, 256 (2003).
[2.4] H. J. McSkimin, and P. Andreatch, Jr., Journal of Applied Physics **43**, 3944 (1972).
[2.5] S. Cho, I. Chasiotis, T. A. Friedmann, and J. P. Sullivan, Journal of Micromechanics and Microengineering **15**, 728 (2005).
[2.6] T. A. Friedmann, J. P. Sullivan, J. A. Knapp, D. R. Tallant, D. M. Follstaedt, D. L. Medlin, and P. B. Mirkarimi, Applied Physics Letters **71**, 3820 (1997).
[2.7] Y. Lifshitz, G. D. Lempert, and E. Grossman, Physical Review Letters **72**, 2753 (1994).
[2.8] D. H. Lowndes, V. I. Merkulov, A. A. Puretzky, D. B. Geohegan, G. E. Jellison, Jr., C. M. Rouleau, and T. Thundat, (Mater. Res. Soc, Warrendale, PA, USA, 1998), pp. 325.
[2.9] N. A. Marks, D. R. McKenzie, B. A. Pailthorpe, M. Bernasconi, and M. Parrinello, Physical Review Letters **76**, 768 (1996).
[2.10] J. J. Cuomo, D. L. Pappas, J. Bruley, J. P. Doyle, and K. L. Saenger, Journal of Applied Physics **70**, 1706 (1991).
[2.11] T. M. Alam, T. A. Friedmann, P. A. Schultz, and D. Sebastiani, Physical Review B (Condensed Matter and Materials Physics) **67**, 245309 (2003).
[2.12] D. S. Grierson, A. V. Sumant, A. R. Konicek, T. A. Friedmann, J. P. Sullivan, and R. W. Carpick, Journal of Applied Physics **107** (2010).
[2.13] N. A. Marks, D. R. McKenzie, B. A. Pailthorpe, M. Bernasconi, and M. Parrinello, Physical Review Letters **76**, 768 (1996).
[2.14] A. V. Sumant, D. S. Grierson, J. E. Gerbi, J. A. Carlisle, O. Auciello, and R. W. Carpick, Physical Review B (Condensed Matter and Materials Physics) **76**, 235429 (2007).
[2.15] A. V. Sumant, O. Auciello, H. C. Yuan, Z. Ma, R. W. Carpick, and D. C. Mancini, (SPIE - The International Society for Optical Engineering, USA, 2009), p. 731817 (7 pp.).
[2.16] P. W. May, J. N. Harvey, J. A. Smith, and Y. A. Mankelevich, Journal of Applied Physics **99** (2006).
[2.17] O. Auciello *et al.*, IEEE Microwave Magazine **8**, 61 (2007).
[2.18] A. C. Rennie, P. L. Dickrell, and W. G. Sawyer, Tribology Letters **18**, 499 (2005).
[2.19] D. J. Dickrell III, and W. G. Sawyer, Tribology Letters (2010).
[2.20] J. Stöhr, *NEXAFS spectroscopy* (Springer-Verlag, Berlin; New York, 1992).

[2.21] W. E. Moddeman, T. A. Carlson, M. O. Krause, B. P. Pullen, W. E. Bull, and G. K. Schweitzer, Journal of Chemical Physics **55**, 2317 (1971).
[2.22] B. Ziaja, D. van der Spoel, A. Szoke, and J. Hajdu, Physical Review B (Condensed Matter and Materials Physics) **64**, 214104 (2001).
[2.23] B. Ziaja, D. van der Spoel, A. Szoke, and J. Hajdu, Physical Review B (Condensed Matter and Materials Physics) **64**, 214104 (2001).
[2.24] S. Fatehi, C. P. Schwartz, R. J. Saykally, and D. Prendergast, Journal of Chemical Physics **132**, 094302 (9 pp.) (2010).
[2.25] J. J. Rehr, J. Mustre de Leon, S. I. Zabinsky, and R. C. Albers, Journal of the American Chemical Society **113**, 5135 (1991).
[2.26] J. J. Rehr, J. Mustre de Leon, S. I. Zabinsky, and R. C. Albers, Journal of the American Chemical Society **113**, 5135 (1991).
[2.27] R. Gago, I. Jimenez, and J. M. Albella, (Elsevier, 2001), pp. 530.
[2.28] S. Osswald, G. Yushin, V. Mochalin, S. O. Kucheyev, and Y. Gogotsi, Journal of the American Chemical Society **128**, 11635 (2006).
[2.29] A. R. Krauss *et al.*, Diamond and Related Materials **10**, 1952 (2001).
[2.30] A. V. Sumant, P. U. P. A. Gilbert, D. S. Grierson, A. R. Konicek, M. Abrecht, J. E. Butler, T. Feygelson, S. S. Rotter, and R. W. Carpick, Diamond and Related Materials **16**, 718 (2007).
[2.31] S. Anders, H. A. Padmore, R. M. Duarte, T. Renner, T. Stammler, A. Scholl, M. R. Scheinfein, J. Stohr, L. Seve, and B. Sinkovic, Review of Scientific Instruments **70**, 3973 (1999).
[2.32] B. H. Frazer, M. Girasole, L. M. Wiese, T. Franz, and G. De Stasio, Ultramicroscopy **99**, 87 (2004).
[2.33] S. Anders, T. Stammler, W. Fong, D. B. Bogy, C. S. Bhatia, and J. Stohr, Journal of Vacuum Science & Technology A (Vacuum, Surfaces, and Films) **17**, 2731 (1999).
[2.34] S. Anders, T. Stammler, W. Fong, C.-Y. Chen, D. B. Bogy, C. S. Bhatia, and J. Stohr, Journal of Tribology **121**, 961 (1999).
[2.35] G. W. Canning, M. L. S. Fuller, G. M. Bancroft, M. Kasrai, J. N. Cutler, G. De Stasio, and B. Gilbert, Tribology Letters **6**, 159 (1999).
[2.36] A. R. Konicek, D. S. Grierson, P. U. P. A. Gilbert, W. G. Sawyer, A. V. Sumant, and R. W. Carpick, Physical Review Letters **100**, 235502 (2008).
[2.37] D. S. Grierson *et al.*, Journal of Vacuum Science and Technology B: Microelectronics and Nanometer Structures **25**, 1700 (2007).
[2.38] G. F. Rempfer, and O. H. Griffith, Ultramicroscopy **27**, 273 (1989).
[2.39] J. J. Rehr, and R. C. Albers, Reviews of Modern Physics **72**, 621 (2000).
[2.40] A. R. Konicek, C. Jaye, M. A. Hamilton, W. G. Sawyer, D. A. Fischer, and R. W. Carpick, Proceedings of the National Academy of Sciences (under preparation).

3. Environmental Dependence of Friction and Wear for ta-C and UNCD

3.1 Introduction

The work in this chapter focuses on examining the specific mechanism for the low self-mated friction of tetrahedral amorphous carbon (ta-C) and ultrananocrystalline diamond (UNCD) and how the low friction depends on the environment. As discussed in Chapter 1, it has long been known that smooth diamond surfaces can exhibit low friction ($\mu < 0.05$) and wear under a range of conditions [3.1-4]. The main hypotheses for this mechanism are based on either graphitization [3.5-7], or chemical passivation [3.8, 9] of the contacting surfaces. The graphitization hypothesis proposes that shearing and local heating during contact converts the surface carbon bonds from a mostly sp^3 configuration to an ordered sp^2-bonded species. The term graphitization commonly, and incorrectly, is used to indicate both the formation of ordered graphitic material, as well as the rehybridization of sp^3-bonded carbon into amorphous sp^2-bonded carbon. The latter definition is a misnomer, and should be strictly referred to as amorphization or amorphous rehybridization to distinguish it from a process whereby sp^3-hybridized carbon is converted into ordered, planar graphite sheets. Graphite is the thermodynamically stable form of carbon at room temperature and pressure, and is a

popular solid lubricant by itself, exhibiting friction coefficients of 0.18 [3.10] and 0.15 [3.1], or used in solid lubricant composite films [3.11]. The low friction is assumed to arise from easy slip between the lamellae of graphite, which are only weakly bonded together by van der Waals' forces [3.12]. An interface that starts out with a primarily diamond character could develop to have lower friction and wear by rehybridizing into ordered graphite sheets. Graphite exhibits higher friction and wear in dry or vacuum conditions [3.13], as do diamond and ta-C. Therefore, the formation of a graphitic surface phase could consistently account for the humidity dependence of friction for diamond and ta-C.

The passivation hypothesis assumes that dangling carbon bonds formed by wear processes during sliding contact are quickly terminated to passive, stable chemical states by surface-reactive species in the environment (*e.g.* hydrogen, water, oxygen) [3.1]. For example, hydrogen-terminated diamond surfaces are highly stable and non-reactive. Friction increases if there is an insufficient flux to the surface of available species, such as in vacuum or dry conditions, and consequently dangling bonds are formed more rapidly than they are passivated. In this case, the dangling bonds can bond with other unsaturated bonds on the counterface causing high friction and high wear [3.8, 14-16]. However, surfaces that reach a steady-state where dangling bonds are sufficiently passivated between sliding passes will maintain low friction and wear.

While both of these hypotheses have been proposed (some as far back as the 1950's) neither has been definitively resolved for diamond or amorphous carbon surfaces.

Spectroscopic evidence would indicate whether one or both mechanisms is responsible for the low friction. In the case of graphitization, there would be the measurable shift in the C 1s→π* peak location. Passivation by dissociated water species would also show up as oxygen and hydrogen bonding.

In this set of experiments, self-mated ta-C and UNCD interfaces were tested at both high and low applied loads at different levels of relative humidity (RH). The goal is to determine how friction and wear change either by varying the humidity, or by sliding under different normal pressures for these materials, and then to study the chemical nature of the worn surfaces to test the two hypotheses. Spatially resolved chemical analysis using PEEM will allow us to determine, for the first time, if graphite is present in the worn interface, or if signatures of chemical passivation are present. If graphitization occurs, we expect that higher normal pressures, which cause higher shear stresses, should increase the conversion rate of sp^3- to sp^2-bonded carbon while dissipating more energy in the contact. It is also possible that higher normal stresses would impede the diffusion of passivating species to areas of the wear track with dangling bonds, causing more wear and producing more dangling bonds. This would keep the system in a high friction and high wear state.

3.2 Experimental Details

Si flats (1x1 cm^2) and Si_3N_4 spheres (Cerbec, 3 mm diam., grade 3) were simultaneously coated with either ta-C or UNCD (described in Chapter 2). After deposition on the flats and spheres, these films were used for self-mated reciprocating

tribometry tests (described in Chapter 2). Two studies were performed for each type of film. For the first study, henceforth referred to as the constant load study, the applied load was fixed (1.0 N for UNCD and 0.5 N for ta-C), and RH was varied (1.0%, 2.5%, 5.0%, and 50.0%). For the second study, henceforth referred to as the load/RH study, the load was varied (either 1.0 N or 0.1 N for UNCD, corresponding to 649 MPa and 300 MPa initial mean Hertzian pressures, respectively, and 0.5 or 0.05 N for ta-C, corresponding to 517 MPa and 240 MPa initial mean Hertzian pressures, respectively), and the RH was set at either 50.0% or 1.0%. As a reference, at 1.0% RH and ambient temperature, the impingement rate of water molecules to the surface is 9.6×10^{17} $cm^{-2}s^{-1}$. For a bare, unreconstructed diamond (111) surface, assuming that every H_2O dissociates into OH and H with a sticking coefficient of 1, it would take 2.5×10^{-5} seconds for the surface to be fully passivated (neglecting the time required for species to diffuse and find an available site for adsorption). In all, six tracks were made per sample: four tracks at a fixed load (1.0 N for UNCD and 0.5 N for ta-C) with RH varying between 1.0-50.0%, and two tracks at either 1.0% or 50.0% RH, but with one tenth the applied load. Each track was made using an unworn sphere; thus, six different spheres were used to create the six tracks on each sample.

For the load/RH study, it was desirable to cover an order of magnitude change in load. The highest applied load (0.5 N) for the ta-C tests was chosen to prevent sticking of the sphere to the surface that was found to occur at higher applied loads. UNCD films were able to sustain a higher initial load (1.0 N) without sticking. In all cases, the number

of sliding cycles (5,000) was chosen to ensure steady-state friction behavior (stable friction not changing over time). The reciprocation length was set to 600 μm for every track with a reciprocation rate of 2.5 Hz. However, the tracks created with higher loads and lower humidities were shorter (only ~420-560 μm) as the higher static friction prevented longer traversal distances. It is unclear from the profilometry if this distance evolved with the number of sliding cycles. Single point wear volumes and wear rates of the spheres and flats were determined from optical profilometry measurements (Zygo NewView 6300). The wear tracks were analyzed *ex-situ* using PEEM.

3.3 Results and Discussion

3.3.1 Constant-Load Studies

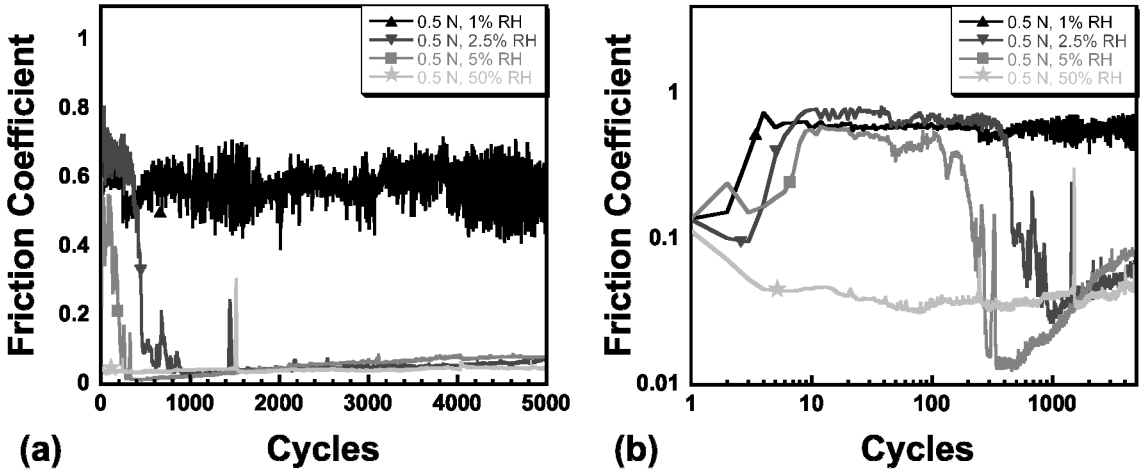

Fig. 3.1: (a) ta-C constant-load study friction plot. (b) Log-log plot of the data in (a) to highlight run-in and friction.

The friction data from the constant-load study for ta-C are plotted in Fig. 3.1. The test performed at 1.0% RH exhibits a high, fluctuating friction coefficient (~0.6) for all

5000 cycles. All other data have a period of higher friction (run-in) before eventually achieving a friction coefficient of ~0.04. Fig. 3.1b highlights the difference in the run-in behavior of the track created at 50.0% RH compared to the others. The run-in for the 50.0% RH track has a sharp drop in friction in 4 cycles and then fully runs in in less than 40 cycles, while the run-in requires 340 cycles for 5% RH, and 920 cycles for 2.5% RH. In other words, for each test that achieved low friction there is an inverse relationship between RH level and number of run-in cycles. As well, the steady-state friction coefficients slowly increase at higher sliding cycles. Note that an anomalously low friction coefficient is seen in the first 1-3 cycles for the high friction tracks. This transient effect is believed to be due to either the initial presence of contamination or sticking of the slider during the first few small-amplitude cycles.

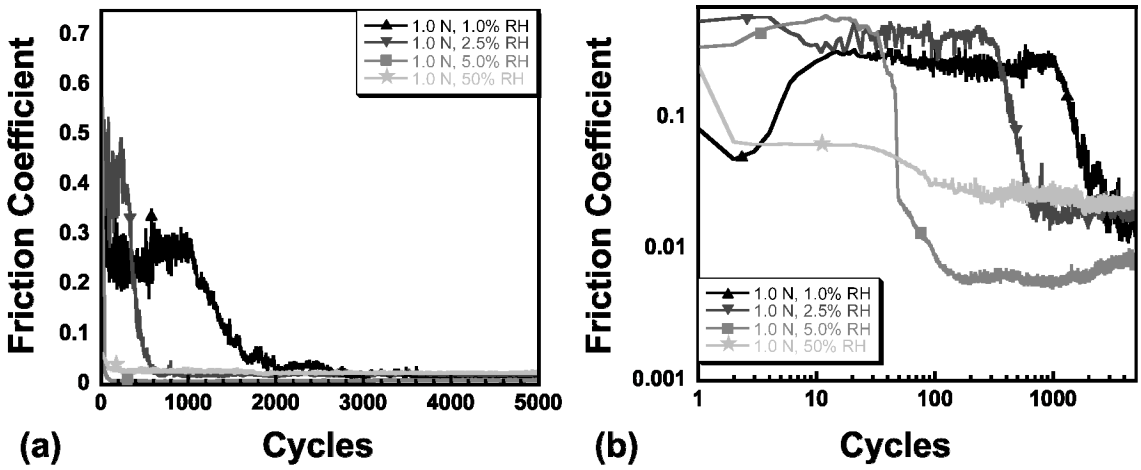

Fig. 3.2: (a) UNCD constant-load study friction plot. (b) Log-log plot of the data in (a) to highlight run-in and friction.

Fig. 3.2 is a plot of the friction data from the constant-load UNCD tests, and Fig. 3.2b is a zoom of the first 200 cycles. All UNCD friction coefficients eventually run in to approximately the same low friction value of ~0.02. Similar to the ta-C results shown in Fig. 3.1a, there exists a clear relationship between RH level and number of run-in cycles for UNCD. In contrast to ta-C, the UNCD friction coefficients do not show an increase as the number of sliding cycles increases.

The results from the constant load studies for ta-C and UNCD (Fig. 3.1 and Fig. 3.2) show that there is a trend of decreasing number of run-in cycles with increasing RH. With successively lower amounts of passivating species in the environment (lower RH), more sliding cycles are needed for the interface to reach a steady state low friction value, with the exception of the 0.5 N, 1.0% RH ta-C track which never runs in to low friction. Previous polycrystalline diamond run-in studies mentioned above involved modification of the surface structure and chemistry by polishing prior to testing [3.17] or changing the film growth conditions [3.11]. These results show that ta-C and UNCD run-in behavior for self-mated interfaces can be controlled by just varying humidity in the environment during sliding. This demonstrates there is a strong tribochemical component to the run-in of these hard-carbon interfaces. These results either support the hypothesis that the passivation of dangling carbon bonds during sliding by water vapor is required to achieve low friction and wear, or they suggest that the formation of a graphitic layer is inhibited by the absence of water vapor.

3.3.2 Load/RH Studies

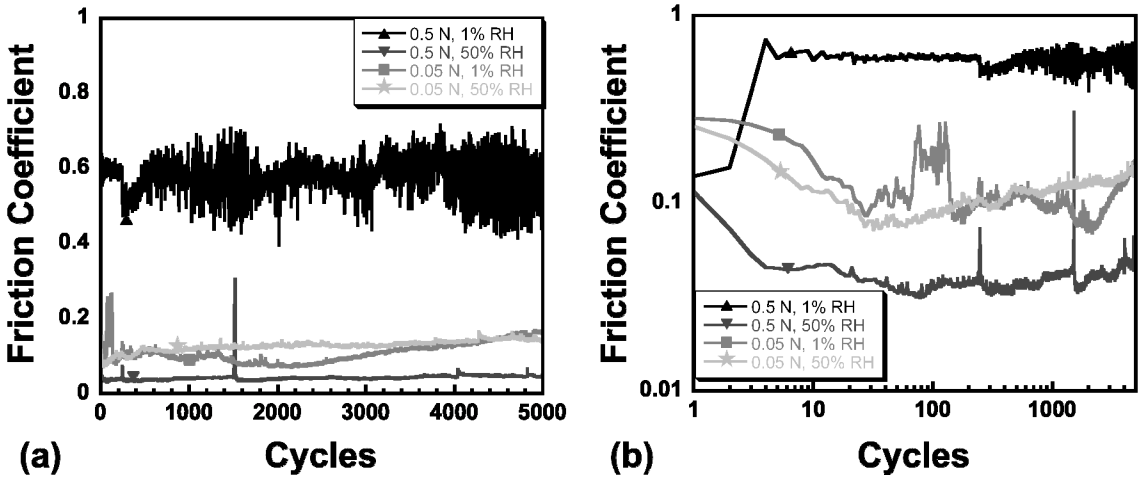

Fig. 3.3: (a) ta-C load/RH study friction plot, (b) Log-log plot of the data in (a) to highlight run-in and friction.

The ta-C friction data from the load/RH study are shown in Fig. 3.3a and Fig. 3.3b. As already seen in Fig. 3.1a, the track created at 0.5 N, 1.0% RH never achieves low friction. However, the track created at 0.05 N, 1.0% RH does run in to a minimum friction value of 0.069 (like the other ta-C tracks, this slowly increases with more cycles). Also, as already seen in Fig. 3.1a, there is a transition in behavior as a function of RH between the two 0.5 N load tracks, such that the track created at 50.0% RH runs in quickly and maintains low friction while the track at 1.0% RH never runs in. The ta-C load/RH study also reveals quantitative differences in the final friction values for the three tracks that ran in. The friction coefficient after run in for the 0.5 N load test was 0.046 (Fig. 3.3a). This is less than one-third the value of the final friction coefficients for

the 0.05 N tracks, made at 1.0% and 50.0% RH, which were 0.163 and 0.139, respectively.

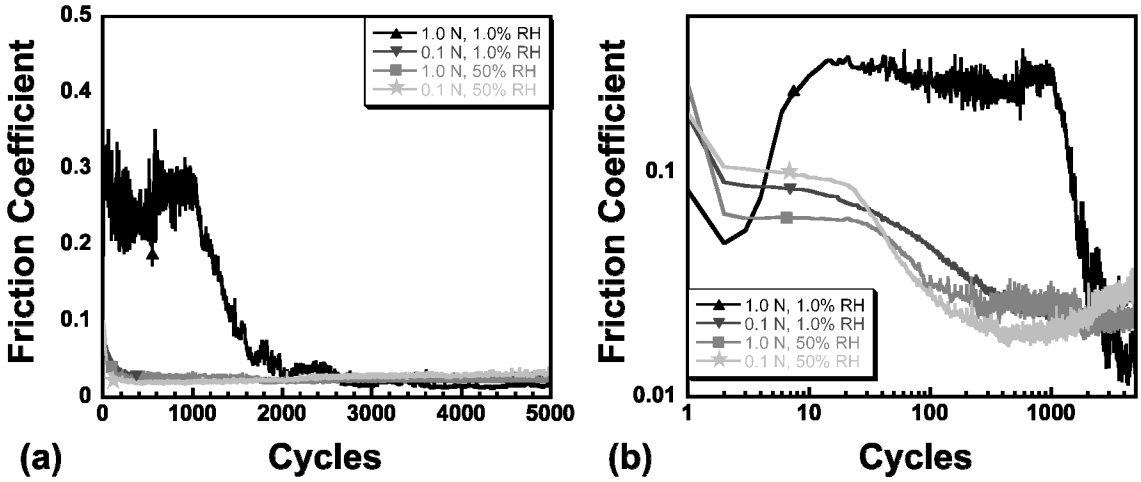

Fig. 3.4: (a) UNCD load/RH study friction plot, (b) Log-log plot of the data in (a) to highlight run-in and friction.

Fig. 3.4a and Fig. 3.4b show the equivalent load/RH study data for UNCD. For these UNCD tests, the tribometry results show that all four tracks created (at high and low load, high and low humidity) ran in to a low friction value. It followed the same overall trend seen for ta-C: the track created at lower humidity and higher load exhibited higher friction and higher wear initially, but the 1.0 N, 1.0% RH UNCD track eventually does run in. Also similar to ta-C, the tracks made at higher load ran in to slightly lower friction values (0.015 and 0.021) compared to the tracks made at the lower load (0.028 and 0.029).

3.3.3 Load/RH Study PEEM Results

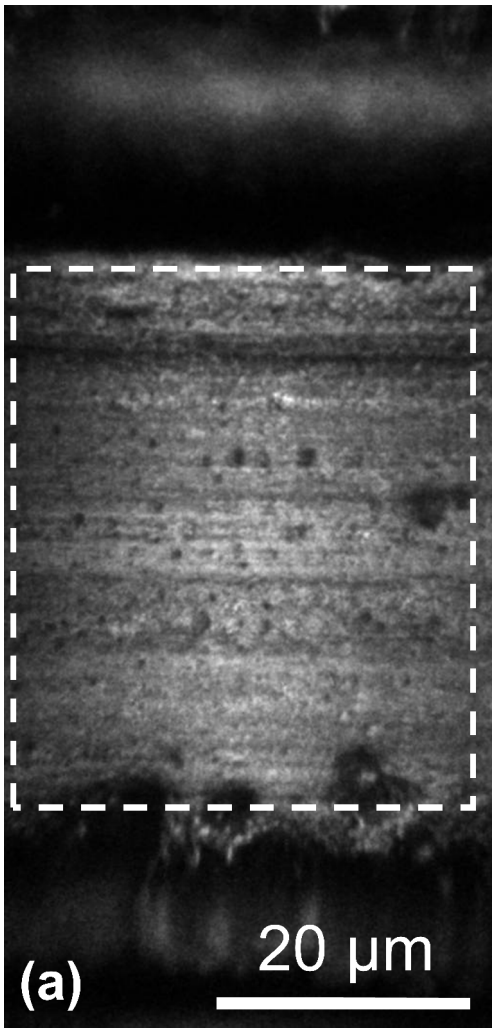

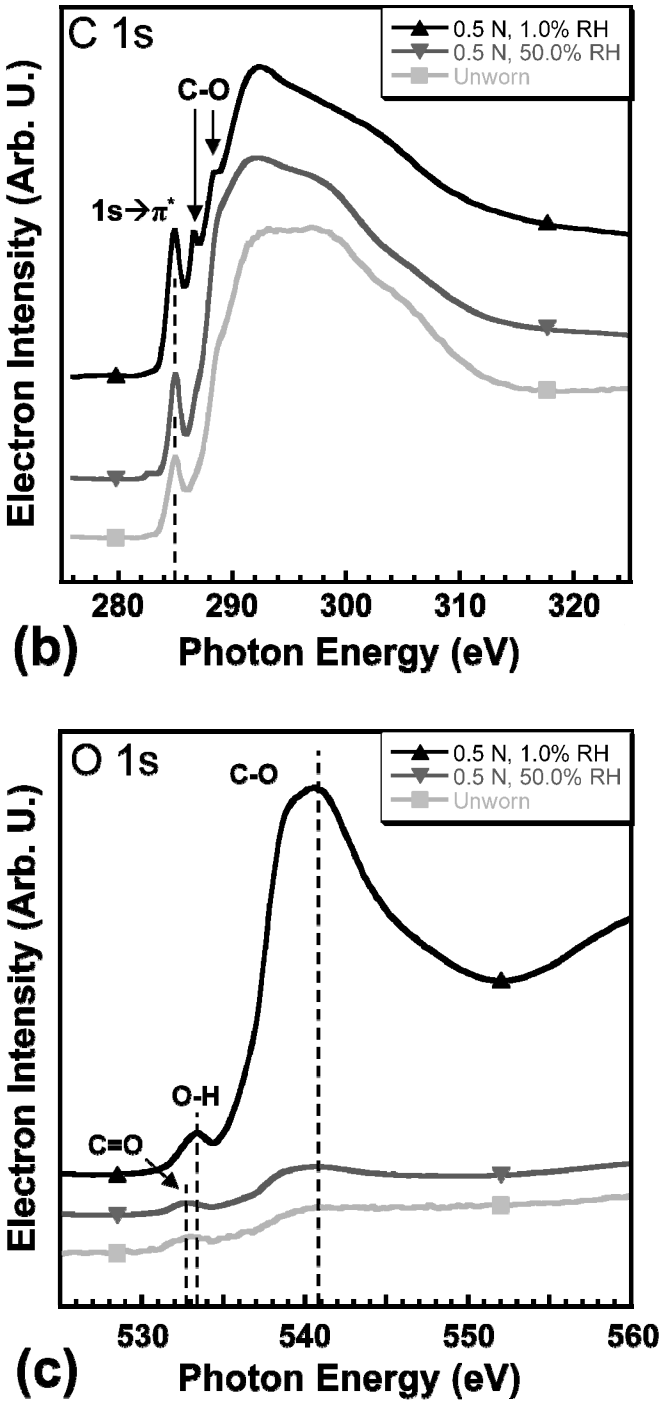

Fig. 3.5: (a) ta-C PEEM image taken with 289.0 eV photons on heavily worn (0.5 N, 1.0% RH) wear track, (b) Carbon *K*-edge spectra from heavily worn, lightly worn,

and unworn parts of the ta-C sample (heavily worn ROI shown in image), (c) Corresponding oxygen *K*-edge data (same ROIs as in (b)).

Analysis of the *ex-situ* PEEM data allows us to explore the tribochemical reactions that occurred under the different testing conditions. Fig. 3.5a is a PEEM image taken at 289.0 eV from the 0.5 N, 1.0% RH ta-C track. The image shown has a large region of interest (ROI) indicated within the wear track borders. The bottom spectrum shown in Fig. 3.5b is a reference taken on an unworn portion of the ta-C sample, and the top spectrum is from the worn region in Fig. 3.5a. There are two main spectroscopic differences between the heavily-worn and unworn spectra. The first is the increase in the C 1s→π* peak at 285.0 eV for the 1.0% RH track. The second is the significant amount of oxidation in the 1.0% RH wear track, as evidenced by the peaks in the heavily worn C *K*-edge spectrum at 286.7 eV and 288.6 eV, which are assigned to a C-O Rydberg orbital and C-O σ* antibonding orbital, respectively [3.18]. A Rydberg orbital is a weakly-bound, unoccupied state of an atom or molecule very near the Fermi level. As such, it is also near the ionization potential of core level electrons, and so is located near the edge jump for NEXAFS spectra. The lightly-worn spectrum from the 0.5 N, 50.0% RH track shows some increase in the C 1s→π* peak at 285.0 eV, giving evidence of a small amount of rehybridization, and some traces of oxidation.

The oxygen *K*-edge spectra (Fig. 3.5c) also reveals differences between the three regions. The spectrum from the unworn area (bottom spectrum) and the spectrum from the 0.5 N, 50.0% RH track (middle spectrum) are similar in both shape and intensity.

There is a small peak around 532.7 eV corresponding to a O 1s→π* transition for double-bonded oxygen [3.19], and then a low, broad hump starting at 538.0 eV which is due to the σ components of single- and double-bonded oxygen. The unworn spectrum has a low overall intensity, which is expected as the surface only has a small amount of oxygen from contamination. The relative intensities of these two curves suggest that there is little oxygen in the 0.5 N, 50.0% RH track. In the case of the 1.0% RH track, there is substantially more oxygen overall as noted by the much higher intensity of the entire spectrum. The oxygen is more σ- than π -bonded, as demonstrated by the much larger edge jump at 538.0 eV and the noticeable C–O feature at ~541 eV. However, for the 1.0% track there is a shift in the pre-edge peak to 533.4 eV, which corresponds to the presence of an O-H bond [3.18].

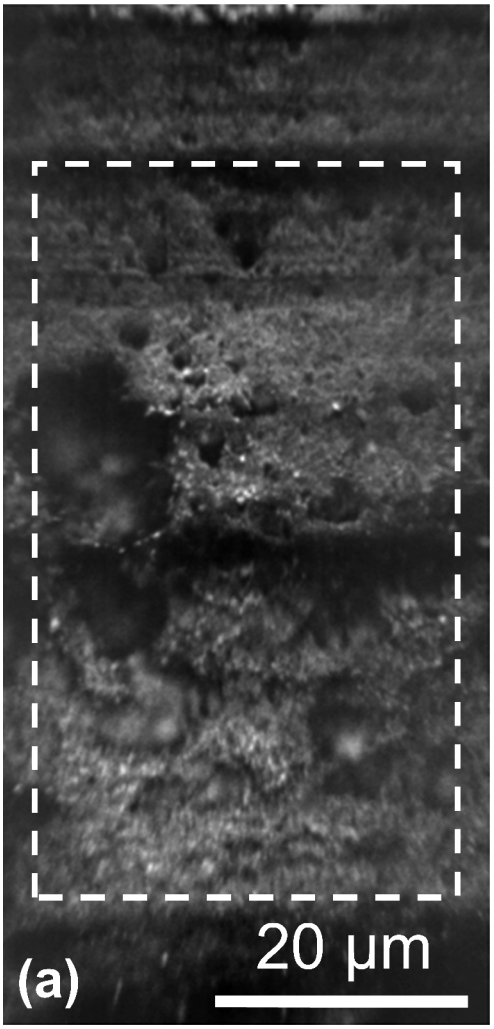
20 µm
(a)

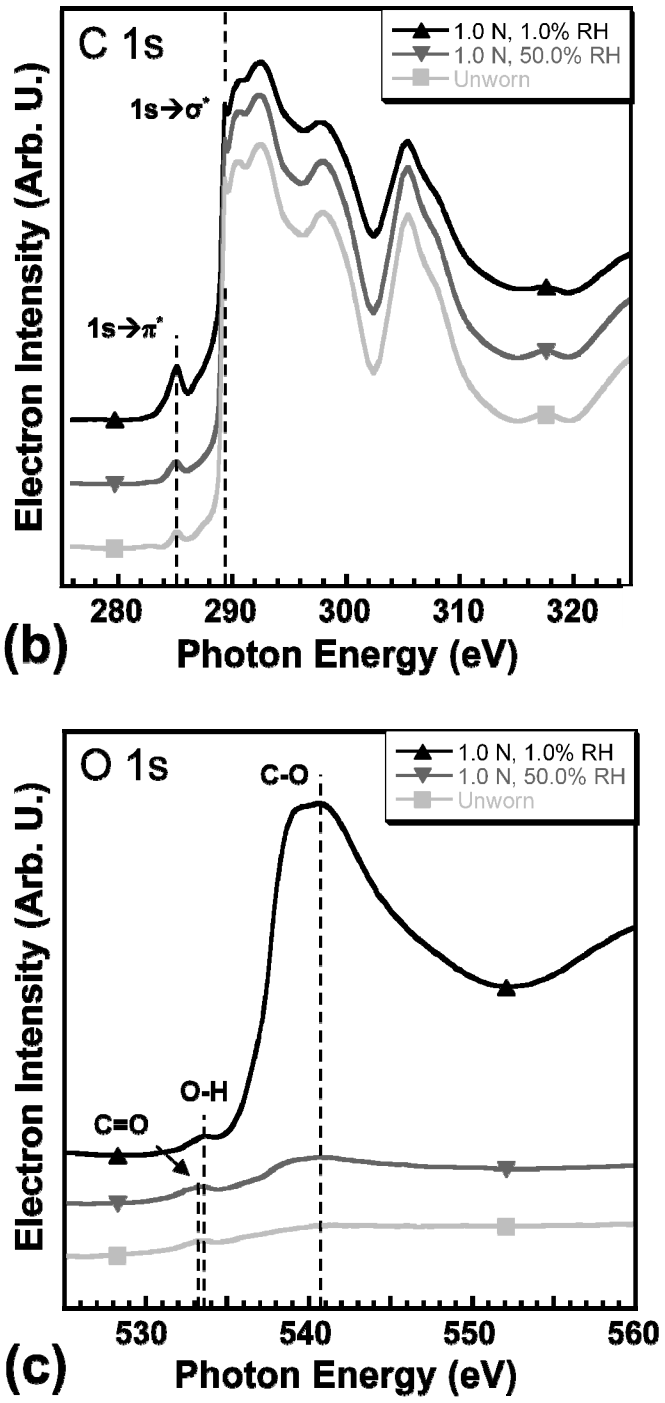

Fig. 3.6: (a) UNCD PEEM image taken with 289.0 eV photons on heavily worn (1.0 N, 1.0% RH) wear track, (b) Carbon *K*-edge spectra from heavily worn, lightly

worn, and unworn parts of the sample (heavily worn corresponds to ROI in image), (c) Corresponding oxygen *K*-edge spectra (same ROIs as in (b)).

The PEEM results from the UNCD constant-load study are similar to those from the ta-C constant-load study. Fig. 3.6a is a PEEM image taken at 289.0 eV from the UNCD track created at 1.0 N, 1.0% RH. This image is entirely inside the borders of the wear track. The bottom spectrum in Fig. 3.6b is from an unworn portion of the same UNCD sample. The top spectrum in Fig. 3.6b is from the ROI in Fig. 3.6a. The spectrum from the 1.0 N, 1.0% RH track shows evidence of both $sp^3 \rightarrow sp^2$ rehybridization of the carbon bonds (increase in peak height at 285.0 eV) as well as oxidation (features at ~286.4 and ~288.6 eV). The oxygen data in Fig. 3.6c show that the different UNCD spectra are very similar to the O 1s ta-C spectra. There is a weak oxygen signal from the unworn portion of the sample (bottom spectrum) and the 1.0 N, 50% RH track (middle spectrum). The small, broad pre-edge feature is centered at 533.2 eV, and is attributed to an overlap of peaks from the π-bonded oxygen as well as hydroxyl groups. The broad feature starting at 538.0 eV is from the σ-bonded oxygen. These spectra are contrasted with a significant increase in oxygen from the 1.0 N, 1.0% track (top spectrum). Here the pre-edge peak has shifted and is centered at 533.5 eV, which, like ta-C, indicates more O-H bonding. The edge jump is apparent at 538.0 eV, with a C-O feature at 541.0 eV.

These results disprove the hypothesis of graphitization. If graphitization occurs, where sp^3-bonded carbon is rehybridized into ordered, sp^2-bonded sheets, there would be a noticeable shift in the C $1s \rightarrow \pi^*$ transition from 285.0 eV to 285.5 eV [3.15, 20, 21].

However, there is no spectroscopic evidence for this shift, even in the heavily worn spectra in Fig. 3.5b and Fig. 3.6b. These spectra had the highest friction, which also means the highest amount of energy dissipated in the contact, as well as the highest amount of wear. But even these wear tracks do not show the presence of graphitic carbon. None of the spectra from any of the wear tracks display a shift in the C 1s$\rightarrow\pi^*$ peak energy, indicating there is no ordered graphite present. Spectra from graphite are similar to spectra taken on graphene surfaces [3.22], suggesting graphene is not formed either.

To further rule out the formation of graphite, we used the transmission properties of x-rays through graphite and diamond and the electron emission properties of carbon [3.23] to simulate a NEXAFS spectrum for one monolayer of graphite on top of UNCD (Fig. 3.7, solid gray line). The atomic densities of graphite and UNCD were used to determine the penetration depth of x-rays into a hypothetical sample of one monolayer of graphite on top of bulk UNCD. The known spacing between graphite planes was used as the monolayer thickness. Then, for each absorbed photon there was one Auger electron produced. By calculating the emission profile of these Auger electrons (assuming they all have ~280 eV energy, and so a 0.75 nm mean free path), the percentage electron yield as a function of depth was calculated. For this hypothetical structure, ~27% of the electrons emitted at the C *K*-edge come from the graphite monolayer. Thus, the simulated spectrum is the linear combination of 27% graphite and 73% UNCD. The sp^2 percentage of this graphite layer is a lower bound for three reasons. First, the monolayer thickness was a lower bound, using the spacing between two sheets in HOPG. A thicker layer would have

more photon absorption and therefore more electron emission, meaning a higher percentage coming from the layer. Second, we assumed the longest electron mean inelastic path (0.75 nm), meaning electrons from deeper in the bulk can contribute a higher fraction of the total signal. Last, any interlayer bonding, which would likely have sp^2 character, was ignored. All of these factors would only enhance the emission from the graphitic layer, yielding a more noticeable graphite character to the resultant spectrum. A simulated spectrum with the same sp^2 content as the most heavily modified region of the 1.0 N, 1.0% UNCD track corresponds to a coverage of only 42 ± 2% of a monolayer of graphite. Further evidence for the lack of graphitization is shown in Fig. 3.7 (bottom). The dashed gray spectrum is the subtraction of an unworn UNCD spectrum from the 1.0 N, 1.0% track spectrum. The result is similar to the spectrum from hydrogenated amorphous carbon [3.24] (Fig. 3.7, dashed black line), suggesting that some amount of amorphous carbon was created by wear.

We performed a similar calculation to that done for graphite, but instead using the hydrogenated amorphous carbon spectrum in Fig. 3.7 for the topmost layer. This analysis revealed that an amorphous carbon layer only 0.25 ± 0.01 nm thick yields the same sp^2 content found in the heavily modified region of the 1.0 N, 1.0% UNCD track. The UNCD and ta-C for the low friction and low wear tracks remains almost completely unaltered at the surface, with no graphitization or significant amorphization. We conclude that the much discussed lubrication mechanism for diamond or heavily tetrahedrally-bonded

carbon involving the formation of substantial graphitic or amorphous interfacial layers does not occur for UNCD or ta-C under a broad range of conditions [3.15].

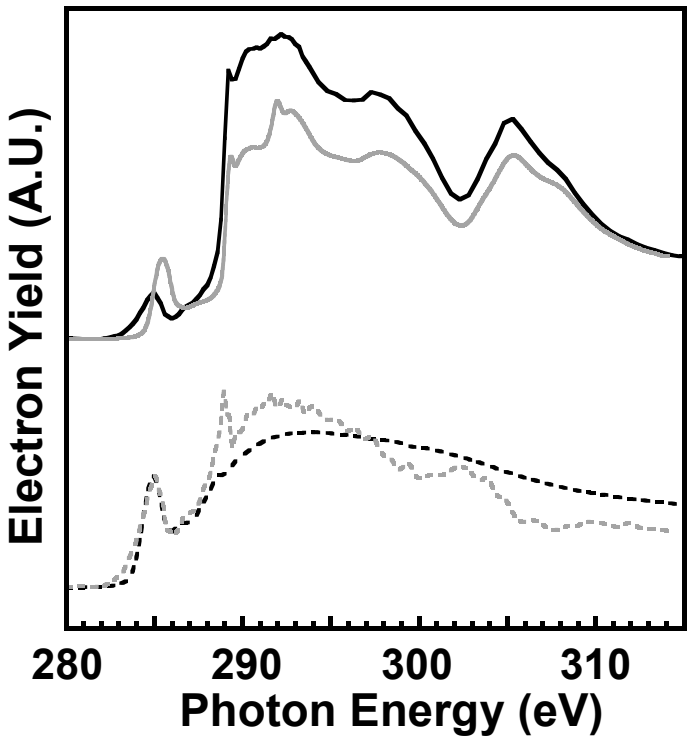

Fig. 3.7: A comparison of NEXAFS spectra. Top - experimental data from the most heavily worn region of the 1.0 N, 1.0% RH UNCD wear track (solid black line) and a simulation for one monolayer of graphite on UNCD (solid gray line). Bottom - spectrum from hydrogenated amorphous carbon (dashed black line) and subtraction of an unworn UNCD spectrum from the 1.0 N, 1.0% RH UNCD track spectrum (dashed gray line).

If passivation is the lubrication mechanism, the tribological performance should be affected by parameters that would inhibit adsorption of species on the dangling bonds formed at the contact, such as normal contact stress, sliding velocity, temperature, and both type and quantity of ambient species. The experiments here show that low friction and wear for ta-C and UNCD only occurs with sufficiently low contact pressure or with

enough RH in the environment. We can explain the run-in and subsequent friction behavior as follows. As sliding begins, if there is enough water vapor in the environment, any broken bonds that are formed during sliding are rapidly passivated, and there are few bonds broken per sliding pass. Therefore, only a small amount of wear occurs as the asperities on the relatively smooth surfaces are further smoothened, and friction runs in with few cycles. However, at higher contact pressures, more broken bonds are formed per unit time and they cannot be passivated fast enough during sliding, causing friction to remain high. Similarly, even for the same contact pressure, if the RH is reduced, the broken bonds that are formed cannot be passivated fast enough due to the lack of available species in the vapor. Again, friction and wear will remain high. This will be true until enough wear occurs that the contact pressure becomes low enough such that the bonds broken per cycle is less than or equal to the bonds passivated. In all cases there is oxidation (small amounts for tracks with low wear, and significant oxidation for cases of high wear). This agrees with previous experiments performed as a function of partial pressure of water in vacuum which supported the passivation hypothesis [3.8, 9].

The spectromicroscopy shows ta-C and UNCD tracks that experience high friction and high wear undergo chemical changes detectable in both the carbon and oxygen spectra. As sliding occurs with strong interaction of dangling bonds across the interface causing high friction, the surface of both films rehybridize (undergoing $sp^3 \rightarrow sp^2$ conversion) modestly. This is seen in the NEXAFS spectra as an increase in the C $1s \rightarrow \pi^*$ feature at 285.0 eV (Fig. 3.5b and Fig. 3.6b). Oxygen NEXAFS data from the PEEM

measurements (Fig. 3.5c and Fig. 3.6c) suggest that there is a single oxidation mechanism that occurs during wear, with primarily hydroxyl groups on the surface forming C–OH bonds. For the case of the 0.5 N, 1.0% RH ta-C track that never ran in, this could either indicate that the surface was unable to be sufficiently passivated and therefore exhibited high friction, or the surface remained reactive throughout the test and the oxidation observed with PEEM occurred after testing was complete. In contrast, the 1.0 N, 1.0% RH UNCD track did run in after 2660 cycles and exhibited this predominantly C-OH bonded surface. This suggests that the surface was driven toward a state with increased C-OH bonding during sliding which minimized the interaction between the pin and flat.

The formation of C-OH bonds is consistent with experiments [3.25, 26] and *ab initio* density functional theory (DFT) calculations [3.27, 28]. Qi *et al.* showed that hydrogen and water will preferentially dissociate (hydrogen into two H, Fig. 3.8a, and water into an H and OH, Fig. 3.8b) and bond to an unterminated diamond (111) surface [3.27]. Hydrogen has no energy barrier to form this reaction, so the dissociation and bonding will happen spontaneously. Water has a small energy barrier (0.122 eV) and, while less likely to happen than for hydrogen, will also likely occur. Okamoto estimated a higher barrier of 1.12 eV using hybrid molecular orbital-DFT calculations [3.28]. It is likely that the stresses and thermal gradients that occur during sliding could enhance this passivation mechanism. While this calculation was for single crystal diamond, there is a similarity to the highly sp^3-bonded ta-C and UNCD surfaces. UNCD would be closer to single crystal diamond, as the grains consist entirely of diamond bonded carbon.

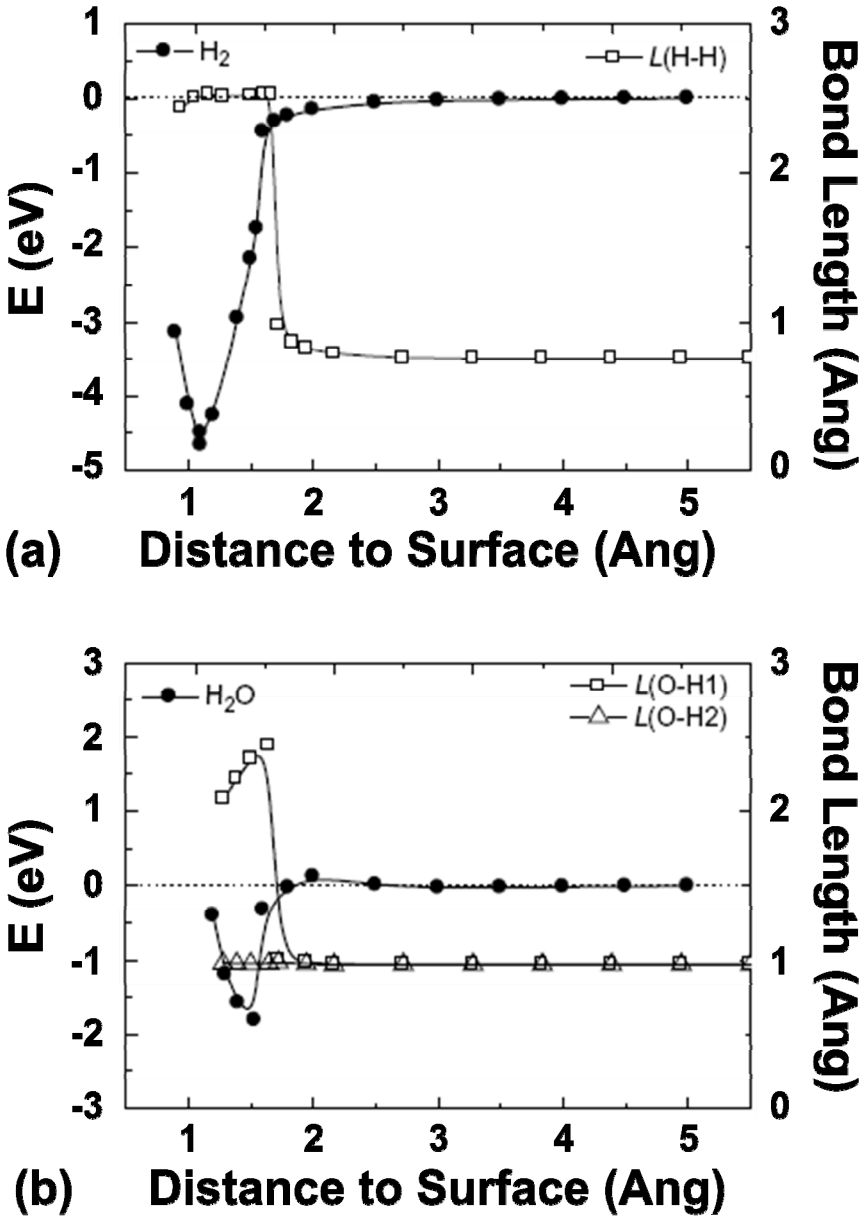

Fig. 3.8: Change in energy and bond length of hydrogen (a) and water (b) molecules as a function of normal separation distance from an unterminated diamond (111) surface [3.27].

Other recent DFT work was performed by Zilibotti *et al.* [3.29], studying the kinetic barriers and equilibrium energies of a diamond (001) surface passivated with various species, including OH groups (Fig. 3.9). For self-mated diamond interfaces terminated with the groups, they determined the potential energy surface (PES), which is the interaction energy of the interface as a function of lateral position. These PES calculations alone cannot predict tribological behavior when there are normal stresses, shear stresses, sliding motion, and more complex surface compositions. However, they do support the argument that hydroxylated diamond surfaces will reduce interactions across an interface, a hydroxylated surface separating by a calculated 0.25 nm, thereby reducing friction and wear. It should be noted that the termination that provided the lowest PES corrugation (smallest variations of the PES along any direction) was the oxygen-terminated surface (Fig. 3.9d), which formed ester groups along the carbon dimers (dimers are reorganizations of surface atoms from their bulk crystalline locations which reduce energy by forming double bonds in the plane of the surface). This would suggest that a diamond surface that could achieve this termination would have the lowest friction, and, in an environment with fewer passivating species available, this would be crucial since lower friction would mean fewer bonds broken per sliding pass, leading to fewer dangling bonds needing passivation. However, the ester terminated surface is a theoretical construct made from an environment that is saturated with O_2 molecules along with water, and the experiments show that for environments similar to the work in this thesis, the ester termination is not observable.

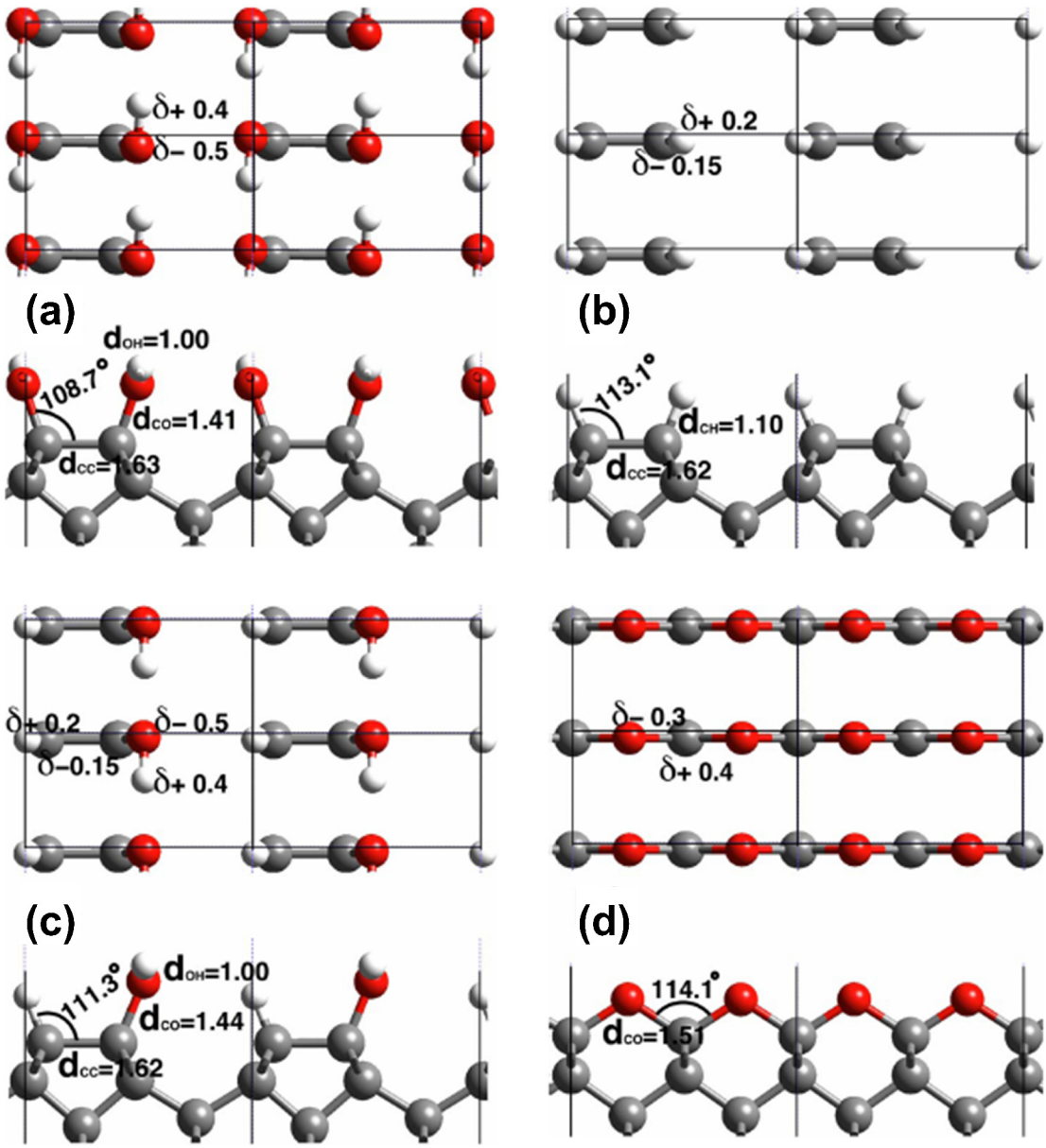

Fig. 3.9: Top and lateral view of hydroxylated (a), hydrogenated (b), H_2O-terminated (c), and oxygenated (d) diamond surfaces [3.29]. Gray atoms are carbon, red are oxygen, and white are hydrogen. Charge separation values, δ, are given for end groups, and bond angles are shown.

Furthermore, starting with an unpassivated diamond surface and molecular water vapor, achieving that C-O-C-terminated surface is a more complex process than the formation of the hydroxylated (or hydroxylated and hydrogenated) surface. Breaking one of the OH bonds in water and then passivating two carbon atoms with the resultant H and OH was calculated to be have an adsorption energy of 1.8 eV/molecule (173 kJ/mol) [3.27]. Taking that process further by breaking the OH bond from the hydroxyl group and then forming a second CO bond requires two additional steps, and is energetically unfavorable to first order when considering bond formation enthalpy (O-H is ~460 kJ/mol, C-O is ~350 kJ/mol). Within a dynamic tribological interface exhibiting high local stresses, the process leading to C-O-C bonding formation cannot be ruled out. However, the simpler process of hydroxylation is naturally expected to predominate. It was also shown by Skokov *et al.* [3.30] and Sque *et al.* [3.31] using DFT that the hydroxylated surface was more energetically favored over the solely oxidized surface.

In the case of high friction and wear conditions for both UNCD and ta-C, the O *K*-edge NEXAFS spectra consistently indicate the presence of hydroxyl groups on the surface as discussed in the context of Fig. 3.5c and Fig. 3.6c. Furthermore, the polarization of the synchrotron radiation is parallel to the plane of the sample surface. The DFT work showed that the C-O component of the hydroxyl bond (Fig. 3.9a) is oriented nearly normal to the surface, and the O-H component is oriented more normal to the plane of the carbon atoms. This would mean there would be weak coupling between the photon polarization direction and the orbital direction for the C-O bond, and stronger

coupling with the O-H bond. However, this is an ideal system with a perfectly flat surface. The tilt of the O-H bond is due to the electronic attraction of the more positively charged hydrogen atoms to the negatively charged oxygen atom on the neighboring carbon dimer. There is also a tilt due to the two sets of lone pair electrons in the unbounded orbitals. The angle of the O-H bond will be further complicated by defects and roughness of the film surface. The carbon and oxygen *K*-edge NEXAFS data in this study all show modest sigma features related to the C-O and O-H bonding expected for hydroxyl groups (~286.5 eV and 288.6 eV for carbon, ~533.5 eV for oxygen). This would make sense because of the interaction strength of the polarized synchrotron radiation with the C-O and O-H bonds of a hydroxyl group bonded to the UNCD or ta-C surface. Therefore, we conclude that it is hydroxyl groups which are the main form of oxygen bonded to the carbon surface, and responsible for the passivation of dangling bonds.

If there was a significant amount of C=O bonding, with the bond direction still oriented normal to the surface, the photon polarization would interact strongly with the π orbitals and there should be intense peaks in the spectra, especially in the O *K*-edge spectrum at ~532 eV. The large intensity of the σ features in the O *K*-edge spectra must come from some type of C-O bonding, which is determined to be from hydroxyl groups.

ta-C	μ_{ss}	Run-in cycles	Track width [µm]	Average track depth [nm]	Track wear rate [$mm^3N^{-1}m^{-1}$]	Sphere wear rate [$mm^3N^{-1}m^{-1}$]
0.5 N, 1.0% RH	0.59	N/A	156	694	$<<2.5x10^{-5}$	$5.5x10^{-6}$
0.5 N, 2.5% RH	0.075	920	88	43	$8.3x10^{-7}$	$7.3x10^{-7}$
0.5 N, 5.0% RH	0.078	340	58	9	$1.4x10^{-7}$	$1.3x10^{-7}$
0.5 N, 50.0% RH	0.046	< 40	45	4	$5.2x10^{-8}$	$5.1x10^{-8}$
0.05 N, 1.0% RH	0.163	150	34	5	$3.9x10^{-7}$	$1.5x10^{-8}$
0.05 N, 50.0% RH	0.139	< 50	32	3	$2.6x10^{-7}$	$2.1x10^{-7}$
UNCD	μ_{ss}	**Run-in cycles**	**Track width [µm]**	**Average track depth [nm]**	**Track wear rate [$mm^3N^{-1}m^{-1}$]**	**Sphere wear rate [$mm^3N^{-1}m^{-1}$]**
1.0 N, 1.0% RH	0.015	2660	211	1814	$<<3.5x10^{-5}$	$1.7x10^{-5}$
1.0 N, 2.5% RH	0.018	660	170	996	$<<1.6x10^{-5}$	$9.7x10^{-8}$
1.0 N, 5.0% RH	0.008	50	58	9	$3.4x10^{-8}$	$5.5x10^{-8}$
1.0 N, 50.0% RH	0.021	< 10	40	7	$3.7x10^{-8}$	$2.6x10^{-8}$
0.1 N, 1.0% RH	0.028	500	18	4	$8.9x10^{-8}$	$3.9x10^{-8}$
0.1 N, 50.0% RH	0.029	250	15	6	$9.3x10^{-8}$	$5.0x10^{-8}$

Table 3.1: Steady-state friction coefficient, number of run-in cycles, track width, average depth, track and sphere wear rates for ta-C and UNCD.

3.3.4 Wear Rates for High Friction Tracks

We observe that the friction and wear are correlated, consistent with the notion that unpassivated bonds lead to stronger interaction across the interface, giving high friction and much damage at the interface. The profilometry results (Table 3.1) provide

the wear track dimensions from the flats and spheres, and were used to calculate wear rates. For all studies on both ta-C and UNCD there are clear relationships between the load and RH level during the test and the number of run-in cycles, track width, average track depth, track wear rate, and sphere wear rate. Tracks that had high friction over a longer number of cycles had deeper and wider wear tracks, and therefore higher wear rates. These corresponded to higher sphere wear. For example, for ta-C, the 0.5 N, 50.0% RH track took less than 40 cycles to run in, had a final width of only 45 μm, and had a single point wear rate of 5.2×10^{-8} $mm^3N^{-1}m^{-1}$. In contrast, the 0.5 N, 2.5% RH track took 920 cycles to run in, had a final width of 88 μm, and had a single point wear rate of 8.3×10^{-7} $mm^3N^{-1}m^{-1}$. For the case of the low friction and low wear tracks, the measured wear volumes are below the uncertainty level calculated in Chapter 2. In these cases the reflected intensity data had to be used to locate the wear track, since the scar was not visible using the topographic data.

The tracks with the most severe conditions, the 0.5 N, 1.0% RH ta-C track and the 1.0 N, 1.0% and 1.0 N, 2.5% UNCD tracks, exhibited severe plastic deformation of the substrate. This makes determination of the wear rate of the film itself impossible and so in Table 3.1 we report the upper limits based on the worn volume observed in interferometry. These films are thin (1-2 μm), and they have a much higher yield strength compared to the underlying Si substrates. A TEM cross section for the 1.0 N, 1.0% RH UNCD track (Fig. 3.10) revealed that, even though the track was 4 μm deep and the Si substrate had undergone an amorphous phase change (Fig. 3.11), there was still a carbon

film on top of the amorphous Si inside the track. The NEXAFS spectroscopy confirmed the presence of carbon coatings within all wear tracks.

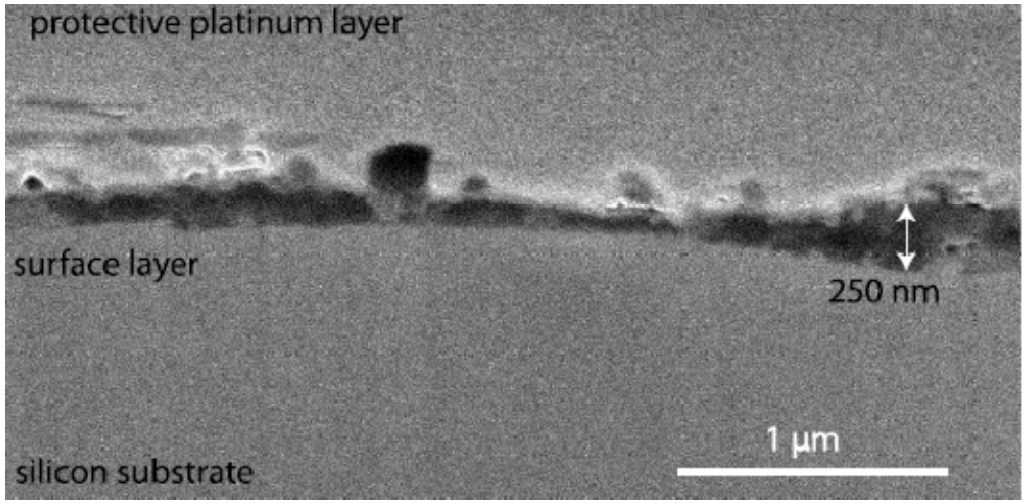

Fig. 3.10: TEM cross-section of a FIB cutout from the 1.0 N, 1.0% RH track showing presence of carbon film (dark layer).

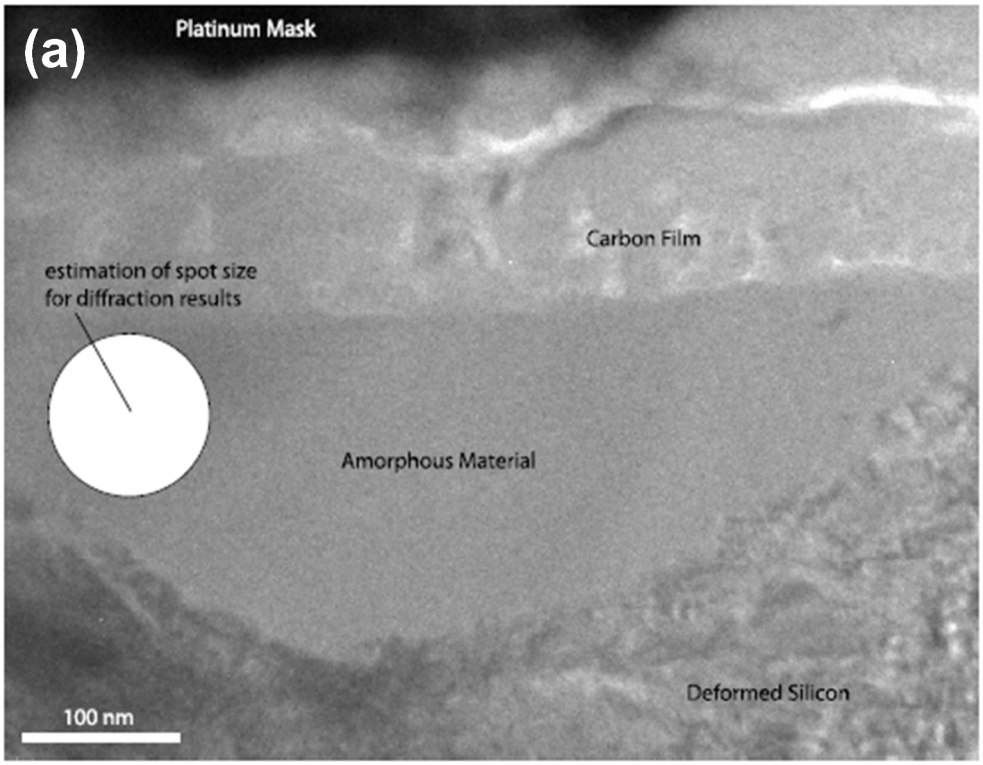

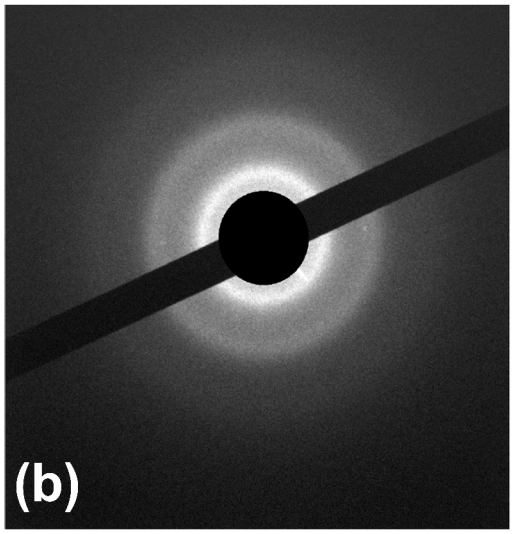

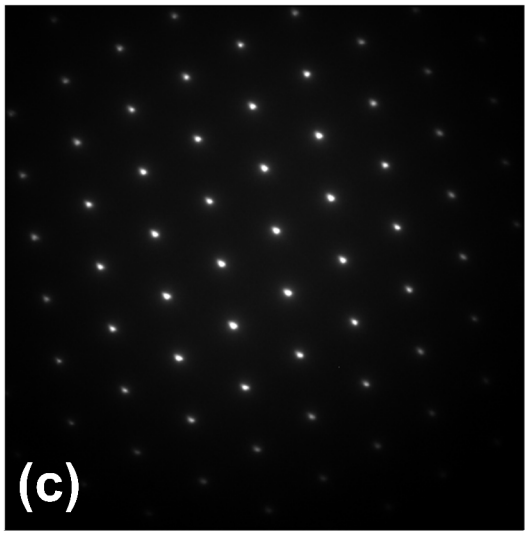

Fig. 3.11: (a) Zoomed in TEM cross-section of a FIB cutout from the 1.0 N, 1.0% RH track showing presence of carbon film with amorphous material below, most likely amorphous silicon. (b) Diffraction pattern showing no ordered structure from

amorphous material region indicated in (a). (c) Diffraction pattern of silicon just below the amorphous material region. Images courtesy of Dr. Jerry Bourne and Dr. Matt Hamilton.

3.3.5 Contact Pressure and Relative Humidity Level

Here we discuss the effect that the normal contact pressure of the contact combined with the RH level has on the friction and run-in behavior. In these experiments, for a given material and a given load, the initial contact pressure is a fixed value. As sliding begins, in different RH environments there will be similar sliding performance for the first few cycles (highlighted, for ta-C, in Fig. 3.2b). Then each system will evolve differently depending on whether or not the bonds that are broken during sliding are able to be passivated sufficiently quickly by the passivating vapor species. Tracks created at 50.0% RH for both ta-C and UNCD run in immediately and never experience many cycles of high friction (Fig. 3.1a and Fig. 3.2a). Profilometry on these tracks show there is low wear and a smaller track width, meaning a lower apparent contact area and therefore a higher average contact pressure. For the 1.0 N UNCD studies the initial mean contact pressure (assuming a Hertzian model with a Si_3N_4 sphere, radius 1.5 mm, 250 GPa modulus, and 0.24 Poisson ratio contacting a Si flat, 160 GPa modulus, and 0.245 Poisson ratio) is 649 MPa. The contact diameter is 44.3 μm. The final contact pressures were 22.7 MPa, 302.0 MPa, 402.0 MPa, and 581.0 MPa for 1.0% RH, 2.5% RH, 5.0% RH, and 50.0% RH, respectively. The ta-C started at 517 MPa mean Hertzian contact pressure and a 35.1 μm contact diameter. The final contact pressures were 28.3 MPa,

77.9 MPa, 184.0 MPa, and 295.0 MPa for 1.0% RH, 2.5% RH, 5.0% RH, and 50.0% RH, respectively. PEEM studies on the 50.0% tracks reveal that the chemical state is almost identical to that of the unworn films. Contrasting this behavior are the tracks created at 1.0% RH. As sliding begins, there are not enough passivating species in the environment to terminate the dangling bonds formed for either ta-C or UNCD, and the resulting friction coefficients are high (0.6 for ta-C, 0.25 for UNCD). High friction leads to a high wear rate, and the track width grows, which lowers the contact pressure. ta-C never recovers from this state, and has high, fluctuating friction for the entire 5000 cycles. A Fourier transform of this ta-C friction plot is featureless, suggesting the fluctuations simply come from the random occurrences of bonds breaking and forming across the pin/flat interface. The UNCD track does recover to low friction after 2660 cycles. The topography of this track was heavily modified from both wear and from deformation of the silicon substrate, both of which contributed to lowering the contact pressure.

The NEXAFS results show that the chemical state of both tracks made at 1.0% RH is similar, suggesting the mechanism and type of passivation is the same. Specifically, both tracks are heavily oxidized, which is assumed to come from the dissociative adsorption of water molecules. These species are what passivate the broken carbon bonds. The trend between final contact pressure and relative humidity gives evidence that a passivation mechanism is at play in these systems. In an environment with a relatively high partial pressure of water (50.0% RH), the system can accommodate a higher contact pressure if the amount of available impinging species is high enough to

passivate the broken bonds within the exposure time between sliding passes. However, as the partial pressure of water in the system is lowered, low friction can only be maintained at lower contact pressure (meaning fewer broken bonds per pass). The transition between high and low friction can be understood as the transition in the critical value of number of broken bonds formed per sliding pass versus the number of bonds passivated between wear events.

The tribological behavior can also be altered by changing the initial load (and therefore the initial contact pressure). This effect is most noticeable at lower humidity. Lowering the load from 0.5 N to 0.05 N at 1.0% RH for ta-C (Fig. 3.3) makes the difference between not running in at all and running in within the first 150 cycles. This shows that change in contact pressure alone has a dramatic effect on the friction at this humidity level. This effect was also seen for the UNCD load/RH study, changing the load between 1.0 N and 0.1 N at 1.0% RH (Fig. 3.4a and Fig. 3.4b). At 50.0% RH the effect is absent, and the friction coefficient actually goes up with the lower load, presumably because of the Hertzian contact pressure going down. With excess amounts of passivating species in the environment, factors like surface roughness or true contact area are the determining factors for the initial friction and run-in behavior.

3.3.6 Insights Gained From Comparing ta-C With UNCD

Overall, the tribological behavior for ta-C and UNCD are remarkably similar, and this demonstrates the effeciveness of the passivation mechanism. However, there are some noticeable differences. The fact that, at the highest respective load and lowest

humidity, the ta-C track did not run in while all the UNCD track did provides insight into the differences between the two films. This difference in behavior is particularly notable since the constant-load ta-C tracks were created using a lower applied load than that for the constant-load UNCD tracks (0.5 N for ta-C, 1.0 N for UNCD). For this ta-C track, even though the average contact pressure reduced as the track grew wider, the bonds that continued to break during sliding were unable to be passivated sufficiently rapidly by the ambient species. The final nominal UNCD contact pressure was roughly twice as high as that for ta-C in these two cases, yet the UNCD was still able to obtain low friction at 1.0% RH. This raises the question as to why ta-C does not perform as well as UNCD.

There are several material properties (some inter-related) that could contribute to this difference. One factor is the respective sp^2 fractions of each film. Both ta-C and UNCD are almost entirely comprised of carbon, with only ~1% hydrogen in either film [3.32]. Although ta-C is amorphous and UNCD is polycrystalline, ta-C has ~20% sp^2-bonded carbon, while UNCD has less than 5% sp^2 carbon bonding (located at grain boundaries). Materials comprised of sp^2-bonded carbon can be good solid lubricants (*e.g.*, graphite [3.1], diamond-like carbon [3.33, 34]). Double bonds are easier to break in the presence of oxygen and water, and they are also more reactive once broken. Therefore a material with a higher percentage of sp^2 bonds would need a higher amount of passivating species in the environment to passivate the dangling bonds before they bond across the interface. Another consideration is the difference in surface roughness (~0.1 nm RMS for ta-C compared to ~10 nm RMS for UNCD). The fact that ta-C is smoother

than UNCD means that the true contact area for ta-C self-mated interfaces is closer to the apparent (Hertzian) contact area. The somewhat lower Young's modulus of ta-C will also lead to higher true contact area. Since the friction depends on the true contact area, a significantly higher contact area will mean higher friction. Therefore, the steady-state friction behavior of ta-C for low friction conditions (high humidity, low load) will be higher than for UNCD at the same conditions. It also explains why ta-C was unable to slide at a 1.0 N load, and required testing at 0.5 N. And it explains why ta-C never ran in at 0.5 N, 1.0% RH when UNCD was able to run-in at 1.0 N, 1.0% RH, considering the final average contact pressure was similar.

3.3.7 Comparing Steady-state Friction Levels

Another observation from the ta-C load/RH study pertains to the quantitative differences in the steady-state friction values for the three tracks that ran in (Fig. 3.3). The friction coefficient after run in for the 0.5 N, 50.0% RH test was ~0.05. This is less than half the value of the steady-state friction for the 0.05 N tracks at both 1.0% and 50.0% RH. This can be explained by the considering that the friction force is directly proportional to the true contact area, and that the contact area is a sublinear function of the normal force due to the non-linear contact mechanic nature of asperities [3.35]. Although reducing the normal load decreases the contact area, and thereby decreases the friction force, in this range the ratio of friction force to normal force (*i.e.*, the friction coefficient) increases. The effect, for ta-C, is a factor of two increase in the friction coefficient for an order of magnitude decrease of the load [3.36].

3.3.8 Oxidation Related to Total Wear

The level of oxidation for ta-C and UNCD tracks is also a measure of the total number of broken bonds, which is related to the wear. The above results showed that the RH level alone can control the rate at which these surfaces run in. The only differences between the tribometer tests in the constant load study are the RH level and number of run-in cycles. They start out with the same load, substrate coating, and sphere coating. They run for the same number of cycles, and all of the UNCD tracks achieve similar steady-state friction coefficients (0.008-0.021), while all but the 1.0 N, 1.0% ta-C track run in to 0.046-0.078. NEXAFS data reveal that the tracks which run in quickly and have low wear (made at higher humidities) are nearly chemically identical to the unmodified film surface. Few bonds are broken during sliding, likely during the few cycles of higher friction, and only a slight amount of oxidation of the track is observed. Chemically, the tracks from the load study that had the shortest run-in period were the most similar to the unworn films (middle spectra in Fig. 3.5b,c and Fig. 3.6b,c).

All UNCD tracks with a 1.0 N load achieved nearly the same steady-state friction of 0.02 +/- 0.01 regardless of their individual oxygen state. For example, the 1.0 N, 1.0% RH track, which had a large amount of oxygen bonded almost entirely as C-O, had a similar friction coefficient (slightly lower, even) than the other tracks which had less oxygen overall and exhibited a mixture of C=O and C-O bonding (Fig. 3.6c, bottom two spectra). The spectra are nearly identical to the respective ta-C tracks (Fig. 3.5c, bottom two spectra). The UNCD and ta-C O 1s spectra at the maximum respective loads for both

the 1% RH and 50% RH cases are directly compared in Fig. 3.10. The spectra for the 50.0% RH UNCD and ta-C tracks have the same line shape, which shows a mixture of π- and σ-bonded oxygen. Comparing those spectra to the spectra from the 1.0% RH tracks highlights the clear changes that occur in tracks made at low humidity and that experienced higher wear. There is a dramatic reduction in the ratio of π- to σ-bonded oxygen (*i.e.*, a large increase in relative σ-bonded oxygen, Fig. 3.12b) that accompanies the increase in overall oxygen content. These relative and absolute amounts of C–O bonding give insight into the UNCD wear history. Mainly, that the amount of oxidation is directly correlated to the amount of wear a track experienced. This is similar to what was seen for ta-C, although low friction was never achieved. The tribometry for UNCD shows the oxidation state does not affect the steady-state friction behavior. This indicates that ta-C and UNCD are best tribologically either in conditions where no surface bonds are broken during sliding (*i.e.*, the surface remains mostly identical to the as-deposited surface). This is supported by the fact that the intensity and line shape for the spectra from the 50.0% RH tracks is nearly identical to the spectra from the respective unworn films. The other low friction conditions are where broken bonds are passivated with oxygen species, which in this case are hydroxyl or other singly-bonded oxygen groups.

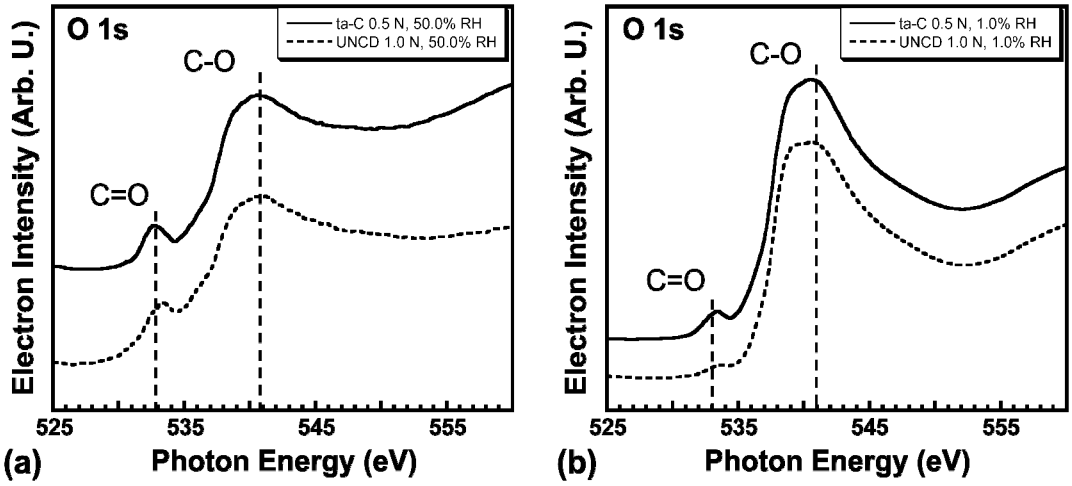

Fig. 3.12: (a) Oxygen *K*-edge spectra for ta-C and UNCD from 50.0% RH environments (amplified intensity axis compared to (b)), (b) Oxygen *K*-edge spectra for ta-C and UNCD from 1.0% RH environments.

3.4 Summary

This work compares the self-mated tribological behavior of two ultra-hard, highly sp^3-bonded, nearly H-free, carbon films, ta-C and UNCD, as a function of load and RH. The spectroscopic results do not show the presence of any graphitic carbon in the worn regions, which proves definitively that graphitization is not the lubrication mechanism for these films and the conditions tested. There is evidence of amorphization in some of the wear tracks that experienced high friction and high wear. However, the tracks that ran in quickly and experienced little wear showed barely any signs of amorphization, indicating that amorphization is not necessary for low friction and wear. And the ta-C track that never ran in (0.5 N, 1.0% RH) experienced the highest amount of amorphization. This

shows that amorphous carbon alone, or an increased fraction of amorphous carbon, can not lubricate these interfaces.

There is a distinct trend in the type and quantity of oxygen bonding in both the ta-C and UNCD wear tracks created at different RH levels which demonstrate that dissociative adsorption of water from the vapor is required to passivate the dangling broken bonds produced by sliding contact. Tracks created at successively lower RH levels have increasingly higher amounts of oxygen bonded in the track, and the type of oxygen bonding is more σ- than π-bonded, in the form of hydroxyl bonding, compared to tracks created in higher RH environments. In order to have low friction and low wear, the interface must be sufficiently passivated with these species between sliding passes.

Both ta-C and UNCD show a trend of increasing number of run-in cycles with decreasing RH. This suggests that the run in behavior, or in other words the rate at with which the interface will reach steady-state, is determined by the vapor environment during sliding. The tracks created at the low RH (1.0%) are also the ones that have higher overall friction and higher wear. ta-C, which has a larger amount of sp^2-bonded carbon, a smoother surface, and a lower modulus compared to UNCD, has higher friction and is more sensitive to the environment than UNCD. Previous studies have suggested that carbon films with increased sp^2 fractions exhibit lower friction and wear by making films more lubricious. Our results suggest that this simple condition is not sufficient to guarantee low friction and wear, and the dependence of the tribochemistry on the contact

pressure and environment must be considered in order to better predict and control the tribological performance.

3.5 Chapter 3 References

[3.1] F. P. Bowden, and J. E. Young, Proceedings of the Royal Society of London, Series A (Mathematical and Physical Sciences) **208**, 444 (1951).
[3.2] M. Seal, Proceedings of the Royal Society of London, Series A (Mathematical and Physical Sciences) **248**, 379 (1958).
[3.3] M. Casey, and J. Wilks, Journal of Physics D: Applied Physics **6**, 1772 (1973).
[3.4] B. Samuels, and J. Wilks, Journal of Materials Science **23**, 2846 (1988).
[3.5] S. E. Grillo, and J. E. Field, Journal of Physics D (Applied Physics) **33**, 595 (2000).
[3.6] A. Erdemir, G. R. Fenske, A. R. Krauss, D. M. Gruen, T. McCauley, and R. T. Csencsits, (Elsevier, Switzerland, 1999), pp. 565.
[3.7] M. N. Gardos, and B. L. Soriano, Journal of Materials Research **5**, 2599 (1990).
[3.8] H. I. Kim, J. R. Lince, O. L. Eryilmaz, and A. Erdemir, Tribology Letters **21**, 53 (2006).
[3.9] M. N. Gardos, and S. A. Gabelich, Tribology Letters **6**, 103 (1999).
[3.10] R. H. Savage, Journal of Applied Physics **19**, 1 (1948).
[3.11] R. R. Chromik, A. L. Winfrey, J. Luning, R. J. Nemanich, and K. J. Wahl, Wear **265**, 477 (2008).
[3.12] R. O. Brennan, Journal of Chemical Physics **20**, 40 (1952).
[3.13] D. H. Buckley, *Surface effects in adhesion, friction, wear, and lubrication* (Elsevier Scientific Pub. Co. ; Distributors for the U.S. and Canada, Elsevier North-Holland, Amsterdam; New York; New York, 1981).
[3.14] M. A. Hamilton, A. R. Konicek, D. S. Grierson, A. V. Sumant, O. Auciello, W. G. Sawyer, and R. W. Carpick, (ASME, Miami, FL, United states, 2009), pp. 9.
[3.15] A. R. Konicek, D. S. Grierson, P. U. P. A. Gilbert, W. G. Sawyer, A. V. Sumant, and R. W. Carpick, Physical Review Letters **100**, 235502 (2008).
[3.16] G. T. Gao, P. T. Mikulski, G. M. Chateauneuf, and J. A. Harrison, Journal of Physical Chemistry B **107**, 11082 (2003).
[3.17] I. P. Hayward, I. L. Singer, and L. E. Seitzman, Wear **157**, 215 (1992).
[3.18] I. Ishii, and A. P. Hitchcock, Journal of Electron Spectroscopy and Related Phenomena **46**, 55 (1988).
[3.19] S. G. Urquhart, A. P. Hitchcock, R. D. Priester, and E. G. Rightor, 1995), pp. 1603.
[3.20] S. Anders, J. Diaz, J. W. Ager, III, R. Y. Lo, and D. B. Bogy, Applied Physics Letters **71**, 3367 (1997).
[3.21] D. S. Grierson, A. V. Sumant, A. R. Konicek, T. A. Friedmann, J. P. Sullivan, and R. W. Carpick, Journal of Applied Physics **107** (2010).
[3.22] K.-J. Kim, H. Lee, J. H. Choi, H. K. Lee, T. H. Kang, B. Kim, and S. Kim, Journal of Physics Condensed Matter **20** (2008).
[3.23] E. Gullikson, X-Ray Interactions With Matter, http://henke.lbl.gov/optical_constants/,

[3.24] N. J. Mehta, S. Roy, J. A. Johnson, J. Woodford, A. Zinovev, Z. Islam, A. Erdemir, S. Sinha, G. Fenske, and B. Prorok, (Materials Research Society, Warrendale, PA 15086, United States, Boston, MA, United States, 2005), pp. 49.
[3.25] A. Laikhtman, A. Lafosse, Y. Le Coat, R. Azria, and A. Hoffman, Surface Science **551**, 99 (2004).
[3.26] X. Gao, L. Liu, D. Qi, S. Chen, A. T. S. Wee, T. Ouyang, K. P. Loh, X. Yu, and H. O. Moser, Journal of Physical Chemistry C **112**, 2487 (2008).
[3.27] Y. Qi, E. Konca, and A. T. Alpas, Surface Science **600**, 2955 (2006).
[3.28] Y. Okamoto, Physical Review B (Condensed Matter) **58**, 6760 (1998).
[3.29] G. Zilibotti, M. C. Righi, and M. Ferrario, Physical Review B (Condensed Matter and Materials Physics) **79**, 075420 (10 pp.) (2009).
[3.30] S. Skokov, B. Weiner, and M. Frenklach, Physical Review B (Condensed Matter) **55**, 1895 (1997).
[3.31] S. J. Sque, R. Jones, and P. R. Briddon, Physical Review B (Condensed Matter and Materials Physics) **73**, 85313 (2006).
[3.32] A. R. Krauss *et al.*, Diamond and Related Materials **10**, 1952 (2001).
[3.33] O. L. Eryilmaz, and A. Erdemir, Wear **265**, 244 (2008).
[3.34] J. Andersson, R. A. Erck, and A. Erdemir, Surface & Coatings Technology **163-164**, 535 (2003).
[3.35] J. A. Greenwood, and J. B. P. Williamson, Proceedings of the Royal Society of London. Series A, Mathematical and Physical Sciences **295**, 300 (1966).
[3.36] T. W. Scharf, and I. L. Singer, Tribology Transactions **45**, 363 (2002).

4. Frictional Switching Behavior of Ultrananocrystalline Diamond

---

4.1 Introduction

The previous chapter discussed the environmental dependence of UNCD and ta-C. During the study of these films, we discovered a surprising and dramatic behavior where the change from low to high friction upon reducing the RH could be completely reversed when increasing the RH again. Here we describe this remarkable phenomenon.

Sharp switching behavior is the opposite of that seen for hydrogenated diamond-like carbon (H-DLC) films transitioning between dry and humid environments. Dickrell *et al.* showed that the friction dependence H-DLC films have on RH can be explained by a fractional coverage model [4.1, 2]. They see a slow, continuous increase in friction coefficient as the RH is raised. The surface is covered with two different types of species, one that is low friction (the native film) and one that is high friction (adsorbed species from dissociated water). The RH level determines the rate of adsorbed species, and the sliding velocity determines the rate of layer removal. The friction coefficient is determined by the relative coverage fraction of the two species.

4.2 Initial Experiments

In the first observation of the switching phenomenon, ultrananocrystalline diamond (UNCD) films were coated on a 1x1 cm^2 Si flat and a 3 mm diameter Si_3N_4 sphere (as in Chapter 2). Using linear reciprocation, a 500 mN load, and 1 mm/s sliding

velocity, a wear track was created in a N_2 environment with relative humidity (RH) starting above 4.0%. The friction coefficient as a function of cycles was recorded, and RH levels were documented by hand every ~25 cycles. After 350 sliding cycles, the RH was lowered by flushing the system with only dry N_2 (Fig. 4.1).

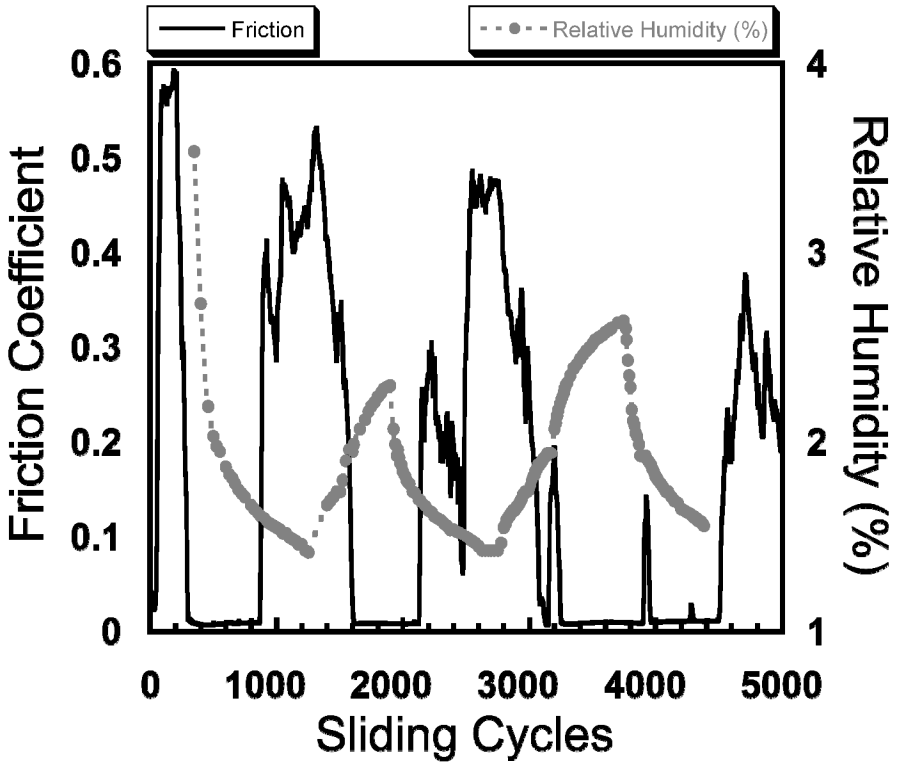

Fig. 4.1: Friction data from UNCD track exhibiting first instance of switching behavior.

At cycle 865 the friction coefficient was 0.009. As the RH dropped below 1.61%, the friction coefficient rose to 0.353 by cycle 890. This is over an order of magnitude increase in the friction coefficient for a RH drop of ~0.05%, occurring in just ~25 sliding cycles. The friction coefficient was high and erratic, reaching a maximum of ~0.53, and the RH eventually bottoms out at ~1.43%. Humidified N_2 was then introduced back into

the chamber. At cycle 1546 the friction coefficient was at 0.266, and the RH had increased to 1.87%. By cycle 1619, the RH had increased to 2.02% and the friction coefficient had dropped back down to 0.008. This cycle is reproduced four times in the data set, where a period of high friction with low RH is followed by the low friction value as the RH is increased again. There is some hysteresis, as the transition from low to high friction occurs at ~1.6% RH, and the transition from high to low friction is at ~1.9% RH. The surface switches sharply between high and low friction with small changes in RH, and is henceforth referred to as UNCD 'switching' behavior. In each switching instance the friction becomes high and erratic at low humidity, and then at higher humidity recovers to almost exactly the same initial value. The friction during the higher RH sections is also quite stable.

Further sets of similar experiments using UNCD films (grown in different runs) saw the same behavior. Fig. 4.2 shows another self-mated UNCD friction plot. In addition to varying the RH, the load is also changed at specific intervals during the test. The track started out at 500 mN, again with a combination of dry N_2 and humidified N_2 providing RH control, 1 mm/s sliding velocity, and a 500 μm track length. RH was still be recorded by hand, and in this case only 20 measurements were recorded over the 12000 cycles. Fig. 4.1 gives a good indication about the pattern of RH changes. As sliding begins (Fig. 4.2) and the RH is lowered, the friction does not sharply increase, but instead slowly rises from its minimum value of ~0.0035 up to ~0.02 before spiking at ~0.0375. The RH is increased again until lower friction is achieved, but the system does not recover to the lower value and instead is at ~0.01. It is possible that the system

reached some sort of new steady-state behavior around cycle 5000 that is different than at cycle 1000. At cycle ~6000 the load was increased from 500 mN to 750 mN. Again the RH was lowered, and again the friction slowly trended upward (from ~0.01 to ~0.023) before switching to the higher friction state. Interestingly, the high friction state for this system is only ~0.04 (and spiky) whereas it was an ~order of magnitude higher (0.2-0.5) for the data in Fig. 4.1. This fact, combined with the lack of sharp switching behavior, implies there is something different about this second system. Finally, after the system recovers (more sharply) after cycle 8000, the load was increased from 750 mN to 1.0 N at cycle ~9200. A last, sharper switching transition is observed, showing that the ability to switch is not fixed at a certain load.

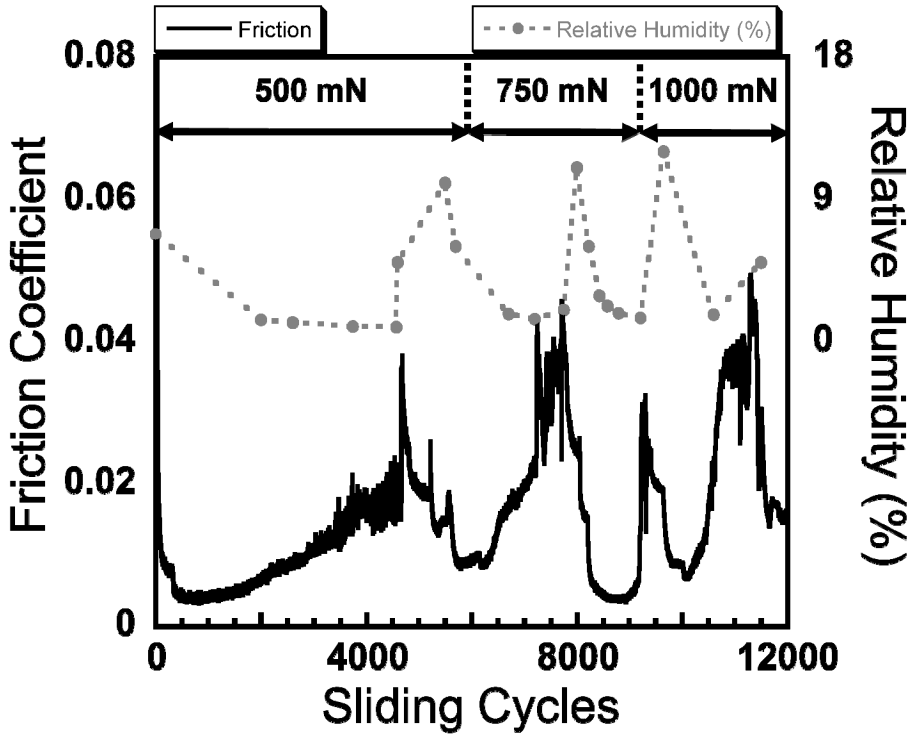

Fig. 4.2: Second example of UNCD switching behavior, including change in load

Results from this second test suggested sharp transition behavior is more likely at high loads. With this in mind, a final test was performed using a 1.0 N load, and otherwise identical parameters, to determine if the switching behavior further evolved with number of switching occurrences. Fig. 4.3 shows a test where the system switches a total of 10 times between the low and high friction state. The friction behavior to this third preliminary test is more similar to the first test (Fig. 4.1) where the change between the low and high friction state covers almost two orders of magnitude, and the switching is sharp. The behavior does evolve with number of switches, which could be due to the accumulated wear. As more time is spent in the high friction state, the system is not able to return to the previously low friction value (cycle 3500). As the RH decreases, the friction slowly increases until the debris is cleared from the contact and a transition occurs (cycles 3500 to 5500).

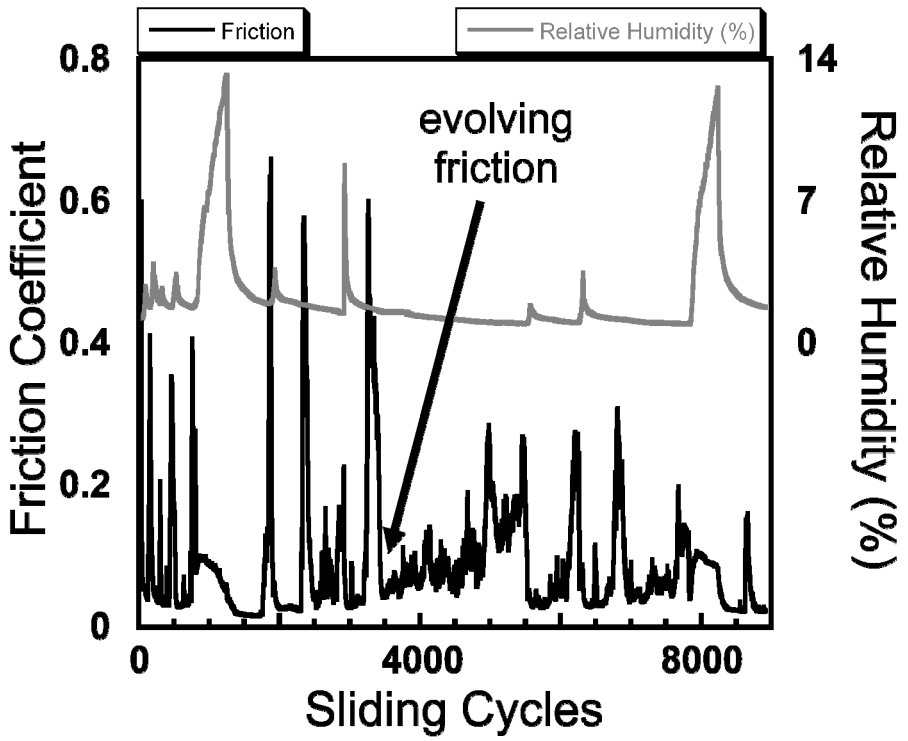

Fig. 4.3: UNCD switching friction plot showing a total of 10 switches. Friction behavior evolves starting at cycle 3500 (arrow) and is not able to return to the low friction value until cycle 5500.

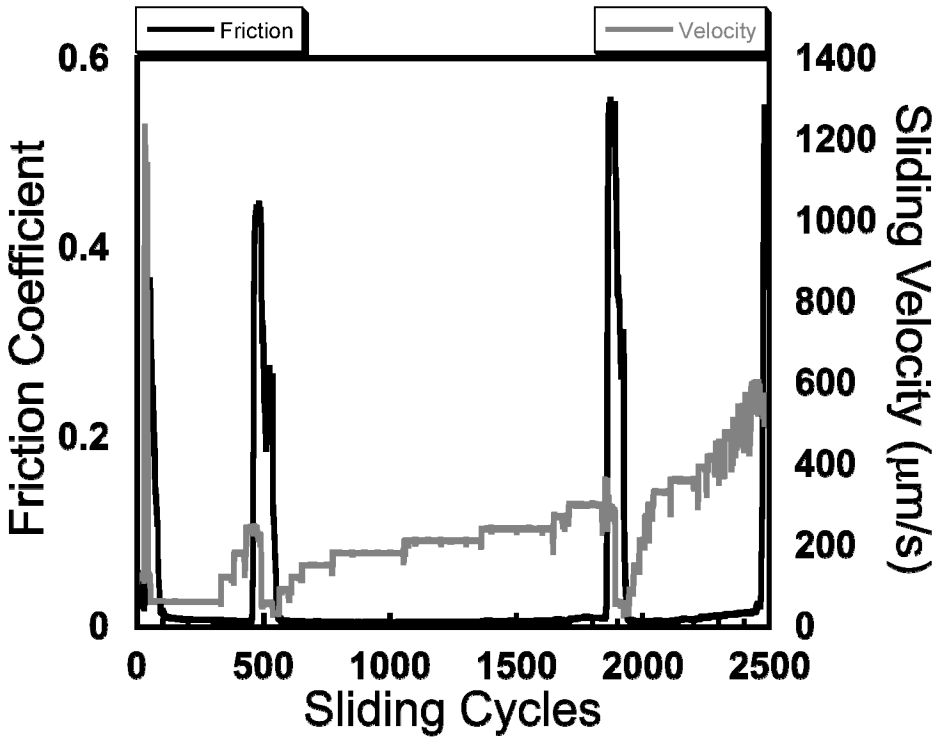

Fig. 4.4: UNCD friction data as a function of sliding velocity with a 1.0 N load, RH between 0.7-0.9%.

Fig. 4.4a is a plot of friction coefficient as a function of cycle for changing sliding velocities. The load was kept constant at 1.0 N and the RH was kept between 0.7% and 0.9%. Here the friction is low (~0.005) even with only 0.9% RH. The difference between this test and previous tests (Chapter 3, and Fig. 4.1, Fig. 4.2, and Fig. 4.3) is that the sliding velocity is only 60 μm/s, compared to the usual 1000 μm/s. The increase in friction with increased sliding velocity further supports the passivation mechanism by showing that the reduced exposure time prevents sufficient passivation of the surface,

which increases dangling bond interaction across the interface. This also shows the transition behavior can be triggered by changing the exposure time instead of the amount of water.

Next we describe an experiment designed to elucidate the mechanism behind the switching behavior for UNCD. The same sequence of environmentally controlled tribometry followed by PEEM measurements determine friction and chemical changes as UNCD interfaces run in, experience a switching transition, and recover. Recent density functional theory (DFT) work provides a possible explanation as to the driving mechanism.

4.3 Systematic Switching Experiments: Experimental Methods

A Si flat and a Si_3N_4 sphere were coated as in Chapter 2. All tracks were made with the same sphere. The experiment involved creating five wear tracks (Fig. 4.5). By creating tracks that were stopped at each point along a switching transition, we can examine the chemical changes that have occurred. Track 1 starts sliding and is stopped after it has run-in. Then, Track 2 undergoes run-in and then has the RH lowered and is stopped just as it transitions to high friction. Track 3 follows the same path as track 2, but then experiences some cycles of high friction. Track 4 follows the same path as track 3, but then has the RH increased again to recover to low friction, and is stopped. Finally, the last track goes through the full switching path and is run for a period of low friction after the transition.

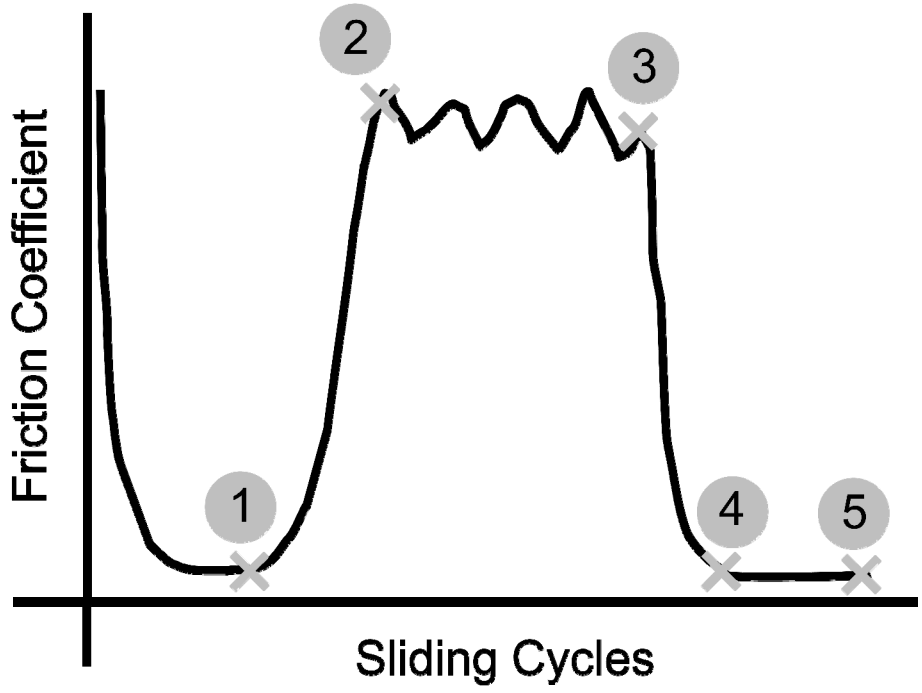

Fig. 4.5: Experimental schematic for wear tracks to test switching behavior

Because of the slow rate that the RH changes in the system, it was not possible to precisely determine the number of cycles each track spent in each phase of the switching transition. Ideally it ought to be chosen to be the same, to ensure that each track had similar wear and chemical modifications during each section. However, due to time limitations and instrumental challenges, that proved to not be possible. The most important goal was achieved: to characterize the surfaces before a transition, during the high friction phase, and after it has recovered to see what conclusions can be drawn about the behavior.

As in Chapter 3, the wear tracks are characterized post-mortem by scanning white light interferometry to measure wear, and by PEEM to measure the chemical bonding

changes. These measurements are related to the tribological performance of each track and the point along the transition at which it was stopped.

4.4 Systematic Switching Experiments: Results and Discussion

All of these tracks were created at 1.0 N and 1 mm/s sliding speed. The first run-in track had 2000 total cycles, and the humidity ranged between 3% and 17% (Fig. 4.6). The RH was initially set at 5% for this track, but it dipped below 4% around cycle 200 (Fig. 4.6, A), causing a transition to high friction. The friction decreased back to 0.034 at cycle 500 (Fig. 4.6, B), likely due to sphere wear (*i.e.,* lower contact pressure resulting from the larger contact area that occurs with a worn sphere). The friction remained slightly higher than normal, and spiky, until the RH was increased from 4% to 7% at approximately cycle 1200 (Fig. 4.6, C). Then the friction remained low and constant at 0.018 for the remaining cycles. The friction profile was not ideal for our desired experiment since there is the period of higher friction. However, we believe that the only critical part of run-in is conditioning the sphere by mechanical polishing and chemical conditioning (as in Chapter 3). Any sphere that has run in is nearly identical, mechanically and chemically, to other spheres that have run in.

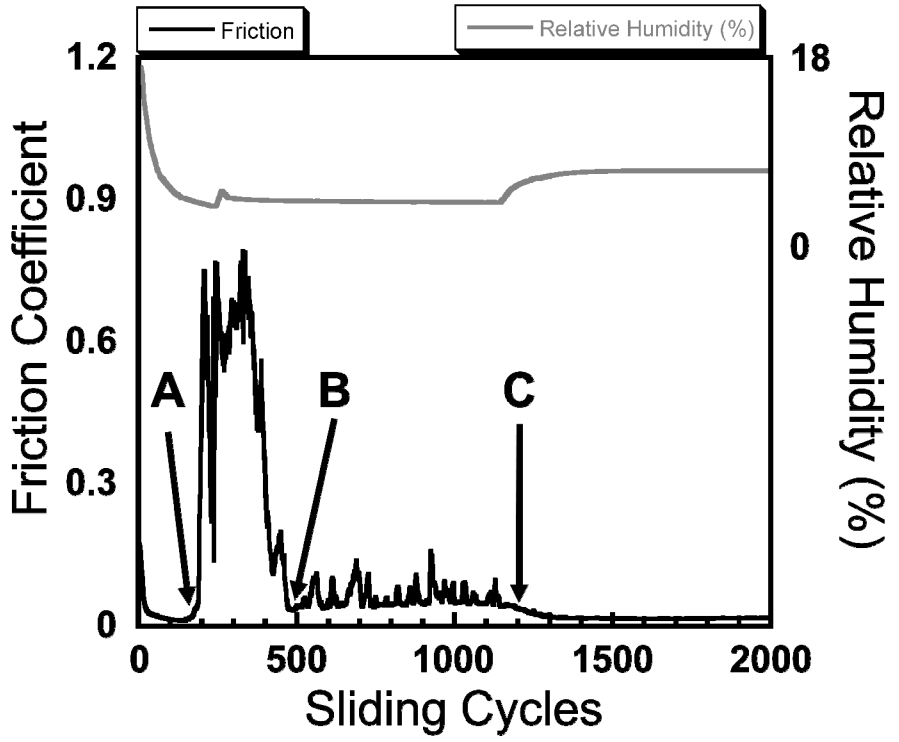

Fig. 4.6: Friction coefficient data with RH for switching transition test, track 1 (first sphere run-in)

Track 2 was run for just over 1500 total cycles (Fig. 4.7). The run-in occurs in less than 100 cycles (Fig. 4.7, A), with the RH around 7%. After ~1100 cycles (Fig. 4.7, B), the RH was lowered to cause a transition, which occurred just after cycle 1500 (Fig. 4.7, C). At this point the test was stopped.

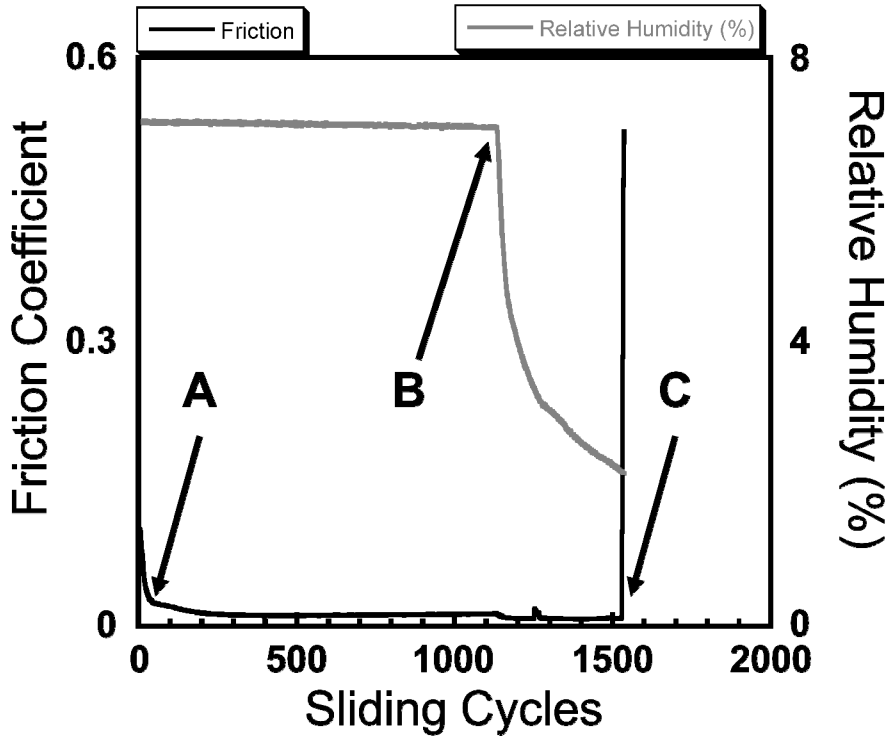

Fig. 4.7: Friction coefficient data with RH for switching transition test, track 2

Fig. 4.8 shows the friction data for Track 3. This track runs in for just over 1000 cycles before the RH is lowered. It then experiences ~800 cycles of high friction.

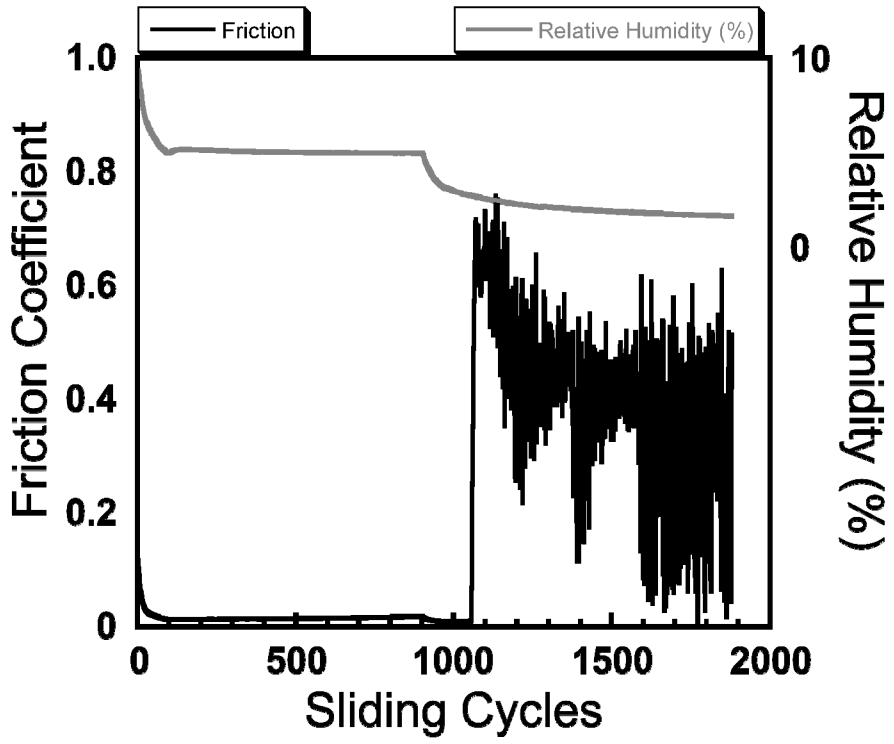

Fig. 4.8: Friction coefficient data with RH for switching transition test, track 3

Friction data for Track 4 are shown in Fig. 4.9. This track runs in at higher humidity for almost 1300 cycles (Fig. 4.9, A) before the humidity is lowered enough to transition. The system runs at higher friction for over 100 cycles, and then the humidity is raised again (Fig. 4.9, B). The friction transitions back to a low state just after cycle 1400 (Fig. 4.9, C) and the test is stopped.

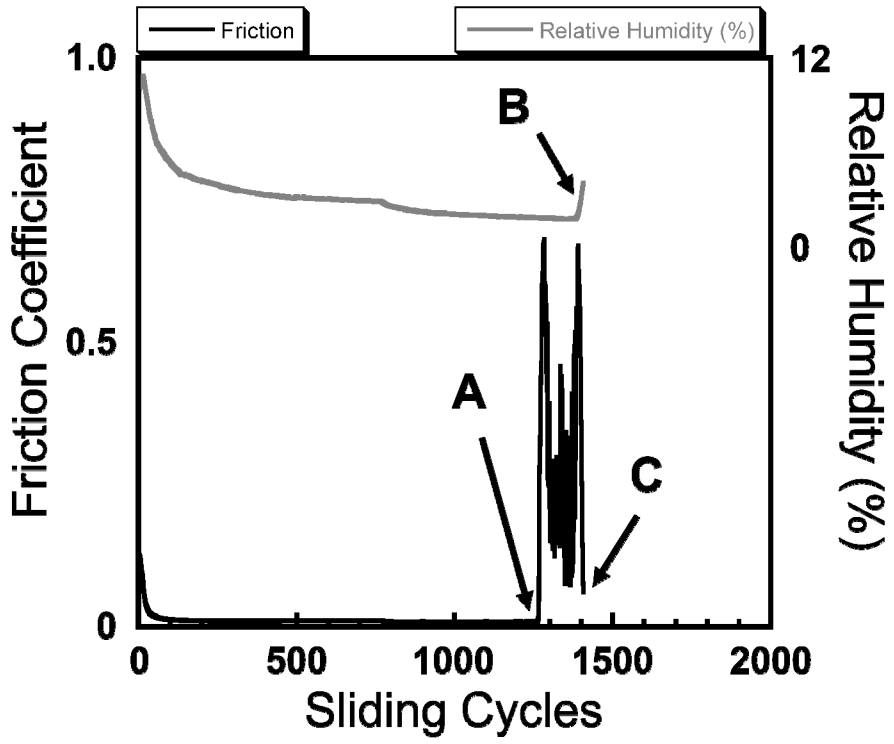

Fig. 4.9: Friction coefficient data with RH for switching transition test, track 4

Finally, Fig. 4.10 shows the friction plot for track 5 which undergoes the full transition and then runs for 300 cycles in low friction after the transition. Track 5 only ran for 200 cycles in high friction.

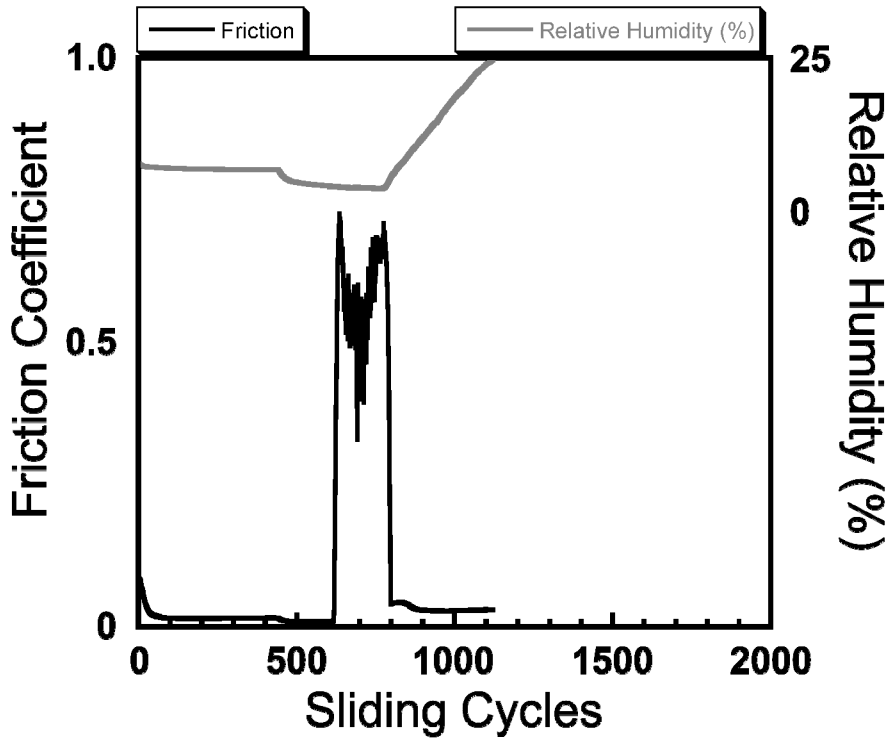

Fig. 4.10: Friction coefficient data with RH for switching transition test, track 5

As was mentioned, due to experimental limitations, it was not possible to keep the number of cycles in each phase of the transition constant for the five tracks. Also, there had to be a compromise over the total number of cycles, since too many cycles in the high friction state would possibly wear out the sphere. As shown in Table 4.1, there is little uniformity between the total cycles, or cycles during any of the phases of the switching transition for the five tracks. Most notably, Track 1 included, undesirably, 200 cycles of high friction. However, we will show that the chemical changes that are revealed in PEEM measurements tell a consistent story. As well, the 800 cycles experienced in the high friction phase for track 3 is noteworthy, since that should be the

track that has the highest amount of chemical and topographic modification (high friction is linked to similar changes in Chapter 3).

Track label	*Cycles to run-in*	*Cycles in high friction*	*Cycles after transition*	*Total Cycles*
Track 1	1300	200	N/A	2000
Track 2	1525	6	N/A	1536
Track 3	1050	800	N/A	1882
Track 4	1250	125	17	1409
Track 5	625	175	323	1123

Table 4.1: Number of sliding cycles during run-in, during the high friction phase after a transition, cycles run after transitioning back to low friction, and total sliding cycles for the five tracks.

Using PEEM, NEXAFS spectra were acquired from the center of each of the five wear tracks, as well as from an unworn portion of the sample. For each track, the center was selected as the region of interest since that is the place where the exposure time and sliding velocity are constant during each cycle. Since no unique information is conveyed in the photoemission images, so they are not shown here.

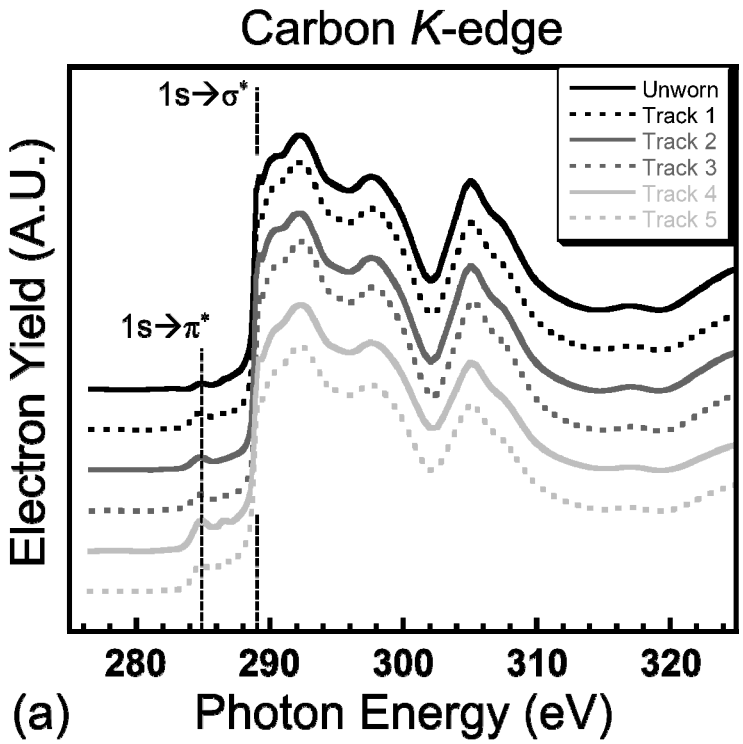
Carbon K-edge
1s→σ*
1s→π*
Unworn
Track 1
Track 2
Track 3
Track 4
Track 5
Electron Yield (A.U.)
280
290
300
310
320
Photon Energy (eV)

(a)

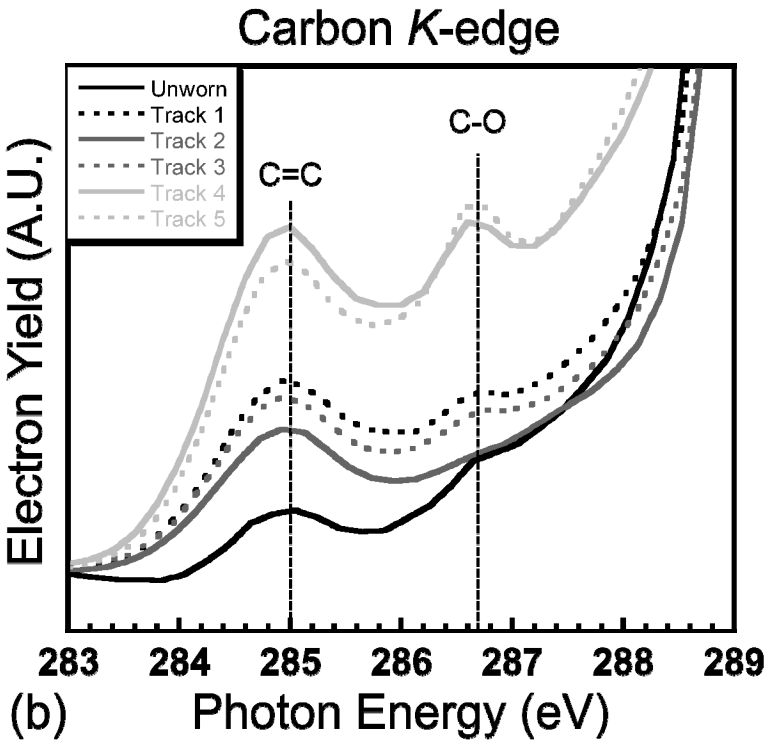
Carbon K-edge
Unworn
Track 1
Track 2
Track 3
Track 4
Track 5
C=C
C-O
Electron Yield (A.U.)
283
284
285
286
287
288
289
Photon Energy (eV)

(b)

Fig. 4.11: Carbon K-edge NEXAFS data from unmodified UNCD and the five wear tracks, (a) full spectra separated, and (b) zoomed into the pre-edge. The solid/dashed lines are just to distinguish the different spectra.

The carbon *K*-edge spectra can be grouped into four categories: unworn, slightly worn, moderately worn, and heavily worn/recovered (Fig. 4.11). The first category only includes the solid black line (top spectrum in Fig. 4.11a and bottom-most spectrum in Fig. 4.11b) which is unworn UNCD. It displays all of the usual spectral features of unworn UNCD (discussed in Chapter 2).

Track 2 (solid dark gray line), which experienced only 6 cycles of high friction, is the second category, and is the closest in line shape to the unworn spectrum. There is some rehybridization evident from the increase in the C 1s$\rightarrow\pi^*$ transition at 285.0 eV. This agrees well with the friction data since Track 2 ran in quickly and experienced only a few cycles of high friction.

The third category involves Track 1 and Track 3 (black and dark gray dotted lines). The spectra from these tracks show even more rehybridization of sp^3- to sp^2-bonded carbon, as well as a noticeable increase in area and peak at 286.7 eV, which is from the C-O Rydberg orbital. There is also increased area around 288 eV (corresponding to the C-O σ^* orbital), but the edge jump after 288.5 eV makes resolving a peak difficult. These tracks are the first run-in track, which experienced 200 cycles of high friction, and the track that was stopped during high friction after 800 cycles.

The final group, which are from the last two tracks made, are the spectra that differ the most from the unworn spectrum. Track 4 and Track 5 were tracks that were stopped just after transitioning back to low friction, and stopped over 300 cycles after the

transition, respectively. They show the highest amount of rehybridization (285.0 eV) and the greatest intensity of the C-O peak (286.7 eV). They also have the greatest increase in area at approximately 288 eV, also indicative of C-O bonding.

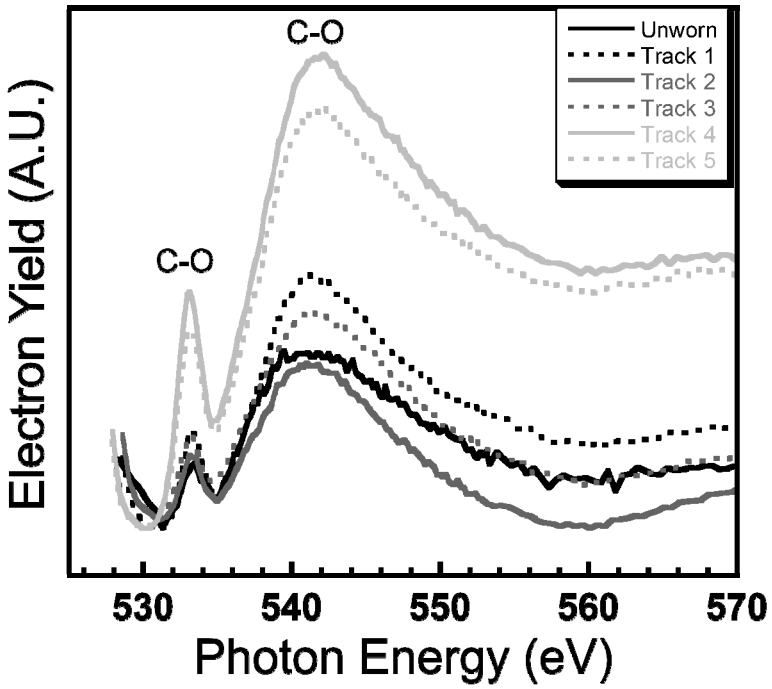

Fig. 4.12: Oxygen *K*-edge spectra from unworn UNCD and the five switching tracks

The oxygen *K*-edge spectra are shown in Fig. 4.12. These are from the same areas as the carbon data in Fig. 4.11. The oxygen trends match well with the carbon data. The peaks at ~533.0 eV and 541 eV correspond in relative intensity with the C-O peak in the carbon *K*-edge data. There is nothing significantly different about the shape of the spectra, just their relative intensity. None of the oxygen spectra have a high overall intensity, suggesting that during none of the tracks has there been an extensive amount of wear. This is a reasonable finding since wear of the sphere as each track is made lowers

the contact pressure, and no track spends very many cycles in the high friction state (compared to 2000-5000 cycles seen by UNCD and ta-C in Chapter 3).

This switching behavior has the characteristics of an instability, such as in a phase transition, suggesting there is a "run away" behavior. This indicates there is a positive feedback mechanism. This feedback stems from the fact that, for diamond, the presence of adsorbed water reduces the energy barrier for further adsorption. Recent density functional theory (DFT) calculations by Manelli *et al.* have shown that water adsorption kinetics change depending on whether or not there is already water adsorbed on the surface [4.3]. DFT calculations on diamond (001) surfaces showed that the energy barrier for molecular water physisorption was lower when there was already molecular water physisorbed to the surface compared to a bare surface. This is because the carbon dimers are more strongly polarized and the incoming water molecule can form hydrogen bonds to molecular water that has already adsorbed. Because of this they predict that water molecules will not uniformly wet a surface, but rather will grow in islands around existing adsorbed water molecules. The other important result was that the dissociation of the water molecules (an important step in passivation) is also dependent on the existing water coverage. They found that the energy barrier for dissociation of water with existing physisorbed molecules present was one order of magnitude lower than that for a lone water molecule. They also saw dissociation with no energy barrier if there were dissociated fragments in the vicinity of the water molecule. This work predicts a cross-over point between the two bonding regimes, for either low or high dangling bond concentrations.

For the switching behavior we observe, controlling the RH adjusts the availability of water molecules in the environment that can adsorb and dissociate. There are then two possible steady-state situations. For RH above a saturation level (~1.8%), the surface already has a sufficient level of adsorbed water, and there are enough water molecules in the environment to continue to adsorb, dissociate, and passivate any dangling bonds formed during sliding. These water molecules have a lower energy barrier to adsorb and dissociate because of a surface that already has a high fractional coverage of adsorbed species. The system therefore maintains low friction and low wear. There is positive feedback as the high surface coverage of adsorbed species promotes further adsorption and dissociation.

However, for RH levels that drop below the necessary saturation level (~1.6%), the environment now has an insufficient availability of species to adsorb. For each sliding pass the sphere makes, more bonds are being broken than are being passivated. This in turn increases the energy barrier for further adsorption and dissociation, creating a positive feedback cycle that deprives the surface of the necessary passivated species. Dangling bonds on the two counterfaces then strongly interact, causing high friction and high wear.

This also explains why there is hysteresis in the RH level required to return the system to the low friction state. When transitioning from the low to high friction state, the surface already is sufficiently covered with water and dissociated water groups (hydrogen and hydroxyl). In this state the energy barrier to adsorb water is lower, so the RH level

needed to ensure water adsorbs and dissociates is lower. The transition to high friction occurs when this layer of passivation, or the islands of passivated species, is largely removed. In order to reestablish the necessary level of passivation to reduce interactions across the interface, the system needs a higher level of available water to recover to low friction. Since the adsorption energy barrier in this state is higher, more water is necessary in order to increase the probability of adsorption.

4.5 Summary

This Chapter discussed the new, dramatic phenomenon of frictional switching behavior of self-mated UNCD. Small decreases in RH below a critical value cause the friction coefficient of the interface to sharply increase and remain high. As the RH is increased to a higher level than where the first transition occurred, the system quickly "heals" to a low friction state. Spatially-resolved NEXAFS spectroscopy shows the transition to high friction causes rehybridization of sp^3- to sp^2-bonded carbon, and an increase in C-O and O-H species bonded to the surface. While the surface chemistry of Track 2 (which experienced almost no cycles of high friction) and Track 5 (which went through a full transition) are very different (far more oxidation for Track 5), the friction coefficients during the low friction state are indistinguishable. This demonstrates that it is not the amount of dissociated species that is relevant, but just that they are replenished at a rate that matches their removal.

New DFT work provides an underlying mechanisms to explain this switching behavior. The DFT work predicts that the energy barrier for adsorption and dissociation are both lowered in the presence of existing adsorbed water molecules [4.3]. The two

steady-state situations are then one of high water coverage and few dangling bonds, and one of low water coverage and many dangling bonds. These would be the low friction and high friction states, respectively. When combined with the bond breaking that occurs during sliding, and the fact that the RH is varied (changing the relative amount available for adsorption), this tribological system switches between the two states by simply lowering or raising the RH below or above the saturation point which is found to be at approximately 1.6% RH (below) and 2.1% (above). There is hysteresis observed in this level of about 0.5% RH, since it requires more water vapor to reinitiate the minimum level of water adsorption needed to then fully passivated the interacting portions of the contact.

These observations are consistent with the results in Chapter 3, where it was shown that not only will the RH level be a key factor, but also the contact pressure. For a lower load, and therefore lower pressure, fewer bonds are broken per cycle. This will change the critical RH level necessary to switch the system between the two states. Also, Chapter 5 will show that by first conditioning the sphere, the tribological performance is much improved. Even though these films are very smooth, they still have asperities that interact. These asperities will be the points where the larger fractions of bonds are broken during sliding, and will be where passivation needs to occur to reduce asperity interactions and lower friction. Removing or smoothing these asperities and passivating the broken bonds will further reduce the asperity interactions, lower the asperity contact pressures, and reduce the necessary RH level required to maintain a sufficiently passivated surface

The switching phenomenon is particularly important for applications, as it shows that temporary exposure to high friction conditions does not lead to irreversible damage of the UNCD. The ability to recover to low friction demonstrates an impressive level of robustness for self-mated UNCD interfaces. It also suggests a possible avenue for creating novel forms of UNCD-based films that can be exposed to dry or vacuum conditions, such as those found in aerospace applications.

.

4.6 Chapter 4 References

[4.1] P. L. Dickrell, W. G. Sawyer, J. A. Heimberg, I. L. Singer, K. J. Wahl, and A. Erdemir, Transactions of the ASME. Journal of Tribology 127, 82 (2005).
[4.2] P. L. Dickrell, W. G. Sawyer, and A. Erdemir, Journal of Tribology 126, 615 (2004).
[4.3] O. Manelli, S. Corni, and M. C. Righi, The Journal of Physical Chemistry C (2010).

5. Examining Both Contacts in a Self-mated Ultrananocrystalline Diamond Contact

---

5.1 Introduction

One of the criticisms of only studying the chemical changes on the flat from a pin-on-flat tribometer geometry is that it is possible the pin is not changing in the same manner as the flat. The pin is in constant contact with the flat during sliding, while portions of the flat (depending on track length and contact size) are fully exposed to the environment during part of the sliding cycle. This means portions of the track have a longer exposure time to interact with the environment, which is further convolved with the extra time it takes to decelerate and accelerate at each end of the track. For linear reciprocation, the middle point of the track is the only one with a constant exposure time. The chemical passivation of the flat might then have a very different final state than that of the pin. This would depend on total wear, or total bonds broken during sliding. It also depends on the different chemical pathways each surface find to passivate or rehybridize broken bonds.

This Chapter discusses the details of an experiment which examines both the sphere and flat that made tribological contact. As mentioned in Chapter 2, PEEM can not image a non-planar surface due to the large bias applied between the sample and microscope. Instead of using PEEM, a new imaging microscopy system developed at the National Synchrotron Light Source, Brookhaven National Laboratory (described in

Chapter 2) is used to characterize both the wear tracks on the flat as well as the wear scar on the sphere. The BNL imaging apparatus uses a magnetic field to guide the photoemitted electrons toward a CCD camera, with a negative bias in front of the camera preventing off-axis electrons from being collected. The resultant set of images is similar to that from PEEM, except the signal is PEY instead of TEY. The resolution of this new system is ~50 μm, which is much lower than the ~50-100 nm resolution of PEEM. PEEM achieves this high resolution by a combination of the large negative bias, which pulls electrons perpendicularly from the sample surface, and the electron optics, which can filter electrons with the wrong path or energy. The BNL imaging chamber is not able to spatially resolve the starting electron locations to this degree.

The tribological performance of the sphere and flat, measured by friction coefficients and wear, is compared to the mechanical and chemical changes that occur on both the flat and the sphere. Profilometry measures the degree of wear and is used to calculate a wear rate. The chemical changes are determined by spatially-resolved near-edge x-ray absorption fine structure (NEXAFS) spectroscopy. Conclusions are drawn about the effect the starting state of each counterface surface has on the final state (both topographically and chemically) and this is leads to inferences about the important characteristics for a low friction, low wear interface.

5.2 Experimental Details

To produce the wear tracks, silicon flats (1x1 cm) and Si_3N_4 spheres (3 mm diameter) were coated with ultrananocrystalline diamond (UNCD) by microwave plasma chemical vapor deposition in a DiamoTek 1800 series 915 MHz, 10 kW MPCVD system

installed at Argonne National Laboratory [5.1]. The growth temperature was 650 °C, which is lower than the growth temperature for typical UNCD [5.2]. Films were grown on the flats and the spheres at the same time to a thickness of ~1 μm. The Si_3N_4 spheres had a flat spot polished on them that was positioned away from the growth source. They are mounted using this polished spot for all subsequent tests so that identifying the same spot is consistent.

Tribometry tests were created in a linear reciprocation mode. The goal was to determine the surface chemical state of the sphere and flat, and the steady-state friction value, after running in the sphere, and then after using the same sphere to create a second track. Carbon films undergo a period of higher friction and higher wear as sliding begins, called run-in, where surface asperities are worn away. The higher the initial roughness, the longer the period of run-in [5.3]. To run in the sphere, first test consisted of sliding for 5000 cycles. Then the sphere was positioned over a new part of the sample, and a second wear track was run for 3000 cycles. In both cases the tests were stopped when it was obvious a steady-state friction coefficient (constant friction over time, indicating the system has reached equilibrium) was obtained. Both tracks were created in a 5.0% relative humidity (RH) with N_2 environment, with a 1.0 N load, a 1 mm/s sliding speed, and a 500 μm track length.

To characterize the UNCD wear, scanning white light profilometry measurements were performed on the tracks using a Zygo NewView 6300 interferometer. A height profile was taken on each track with lateral resolution of ~0.5 μm and vertical resolution at 0.1 nm.

The imaging NEXAFS measurements were performed using the parallel processing imaging system at the NIST beamline U7A located at the National Synchrotron Light Source. The Si flat and Si3N4 sphere used in the tribometer tests were mounted to the metal sample arm with copper tape and carbon tape, respectively. A thin piece of carbon tape was used to prevent charging effects by groundin the coating on top of the Si flat to the metal sample arm. Because of the sphere geometry, the grounding with carbon tape was not possible. However, the spectra do not show any charging effects. Absorption spectra for the carbon *K*-edge were taken using a photon energy range of 270-340 eV, and 515-570 eV for the oxygen *K*-edge, with energy resolutions of 0.1 eV and 0.2 eV, respectively.

5.3 Results and Discussion

The friction data for the two wear tracks are shown in Fig. 5.1. The run-in track friction starts off at 0.244 +/- 0.005 for ~1200 cycles, and then the sphere and track run in after 3000 cycles to a friction coefficient of 0.0371 +/- 0.0008. When the test was stopped after 5000 cycles, the friction had reached a steady-state value of 0.0337 +/- 0.0003. The friction data for the second wear track show a run-in to 0.04 in less than 40 cycles and eventually hits a minimum of 0.022 at 200 cycles. The friction slowly increases for the remaining cycles of the test and is at 0.028 at cycle 3000.

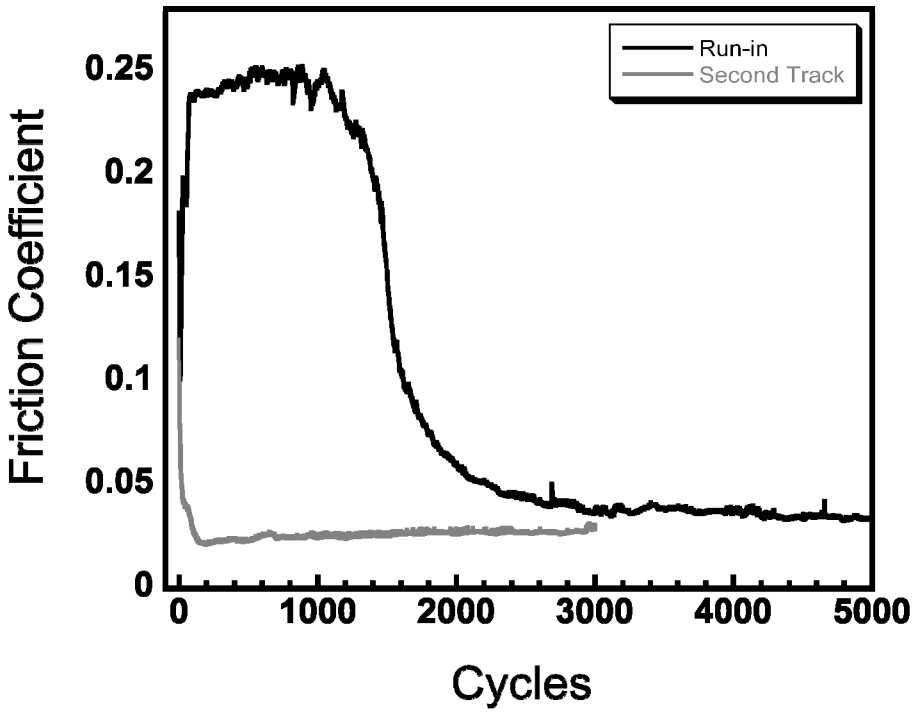

Fig. 5.1: Friction data from run-in track (black line) and for the second track (gray line) made in a new location on the sample.

These friction curves show there is a noticeable effect of conditioning the sphere. The run-in track experiences a longer period of high friction and has a high wear rate, compared to the second track. Smoothing of asperities and chemically conditioning the surface to a stable state are likely most important factors. Both the Si flat and the Si_3N_4 sphere are ~equally smooth substrates, which should mean the surface roughness of the film is likely dominated by the growth itself, and doesn't have a large contribution from the substrate. During the first run-in track, these asperities are being worn away on both surfaces, but what is interesting is that in the second track it seems the effects of any surface roughness of the substrate are negligible. By loading the sphere to the same load, the same spot should be in contact that was worn during the first track. The second track

runs in within 200 cyles, and to a lower friction value than that achieved after 5000 cycles in the run-in track. The friction does trend upward as the second track approaches 3000 cycles, which suggests the contact area of this second track is evolving and that the true contact area is increasing. The profilometry results show that the two tracks have a different height profile. In both cases the wear of the track is low. The run-in track had a maximum depth of ~43 nm inside the gouge, and a single-point wear rate of 3.2×10^{-8} $mm^3N^{-1}m^{-1}$. The second track profile was not distinguishable from the surface roughness of the film.

To examine the chemical conditioning that occurred for these tracks, electron emission images for the sphere and flat include the areas modified by wear as well as areas of unworn material. Fig. 5.2a is an image of the UNCD coated sphere used to make the two tracks highlighted in Fig. 5.3a. Carbon NEXAFS data (Fig. 5.2b) were taken from the scar on the sphere as well as the unworn film. The scar region of interest (ROI) is drawn in Fig. 5.2a. Both spectra have a peak at 285.2 eV that is from a combination of the presence of disordered [5.4] and ordered [5.5, 6] carbon-carbon double bonds. There is an edge jump with an excitonic feature at ~289.3 eV and a dip in intensity at ~302 eV (as discussed in Chapter 2). These features are common to materials with a high fraction of ordered sp^3-bonded carbon, i.e., diamond [5.7]. There is also a feature at ~286.7 eV from C=O bonds [5.8, 9]. The double peak around 292.0 eV is more intense than typical UNCD spectra, and looks like the σ* post-edge features from a highly oriented pyrolitic graphite (HOPG) spectrum [5.6]. The only noticeable differences between the two spectra are the peak heights at ~285.2 eV and ~286.6 eV. The unworn film has more sp^2-

bonded carbon as well as more C=O bonds than the wear scar. The oxygen spectra (Fig. 5.2c) show differences in the level of oxidation. The unworn spectrum has higher peaks at both ~532.6 eV and ~535.4 eV, which are π* features of O=C bonding [5.10].

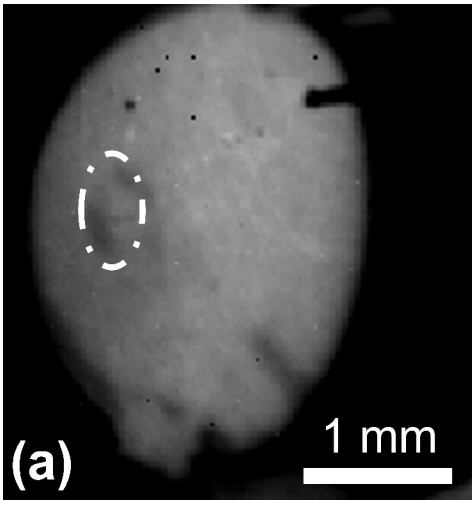

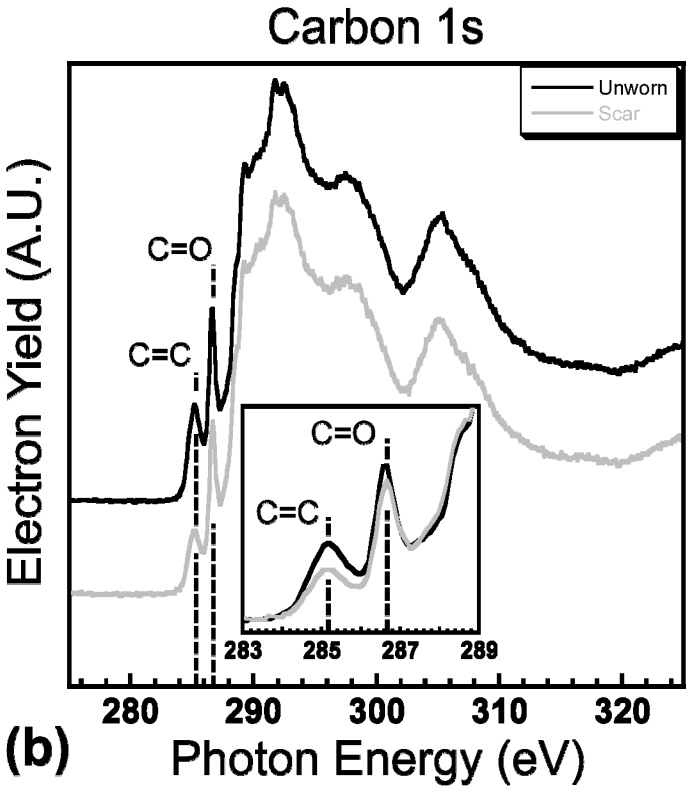

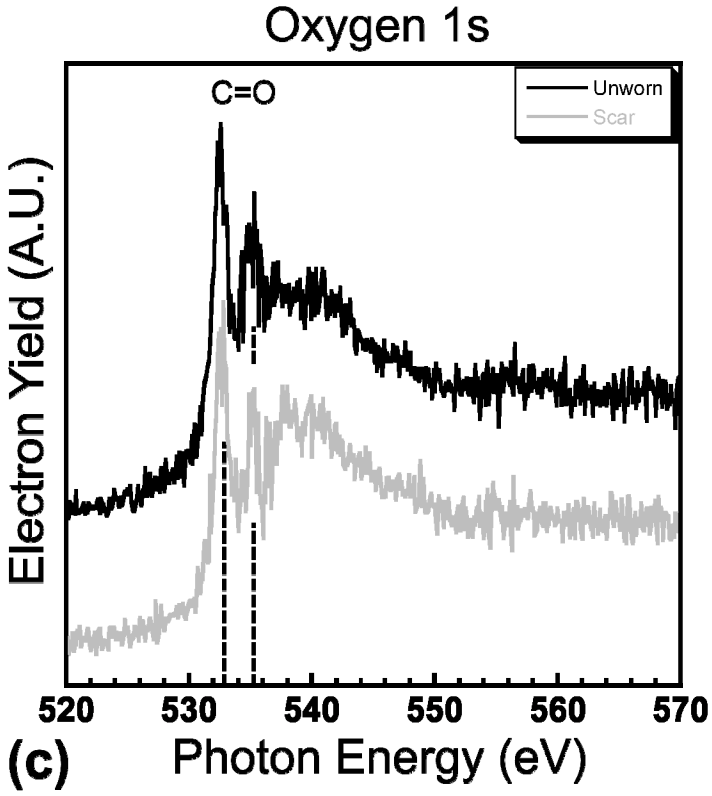

Fig. 5.2: (a) PEY electron emission image of UNCD coated Si_3N_4 sphere; (b) carbon NEXAFS spectra from unworn area (black) and wear scar (gray); (c) oxygen NEXAFS spectra from the same regions.

Fig. 5.3a is a full-field electron image at 289.0 eV of the UNCD flat. The bright stripes are regions that were coated with 40 nm of platinum for a separate study. The dark upper and upper right regions result from the edges of the CCD camera. Four tracks are visible in the image. The carbon NEXAFS data from the two tracks in this study (ROIs labeled in Fig. 5.3a) and an unworn region (not drawn) are in Fig. 5.3b. These spectra have a peak at 285.0 eV that is due to disordered carbon-carbon double bonds [5.4]. The peak at 286.6 eV is from C=O bonding. There is a slight feature in the run-in track and second track at 287.5 eV from C-H bonds. Both the run-in track and the second track have higher C=C concentrations than the unworn area, with the run-in track having the

most. The run-in track also has the highest amount of C=O bonding, whereas the second track actually has less than the unworn area. Fig. 5.3c has O *K*-edge NEXAFS spectra from the same regions from which the C *K*-edge spectra in Fig. 5.3b were taken. All spectra have the same intensity peak at ~533.0 eV from the O=C bonds. There is also a feature at ~535.5 eV that is the higher in the unworn spectrum than the run-in track and second track.

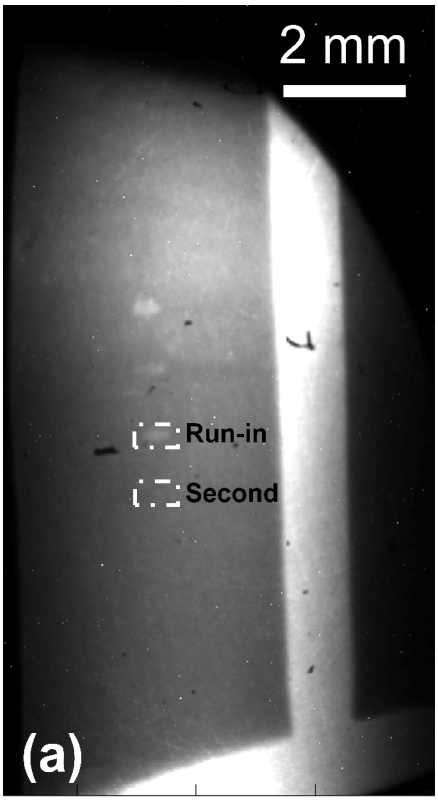

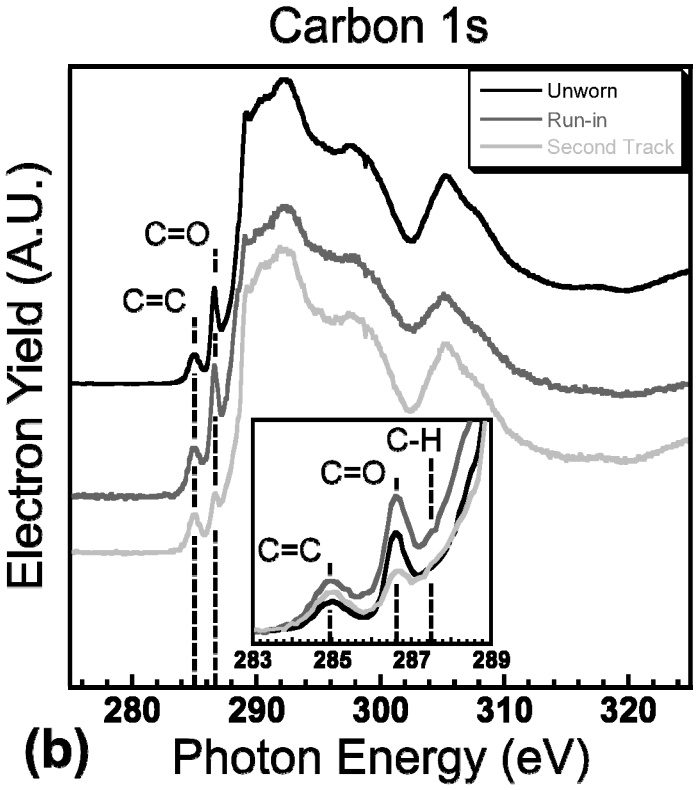
Carbon 1s
Unworn
Run-in
Second Track
C=O
C=C
C-H
C=O
C=C
283
285
287
289
Electron Yield (A.U.)
280
290
300
310
320
(b)
Photon Energy (eV)

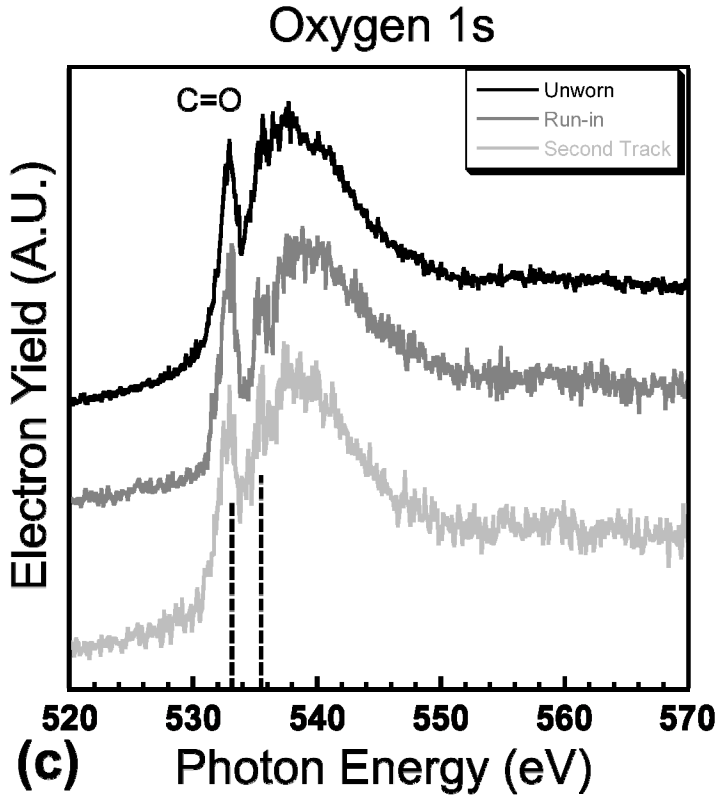

Fig. 5.3: (a) NEXAFS image of UNCD coated silicon flat; (b) carbon NEXAFS spectra from unworn area (black), run-in track (dark gray), and second track (light gray); (c) oxygen NEXAFS spectra from same regions.

The most noticeable observation from the spatially-resolved NEXAFS of the sphere is that the chemical character of the as-grown film differs from that of the as-grown film from the flat. There is the noticeable presence of graphitic carbon on the sphere, shown by the higher energy shift of the C=C π^* peak, and the features around 292.0 eV. Fig. 5.4 shows a hypothetical spectrum that combines 75% of a UNCD NEXAFS spectrum with 25% of an HOPG spectrum. The NEXAFS data from the sphere look similar to this hypothetical spectrum, further supporting that there is a component of graphitic carbon present. The differences obviously come from the large oxygen signal

present on the sphere, as well as a slope difference around the second band gap (302 eV). Note that the two spectra that form the calculated spectrum are from TEY measurements of clean UNCD and HOPG surfaces (almost no oxygen present), and that the PEY surface sensitivity increases the amount of amorphous carbon seen. This is the contribution that changes the slope in the post-edge (black spectrum, Fig. 5.4).

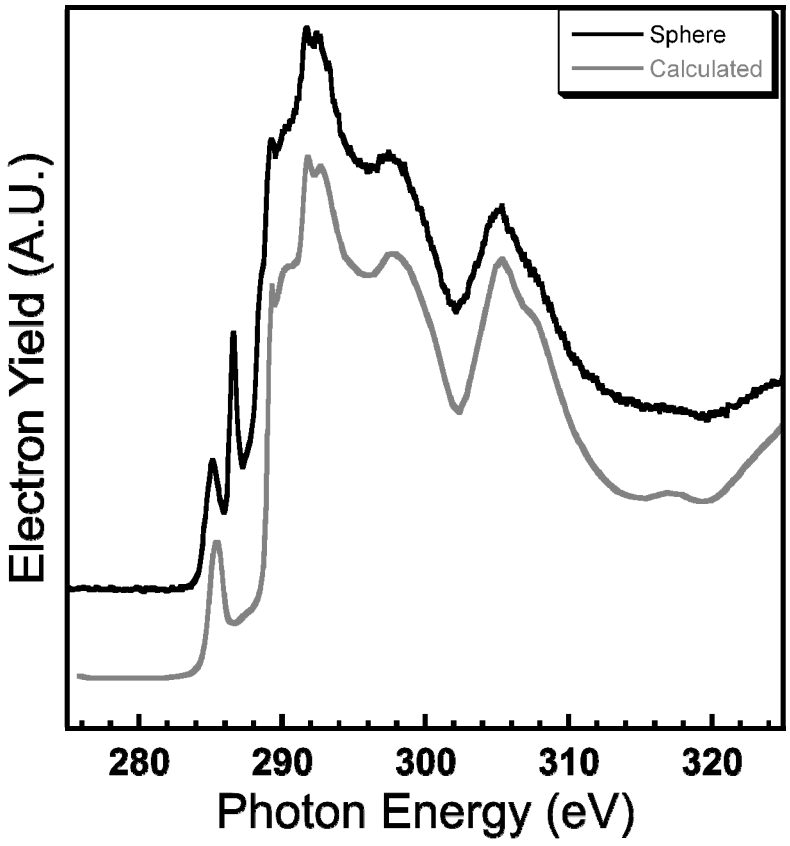

Fig. 5.4: NEXAFS comparison spectra between unworn sphere and calculated spectrum from 75% UNCD and 25% HOPG.

It is possible that the spectral differences from the as-grown flat and sphere are simply from different coating properties due to the different substrate geometries. The samples are all coated in the same run, but the shape of the two substrates means there are

different thermal gradients. Beyond geometry, the average growth temperature was likely different. The thermal conductivity of SiN (0.3 $Wcm^{-1}K^{-1}$) is more than four times less than Si (1.3 W $Wcm^{-1}K^{-1}$). This would explain why the coatings of the two surfaces are likely not identical.

NEXAFS data from the flat (Fig. 5.3b and Fig. 5.3c) show that the run-in track had more amorphous carbon, C=O bonds, and C-H bonds than the unworn film. There is no shift in the C=C peak that would indicate ordered bonding, or graphitization. It is unclear whether the increase in sp^2-bonded carbon is solely from wear of the flat, or whether there is a contribution from debris left on the flat from sphere wear. This shows that the period of high friction broke carbon bonds and those bonds amorphously rehybridized or bonded to species in the environment, most likely water. The increase in amorphous carbon is also evident by the reduction in the second bandgap at 302.0 eV which is caused by the increase of carbon-carbon species with a wider range of bonding lengths. After 2000 cycles, asperities on the sphere are mechanically removed [5.3] and the smooth area inside the contact patch, along with chemical passivation, leads to low friction.

In contrast, the second track ran in immediately and has a lower wear rate. While the state of the sphere at the start of this second track is unknown, the final state (Fig. 5.2b) has less C=C and C=O bonded carbon compared to the unworn film, suggesting a surface layer was removed during sliding. If the surface of the unmodified sphere was representative of the bulk, the changes to the chemistry would only be reflected in increases in the amount of oxygen bonding and C=C bonds. However, the post-wear

spectrum has the same line shape as that of the unworn spectrum, except lower features in the pre-edge. It is possible that there is a surface layer that is more oxidized and is removed during mechanical wear. The O *K*-edge NEXAFS data (Fig. 5.2c) also suggest a surface layer with more oxygen has been removed, as the features at ~532.6 eV and ~535.4 eV are both lower.

Fig. 5.3b shows the C *K*-edge data for the second track. The result of conditioning the sphere first is a more evident removal of the substrate surface layer. The decrease in the C=O peak at ~286.6 eV shows that an oxidized surface layer is removed, likely during the very first few passes of high friction. There is some rehybridization of the sp^3-bonded carbon, but the lack of strong C=O or C-H features suggest few bonds were broken. This is a direct result of smoothing the contact area of the sphere, and then passivating any dangling bonds on the sphere with dissociated water during the first track. The average contact pressure is lower at the beginning of the second track. This, along with the fact that the sphere has already been polished of its highest asperities, means the system has to undergo less wear before steady-state behavior is achieved. Polishing the sphere first highlights how crucial that counterface is to the performance of the pair. It strongly suggests that, if possible, the counterface to a flat in a tribological pairing should always be slightly worn first (at the same point that will make later contact). This will dramatically reduce the friction and wear during sliding.

This also has relevance to the results in Chapter 3 that showed the environment in which these tests are run can control the initial run-in behavior. It is possible that by combining these two results, an optimal conditioning process could be designed to nearly

eliminate wear from run-in. The first step would be to run-in the sphere until the system reached steady-state, but at a high humidity, so that the wear would be minimal while only the highest asperities are worn. Then the sphere could be run against any other portion of the sample and the friction and wear should be minimal.

5.4 Summary

A UNCD-coated sphere made two reciprocating wear tracks on a UNCD-coated flat. The first track took over 2000 cycles to run-in, while the second track, after being polished during the first track, ran in within 200 cycles. The period of higher friction led to measurable wear of the run-in track, while, correspondingly, the immediate run-in and low friction during the second track did not leave a detectable track on the surface.

Spatially resolved NEXAFS data were taken using a newly developed imaging apparatus at the National Synchrotron Light Source, Brookhaven National Laboratory. Data showed that both coatings had evidence of a surface layer that had different chemical properties than the bulk film. Due to the added surface sensitivity of the PEY measurements, it isn't conclusive as to whether it represents an aberrant growth. However, spectra from the sphere show that the as-grown and worn area have largely the same character, which resembles UNCD with a significant fraction of graphitic carbon. The worn portion of the sphere had slightly less sp^2-bonded carbon as well as fewer C=O bonds, after wear removed some of the surface layer. Relative sp^2-bonded carbon fraction increased in the run-in track, as higher amounts of wear either caused rehybridization or left sp^2-bonded debris inside the worn region. However, the second wear track that experienced low friction and low wear had a NEXAFS spectrum with a much reduced

C=O bonding intensity, along with a slight increase in the C 1s→π* intensity. This showed that only minimal bonds were broken while making this track, and those likely removed the oxygen from the surface, causing the dangling carbon bonds to rehybridize in the process.

An important lesson learned from this study is that the chemistry of the sphere need not always be identical to the flat. Diamond growth is very sensitive to temperature. There are thermal gradients in the growth area that can be controlled and tuned to improve the uniformity of coatings over wafers. But these systems are not optimized for 3D geometries (*e.g.* spheres). There is no spectroscopy technique like NEXAFS that can give such an accurate, qualitative measure of the bonding quality of a diamond film. However, due to the fact that a synchrotron is needed to perform these measurements, this is not always feasible. Regardless, this needs to be considered when performing tests with self-mated, polycrystalline diamond interfaces.

5.5 Chapter 5 References

[5.1] A. V. Sumant, O. Auciello, H. C. Yuan, Z. Ma, R. W. Carpick, and D. C. Mancini, (SPIE - The International Society for Optical Engineering, USA, 2009), p. 731817 (7 pp.).
[5.2] A. V. Sumant, D. S. Grierson, J. E. Gerbi, J. Birrell, U. D. Lanke, O. Auciello, J. A. Carlisle, and R. W. Carpick, Advanced Materials **17**, 1039 (2005).
[5.3] I. P. Hayward, I. L. Singer, and L. E. Seitzman, Wear **157**, 215 (1992).
[5.4] R. Gago, M. Vinnichenko, H. U. Jager, A. Y. Belov, I. Jimenez, N. Huang, H. Sun, and M. F. Maitz, Physical Review B (Condensed Matter and Materials Physics) **72**, 14120 (2005).
[5.5] R. Gago, I. Jimenez, and J. M. Albella, (Elsevier, Netherlands, 2001), pp. 530.
[5.6] S. Osswald, G. Yushin, V. Mochalin, S. O. Kucheyev, and Y. Gogotsi, Journal of the American Chemical Society **128**, 11635 (2006).
[5.7] F. L. Coffman, R. Cao, P. A. Pianetta, S. Kapoor, M. Kelly, and L. J. Terminello, Applied Physics Letters **69**, 568 (1996).
[5.8] J. Stöhr, *NEXAFS spectroscopy* (Springer-Verlag, Berlin; New York, 1992).
[5.9] M. Jaouen, G. Tourillon, J. Delafond, N. Junqua, and G. Hug, Diamond and Related Materials **4**, 200 (1995).
[5.10] I. Ishii, and A. P. Hitchcock, Journal of Electron Spectroscopy and Related Phenomena **46**, 55 (1988).

6. Conclusions

6.1 Broader Experimental Impact

The work in this thesis depends on a carefully developed series of experimental steps necessary to measure and correlate tribological phenomena with surface chemical changes for these hydrogen free, hard carbon films. One important benefit is that this protocol is applicable to a much wider range of materials. Recent investigations of surfaces exposed to tribological contact in a silicon-based MEMS device [6.1], and studies of silicon nitride in contact with UNCD [6.2] are examples of such applications.

The important components center around the tribometer experiments and subsequent PEEM measurements. Tribometry with the level of environmental control and measurement precision attained here is not simple. For the work in this thesis, positional friction measurements are made with micron-scale precision, and the relative humidity is controlled and measured to within 0.1%. This improves the reliability and reproducibility of the experiments. Working with advanced tribometers and controlled experimental conditions ensures that tests can be performed and phenomena observed, but that the samples will be usable for later measurements. Analyzing chemical changes with PEEM has been the other key component to this work. No other technique can achieve the same combination of spatial resolution, atomic composition sensitivity, and chemical bonding sensitivity, while being non-destructive, relatively high throughput, and working on a microscopic level that matches the scale of the tribometry. This has been especially

fruitful for carbon, since other techniques are not as surface sensitive, or sensitive to the subtle bonding changes, that happen at the interface during tribochemical modification. There have been other studies that have studied tribological problems using PEEM [6.1-9], with most of them focusing on antiwear films formed from oil with ZDDP additive. This thesis describes the most in-depth study of a tribological problem by combining tribometry and PEEM, along with other characterization methods.

6.2 Results Summary

This thesis has presented studies of the wear mechanisms of nearly hydrogen free, hard carbon thin films. A main conclusion is that passivation, and not graphitization, is responsible for the low friction and low wear of these materials under a wide range of conditions. In a self-mated diamond tribological contact where there are shear stresses and thermal gradients in a contact, it is not unreasonable to hypothesize that graphitic carbon could be formed. At higher RH, these two surfaces could weakly interact and would therefore have low friction and wear, much like graphite itself. At lower RH, graphite is known to be a poor lubricant. The formation of graphite during sliding would create debris and increase friction and wear. However, no evidence of any graphitization was observed in any study performed with UNCD or ta-C interfaces. There was some degree of rehybridization in the form of amorphous carbon with elevated sp^2 content found for wear tracks that experienced periods of high friction and had more wear. However, this amorphized surface still did not lubricate the interface at low RH, and is not the mechanism for low friction.

All evidence points toward passivation, specifically by the dissociation of water into hydrogen and hydroxyl groups. At high RH, and all loads tested, ta-C and UNCD experience a short run-in period followed by low friction. This coincides with extremely low wear, which in some cases is nearly immeasurable using optical profilometry techniques. The evidence suggests that the little wear that might occur due to asperities being polished is quickly followed by the broken bonds being passivated by dissociated water. This leads only to mild oxidation of the surface. At low RH, and especially higher loads, these films experience high friction and wear. As broken bonds are formed there are not enough passivating species to fully saturate the surface, and the bonds on both surfaces strongly interact, leading to high friction and wear. Bond breaking is seen to be a strong function of apparent contact pressure. If enough wear of the sphere occurs, then at a fixed load the contact pressure decreases, causing fewer bonds to be broken per sliding pass. This was seen for UNCD in Chapter 3 where the high load, low RH test eventually did run in to low friction, but only after the wear track dimensions had significantly increased.

The number of run-in cycles is determined by the availability of the passivating vapor species, which further demonstrates that the rates of water adsorption and dissociation (further discussed in Chapter 4) compete with the rates of bond breaking and trans-interfacial bond formation. Higher RH and longer exposure times enable more complete passivation, decreasing the time the system takes to reach steady-state. In order to quickly achieve low friction, and therefore have minimal wear from run-in, the system requires a sufficient RH level for a given initial load (contact pressure).

The balance between bond breaking and passivation also leads to the switching phenomenon for UNCD (discussed in Chapter 4). The critical factor here involves the relationship between water adsorption and dissociation on a surface and the energy barrier to further adsorb and passivate. Since, according to DFT calculations, the energy barriers significantly decrease for both adsorption and dissociation with some water already present, a tribological bimodality exists. In the low friction case, there is a sufficient RH level for water to adsorb and then dissociatively passivate the dangling bonds formed during sliding, given an already high level of water on the surface. This situation persists until the RH is dropped below a critical threshold. Then the number of bonds broken, even if kept constant, cannot be passivated rapidly enough by the available water species. There is a combination of two effects: too many unpassivated species, and an increase in the energy barriers required to adsorb and to dissociate water. When this occurs, the friction transitions to the high state, and at this point the contacting points on the surface are not passivated and strongly interact.

This process is reversible, but hysteretic, requiring a higher RH to recover than the level at which the high friction transition occurred. The available water before the high friction transition was sufficient because of the presence of water on the surface. After the transition there is less water already adsorbed, and with the higher energy barriers to adsorb, a higher RH level is needed to kinetically drive the reaction and thus to begin replenishing the surface with dissociated water. After the RH is increased above this threshold, the passivation happens rather rapidly. Assisted by the positive feedback resulting from adsorption-induced lowering of the barriers, areas of water adsorption

grow, and water further adsorbs, diffuses, dissociates, and passivates dangling bonds. This prevents bonding across the interface and quickly reduces the friction.

The main result from the experiments using the new imaging apparatus at the National Synchrotron Light Source is the success in full-field imaging, with image depth and contrast, of both the sphere and flat that made a tribological contact. The NEXAFS data acquired showed that while the initial state of the coatings on the sphere and flat were different, the surfaces evolved to similar final states. The added surface sensitivity of the PEY measurements showed the removal of a top surface layer from both materials due to sliding. Running in the sphere on one area of the flat caused rehybridization and oxidation on the flat wear track. However, a second track made with the polished sphere had little chemical change and barely any wear. This shows that run-in causes the most wear and chemical modification for these interfaces.

An interesting point to consider concerns reducing this run-in phase. Since this phase is where the most wear, and therefore debris, comes from, reducing it could enable devices that can not tolerate debris particles normally to otherwise function. In Chapter 3 it was observed that changing the RH level in the environment controlled the number of cycles of run-in. In Chapter 4 several examples were shown where a sphere was run in at higher humidity, and then the RH was decreased substantially while still maintaining low friction (until the RH was below a critical threshold). This suggests that devices could be operated in lower humidities (~2%), but first run in at a higher humidity. By performing this initial step, the surface conditioning happens in a higher RH environment, and then actual use can occur at lower RH without the debris and increased friction during run-in.

Alternatively, growing films that are even smoother (which also requires the substrate to be sufficiently smooth to begin with) could dramatically reduce the run-in and thus the overall wear.

A second point to consider concerns the switching behavior seen for UNCD. This sharp transition would be interesting for a humidity sensing application. By setting the correct load and exposure time, the friction performance of a self-mated UNCD contact could be used as a trigger to indicate changes in the chemical environment beyond a certain threshold value.

Finally, the results suggest that the pathway to reducing the environmental limits of ultra-hard carbon-based films may be through combining the excellent properties that have been measured in this thesis, and the range of environments and loads shown, with other materials. Voevodin *et al.* have created so-called 'chameleon' coatings that are able to adapt their friction and wear behavior for both dry and humid environments [6.10], as well as for changing temperatures [6.11]. It is possible that ta-C or UNCD coatings could become a component of a multi-phase coating where the carbon component could be responsible for extremely low friction and wear for RH levels between 2.5% and 100%, and at contact pressures in the hundreds of MPa. The other components would need to be responsible for vacuum conditions, or inert environments below 1.0% RH.

6.3 Future Work

There are still interesting avenues of study to more completely understand the tribological behavior of these materials. For example, there are further experiments that could better verify the conclusions drawn in Chapter 3. The first such experiment would

be to create reference samples of UNCD and ta-C that are terminated with known chemical species (*e.g.*, hydrogen, hydroxyl, or ester groups) and then measure the NEXAFS spectra for these different sample terminations. This is required because most of the literature on NEXAFS reference spectra come from molecules in the gas state. Each molecule has slightly different transition energies, even for similar bonds (*e.g.*, a C-C bond for ethane is at 290.8 eV, but the C-C bond in propane is 291.6 eV [6.12]). By intentionally terminating these carbon films with various species, the NEXAFS references would, ideally, directly correlate with the spectra seen for worn surfaces.

Another series of measurements would involve using the new PEEM3 at the Advanced Light Source. PEEM3 has only been brought online in the last two years. Some advantages over PEEM2 (the instrument used for all PEEM measurements in this thesis) include higher spatial resolution as well as the ability to cool or heat the sample over a much wider temperature range. An added feature of the beamline PEEM3 resides at is the ability to have linearly polarized light and to change the angle of polarization in the plane of the electric and magnetic field vectors. Unfortunately, due to the fixed orientation of the sample and the fixed angle of incidence of the photons on the sample, it is not possible to change the angle between the light and the sample normal. However, the fixed polarization of the linearly polarized light at PEEM2 (polarization field vector parallel to the sample surface) makes it impossible to strongly excite molecular orbitals that are perpendicular to the surface. By rotating the polarization of the light from more parallel to more perpendicular to the sample surface, information about the bond

orientation can be obtained. This would lead to more conclusive evidence about the specific type of termination for the worn surfaces.

While such further work would certainly be beneficial, the new conclusions drawn from this thesis demonstrate convincingly that the tribological behavior of ultra-strong, hydrogen-free, carbon-based films is strongly coupled to surface chemical processes. With this knowledge in hand, these materials can be better designed for and implemented in tribological applications. A better scientific understanding of environmental effects in tribological contacts in general can emerge.

6.4 Chapter 6 References

[6.1] D. S. Grierson, A. R. Konicek, G. E. Wabiszewski, A. V. Sumant, M. P. De Boer, A. D. Corwin, and R. W. Carpick, Tribology Letters **36**, 233 (2009).
[6.2] D. S. Grierson *et al.*, Journal of Vacuum Science and Technology B: Microelectronics and Nanometer Structures **25**, 1700 (2007).
[6.3] E. L. Montei, and M. E. Kordesch, Journal of Vacuum Science and Technology A: Vacuum, Surfaces and Films **15**, 1173 (1997).
[6.4] S. Anders, T. Stammler, W. Fong, C.-Y. Chen, D. B. Bogy, C. S. Bhatia, and J. Stohr, Journal of Tribology **121**, 961 (1999).
[6.5] X. H. Zhang, R. S. Gates, S. Anders, and S. M. Hsu, Tribology Letters **11**, 15 (2001).
[6.6] M. N. Najman, M. Kasrai, G. M. Bancroft, B. H. Frazer, and G. De Stasio, (Kluwer Academic/Plenum Publishers, USA, 2004), pp. 811.
[6.7] M. A. Nicholls, G. M. Bancroft, M. Kasrai, P. R. Norton, B. H. Frazer, and G. De Stasio, Tribology Letters **18**, 453 (2005).
[6.8] G. Pereira, A. Lachenwitzer, M. A. Nicholls, M. Kasrai, P. R. Norton, and G. De Stasio, Tribology Letters **18**, 411 (2005).
[6.9] A. R. Konicek, D. S. Grierson, P. U. P. A. Gilbert, W. G. Sawyer, A. V. Sumant, and R. W. Carpick, Physical Review Letters **100**, 235502 (2008).
[6.10] A. A. Voevodin, and J. S. Zabinski, Thin Solid Films **370**, 223 (2000).
[6.11] C. Muratore, A. A. Voevodin, J. J. Hu, J. G. Jones, and J. S. Zabinski, Surface and Coatings Technology **200**, 1549 (2005).
[6.12] A. P. Hitchcock, and I. Ishii, Journal of Electron Spectroscopy and Related Phenomena **42**, 11 (1987).

7. Appendix

7.1 Publications

Thermal stability and rehybridization of carbon bonding in tetrahedral amorphous carbon
D. S. Grierson, A. V. Sumant, A. R. Konicek, T. A. Friedmann, J. P. Sullivan, and R. W. Carpick
Physical Review B, Vol. 107, No. 3, 2010, p. 033523-8

Characterization of microscale wear in a polysilicon-based MEMS device using AFM and PEEM-NEXAFS spectromicroscopy
D. S. Grierson, A. R. Konicek, G. E. Wabiszewski, A.V. Sumant, M. P. de Boer, A. D. Corwin, and R. W. Carpick
Tribology Letters, Vol. 36, No. 3, 2009, p. 233-238

Origin of ultralow friction and wear in ultrananocrystalline diamond
A. R. Konicek, D. S. Grierson, P.U.P.A. Gilbert, W. G. Sawyer, A. V. Sumant, and R. W. Carpick
Physical Review Letters, Vol. 100, No. 23, 2008, p. 235502/1-4

Synthesis and characterization of smooth ultrananocrystalline diamond films via low pressure bias-enhanced nucleation and growth
Y. C. Chen, X. Y. Zhong, A. R. Konicek, D. S. Grierson, N. H. Tai, I. N. Lin, B. Kabius, J. M. Hiller, A. V. Sumant, R. W. Carpick, and O. Auciello
Applied Physics Letters, Vol. 92, No. 13, 2008, p. 133113/1-3

Tribochemistry and material transfer for the ultrananocrystalline diamond-silicon nitride interface by X-PEEM spectromicroscopy
D. S. Grierson, A. V. Sumant, A. R. Konicek, M. Abrecht, J. Birrell, O. Auciello, J. A. Carlisle, T. W. Scharf, M. T. Dugger, P.U.P.A. Gilbert, and R. W. Carpick
Journal of Vacuum Science and Technology B: Microelectronics and Nanometer Structures, Vol. 25, No. 5, 2007, p. 1700-1705

Surface composition, bonding, and morphology in the nucleation and growth of ultra-thin, high quality nanocrystalline diamond films
A. V. Sumant, P.U.P.A. Gilbert, D. S. Grierson, A. R. Konicek, M. Abrecht, J. E. Butler, T. Feygelson, S. S. Rotter, and R. W. Carpick
Diamond & Related Materials, Vol. 16, No. 4-7, 2007, p. 718-724

Electron-phonon interaction at the Si(111)-7x7 surface
I. Barke, F. Zheng, A. R. Konicek, R. C. Hatch, and F. J. Himpsel
Physical Review Letters, Vol. 96, No. 21, 2006, p. 216801/1-4

7.2 Analysis Code

7.2.1 Profilometry Analysis

```
[filename, pathname] = uigetfile({'*.asc';'*.txt'}, 'Pick a txt-file');
% User selects .asc or .txt file containing topographic data with wear
track

fullname = strcat(pathname, filename);
[A, x_range, y_range, I] = heightHeaderLoad(fullname);
[y,x] = size(A);
dX = x_range/x;
dY = y_range/y;
% Load data file, find the size, calculate the pixel size from the
header information

fit_fig1 = figure;
if viewSelect == 1
    surf(A);
else
    surf(I);
    colormap('gray');
end
shading interp;
title('Left click 4 points that encompass the wear track.');
xlabel('X pixels');
ylabel('Y pixels');
view(0,90)
xlim([0 x])
ylim([0 y])
axis equal;
axis off;
[a,b,but] = ginput(4);
xy = [a,b];
negs = find(xy < 1);
xy(negs) = 1;
beyondx = find(xy(:,1) > x);
xy(beyondx,1) = x;
beyondy = find(xy(:,2) > y);
xy(beyondy,2) = y;
minx = round(min(xy(:,1)));
maxx = round(max(xy(:,1)));
miny = round(min(xy(:,2)));
maxy = round(max(xy(:,2)));
close(fit_fig1)
% Plot the data and select a rectangle around the track to exclude the
% track from the plane fit
```

```
tempA = A;
tempA(miny:maxy,minx:maxx) = NaN;
tempA_remove = tempA(:);
includePoints = find(~isnan(tempA_remove));
tempA_remove = tempA_remove(includePoints);
[X,Y] = meshgrid((1:x),(1:y));
X2 = X(:);
Y2 = Y(:);
B = [X2(includePoints),Y2(includePoints),
X2(includePoints).*Y2(includePoints),ones(length(X(includePoints)),1)];
p = (B'*B)\(B'*tempA_remove);
A = A - (p(1)*X + p(2)*Y + p(3)*X.*Y + p(4));
% Plane fit the data

A2 = A;
NaN_loc = find(isnan(A2));
A2(NaN_loc) = 0;
mat_avg = mean(mean(A2));
mat_rms = sqrt(mean(mean((A2-mat_avg).^2)));
too_high = A>3*mat_rms;
too_low = A<-3*mat_rms;
too_nan = isnan(A);
Flagpoints = too_high + too_low + too_nan;
% Flag errant data

while sum(sum(Flagpoints))~=0
    for p = 1:y
        for q = 1:x
            if Flagpoints(p, q) == 1
                r = zeros(1, 1);
                s = zeros(1, 1);
                DD = 0;
                row_ok = 1;
                start_ind = q-1;
                if start_ind < 1
                    start_ind = 1;
                end
                final_ind = q-round(0.05*x);
                if final_ind<1
                    final_ind = 1;
                end
                for a = start_ind:-1:final_ind
                    if Flagpoints(p,a) == 0
                        DD = DD + 1;
                        r(DD) = a;
                        s(DD) = A3(p, a);
                    end
                end
                start_ind = q+1;
                if start_ind > x
                    start_ind = x;
                end
                final_ind = q+round(0.05*x);
                if final_ind > x
                    final_ind = x;
```

```
end
for b = start_ind:final_ind
    if Flagpoints(p, b) == 0
        DD = DD + 1;
        r(DD) = b;
        s(DD) = A3(p, b);
    end
end
if length(r)>=round(0.05*x)
    Xrun = mean(s);
else
    row_ok = 0;
end
r = zeros(1, 1);
s = zeros(1, 1);
EE = 0;
col_ok = 1;
start_ind = p-1;
if start_ind < 1
    start_ind = 1;
end
final_ind = p-round(0.05*y);
if final_ind<1
    final_ind = 1;
end
for left = start_ind:-1:final_ind
    if Flagpoints(left,q) == 0
        EE = EE + 1;
        r(EE) = left;
        s(EE) = A3(left, q);
    end
end
start_ind = p+1;
if start_ind > y
    start_ind = y;
end
final_ind = p+round(0.05*y);
if final_ind > y
    final_ind = y;
end
for right = start_ind:final_ind
    if Flagpoints(right, q) == 0
        EE = EE + 1;
        r(EE) = right;
        s(EE) = A3(right, q);
    end
end
if length(r)>=round(0.05*y)
    Yrun = mean(s);
else
    col_ok = 0;
end
if row_ok == 1 & col_ok == 1
    A3(p,q) = (Xrun+Yrun)/2;
    Flagpoints(p,q) = 0;
```

```
                end
            end
        end
    end
end
A = A3;
% Interpolate flagged data points by spline fitting trusted data

z_trunc = A(miny:maxy,minx:maxx);
distance = 2 * sliplength * cycles / 1000000;
Truevolumeremoved = 0;
Truedebrisvolume = 0;
Truewearrate = 0;
Depthsum = 0;
Depthsumsquared = 0;
Maxdepth = 0;
above_plane = z_trunc>0;
below_plane = z_trunc<0;
Truevolumeremoved = abs(sum(sum(z_trunc(below_plane)))*dX*dY/(1000^4));
Truedebrisvolume = abs(sum(sum(z_trunc(above_plane)))*dX*dY/(1000^4));
Maxdepth = min(min(z(miny:maxy,minx:maxx)));
Averagedepth = mean(mean(z_trunc(below_plane)));
Avg_depth_str = num2str(Averagedepth, 7);
Avg_depth_cat = ['Average depth = ', Avg_depth_str, ' nm'];
Max_depth_str = num2str(Maxdepth, 7);
Max_depth_cat = ['Maximum depth = ', Max_depth_str, ' nm'];
RMS = (mean(mean(z(miny:maxy,minx:maxx).^2)))^0.5;
RMS_str = num2str(RMS, 7);
RMS_cat = ['RMS = ', RMS_str, ' nm'];
Truevolumeremoved_str = num2str(Truevolumeremoved, 7);
Truevolumeremoved_cat = ['True volume removed = ',
Truevolumeremoved_str, ' mm^3'];
Truedebrisvolume_str = num2str(Truedebrisvolume);
Truedebrisvolume_cat = ['True debris volume = ', Truedebrisvolume_str,
' mm^3'];
Truewearrate = Truevolumeremoved / (load * distance);
Truewearrate_str = num2str(Truewearrate, 7);
Truewearrate_cat = ['True wear rate = ', Truewearrate_str, '
mm^3/N*m'];
Wear_results = char(Avg_depth_cat , Max_depth_cat , RMS_cat ,...
    Truevolumeremoved_cat , Truewearrate_cat, Truedebrisvolume_cat)
% Calculate the volume removed, debris volume, maximum depth, average
% depth, and wear rate from the data
```

7.2.2 Spectroscopy Analysis

```
[filename, pathname] = uigetfile({'*.dat;*.txt', 'Spectrum Files
(*.dat,*.txt)'}, 'Pick a data file');

% Loads the pathname containing the data to be analyzed. It is
understood the files are listed alphabetically, and, pair-wise, in the
order of the data file and then the normalization file.
```

```
% The following boolean variables are '1' for yes/do/on or '0' for
% no/don't/off unless otherwise specified
film_bool = 1; % Boolean variable for film type, 1 for UNCD, 0 for ta-C
stack_save_bool = 1;
sep_save_bool = 1;
stndv_save_bool = 1;
% Boolean variables controlling whether processed data is saved
linfit_bool = 1; % Boolean variable for whether to perform linear fit
on data

dat_files = dir(fullfile(pathname, '\*.dat'));
% Search the pathname for all .dat files (file format for NEXAFS data)

if (stack_save_bool == 1) || (sep_save_bool == 1) || (stndv_save_bool
== 1)
    try
        warning off
        mkdir([pathname, '\Saved Spectra'])
    catch
    end
end

for j = 1:(length(dat_files)/2)
    sample_file_name = [pathname, dat_files(2*j-1).name];
    I0_file_name = [pathname, dat_files(2*j).name];

    E = loadWithHeader(sample_file_name);
    F = loadWithHeader(I0_file_name);
    % Loads sample and I0 file, pair-wise
    [G] = smooth(F);
    % Smooths I0 spectrum (should be fine since no I0 has a sharp
feature)

    [C, L1, L2] = interpolate(E);
    [D] = interpolate(G);
    % Interpolate data and I0

    X = zeros(L1,L2);
    X(:,1) = C(:,1);
    % Zero matrix to the size of the incoming data, and set first
column to be the energy column from the interpolated data matrix

    [not_used, index1] = findValInd(X, X(1,1));
    [not_used, index2] = findValInd(X, X(1,1)+2.5);
    C_avg = repmat(mean(C(index1:index2,2:L2)),L1,1);
    D_avg = repmat(mean(D(index1:index2,2:L2)),L1,1);
    X(:,2:L2) = (C(:,2:L2)./C_avg)./(D(:,2:L2)./D_avg)-1;
    % First find the start and end indeces of the first 2.5 eV worth of
data. Create two replicated matrices, one for data and one for I0, of
their respective mean values between the found indeces. Normalize the
data by taking the data divided by its mean, and dividing that by the
I0 divided by its mean.

    if X(1,1) < 285 && film_bool == 1
```

```
        [not_used, xyz] = findValInd(X, max(X(:,2))/2, 2);
        X(:,1) = X(:,1) - X(xyz,1) + 289;
    elseif X(1,1) < 285 && film_bool == 2
        [mid_index, real_peak_pos] = piMaxMinFind(X);
        X(:,1) = X(:,1) - X(real_peak_pos,1) + 285;
    end
    % Correct the energy axis of every spectrum using the location of
the edge-jump for UNCD and the location of the pi* peak for ta-C.

    U = X; % First matrix that will store the as-normalized data

    if linfit_bool == 1
        if 260 < X(1,1) && X(1,1) < 285
            [not_used, index1] = findValInd(X, 277);
            [not_used, index2] = findValInd(X, 282);
            V = X;
            for i = 2:L2
                preedgelinfitparam(:,i-1) =
polyFitPlus(X(index1:index2,1), X(index1:index2,i), 1);
                V(:,i) = X(:,i) - (preedgelinfitparam(1,i-1)*X(:,1) +
preedgelinfitparam(2,i-1));
            end
            X = V;
            if X(L1,1) < 320
                E1 = L1;
            else
                [not_used, E1] = findValInd(X,320);
            end
        elseif 335 < X(1,1) && X(1,1) < 345
            [not_used, index1] = findValInd(X, X(1,1)+1);
            [not_used, index2] = findValInd(X, X(1,1)+5);
            V = X;
            for i = 2:L2
                preedgelinfitparam(:,i-1) =
polyFitPlus(X(index1:index2,1), X(index1:index2,i), 1);
                V(:,i) = X(:,i) - (preedgelinfitparam(1,i-1)*X(:,1) +
preedgelinfitparam(2,i-1));
            end
            X = V;
            [not_used, E1] = findValInd(X,X(end,1)-2);
        elseif 380 < X(1,1) && X(1,1) < 400
            [not_used, index1] = findValInd(X, X(1,1)+2);
            [not_used, index2] = findValInd(X, 395);
            V = X;
            for i = 2:L2
                preedgelinfitparam(:,i-1) =
polyFitPlus(X(index1:index2,1), X(index1:index2,i), 1);
                V(:,i) = X(:,i) - (preedgelinfitparam(1,i-1)*X(:,1) +
preedgelinfitparam(2,i-1));
            end
            X = V;
            [not_used, E1] = findValInd(X,X(end,1)-2);
        elseif 500 < X(1,1) && X(1,1) < 540
            [not_used, index1] = findValInd(X, 522);
            [not_used, index2] = findValInd(X, 527);
```

```
            V = X;
            for i = 2:L2
                preedgelinfitparam(:,i-1) =
polyFitPlus(X(index1:index2,1), X(index1:index2,i), 1);
                V(:,i) = X(:,i) - (preedgelinfitparam(1,i-1)*X(:,1) +
preedgelinfitparam(2,i-1));
                V(:,i) = V(:,i) - min(V(:,i));
            end
            X = V;
            [not_used, E1] = findValInd(X,X(end,1)-2);
        elseif 690 < X(1,1) && X(1,1) < 710
            [not_used, index1] = findValInd(X, 702);
            [not_used, index2] = findValInd(X, 708);
            V = X;
            for i = 2:L2
                preedgelinfitparam(:,i-1) =
polyFitPlus(X(index1:index2,1), X(index1:index2,i), 1);
                V(:,i) = X(:,i) - (preedgelinfitparam(1,i-1)*X(:,1) +
preedgelinfitparam(2,i-1));
            end
            X = V;
            [not_used, E1] = findValInd(X,X(end,1)-2);
        elseif 1010 < X(1,1) && X(1,1) < 1030
            [not_used, index1] = findValInd(X, X(1,1)+1);
            [not_used, index2] = findValInd(X, X(1,1)+8);
            V = X;
            for i = 2:L2
                preedgelinfitparam(:,i-1) =
polyFitPlus(X(index1:index2,1), X(index1:index2,i), 1);
                V(:,i) = X(:,i) - (preedgelinfitparam(1,i-1)*X(:,1) +
preedgelinfitparam(2,i-1));
                V(:,i) = V(:,i) - min(V(:,i));
            end
            X = V;
            [not_used, E1] = findValInd(X,X(end,1)-2);
        elseif 1045 < X(1,1) && X(1,1) < 1055
            [not_used, index1] = findValInd(X, X(1,1)+3);
            [not_used, index2] = findValInd(X, X(1,1)+10);
            V = X;
            for i = 2:L2
                preedgelinfitparam(:,i-1) =
polyFitPlus(X(index1:index2,1), X(index1:index2,i), 1);
                V(:,i) = X(:,i) - (preedgelinfitparam(1,i-1)*X(:,1) +
preedgelinfitparam(2,i-1));
                V(:,i) = V(:,i) - min(V(:,i));
            end
            X = V;
            [not_used, E1] = findValInd(X,X(end,1)-2);
        end
    end
    % If the boolean variable for linear fit is true, perform a linear
fit on the data from the flat portion in the pre-edge of each spectrum,
and then subtracting that fit from the whole spectrum.
```

```
    W = X; % Second matrix that will store the normalized and linear
fit data
    Y = X; % Third matrix that will store the normalized, linear fit,
and post-edge divided data
    Z = X; % Fourth matrix that will store the normalized, linear fit,
post-edge divided, and separated data

    if linfit_bool == 1
        for i = 2:L2
            if (abs(X(E1,2:L2)) == X(E1,2:L2)) && E1 > 0
                diviSOR = X(E1,i);
            else
                diviSOR = 1;
            end
            if i == 2
                Y(:,i) = X(:,i)./diviSOR;
                Z(:,i) = Y(:,i);
            else
                Y(:,i) = X(:,i)./diviSOR;
                MinColumnBefore = min(Z(:,i-1));
                Z(:,i) = (X(:,i))./(diviSOR);
                MaxColumnCurrent = max(Z(:,i));
                if X(1,1) < 285 && film_bool == 1
                    Z(:,i) = (X(:,i))./(diviSOR) + MinColumnBefore -
0.7 * MaxColumnCurrent;
                elseif X(1,1) < 285 && film_bool == 0
                    Z(:,i) = (X(:,i))./(diviSOR) + MinColumnBefore -
0.3 * MaxColumnCurrent;
                else
                    Z(:,i) = (X(:,i))./(diviSOR) + MinColumnBefore -
0.75 * MaxColumnCurrent;
                end
            end
        end
    end
    % Section that performs the data manipulation as described above

    NoLinNoDivStackData = U;
    LinNoDivStackData = W;
    LinDivStackData = Y;
    LinDivSepData = Z;

    if (stack_save_bool == 1) || (sep_save_bool == 1) ||
(stndv_save_bool == 1)
        F = ['%5.8f '];
        for i = 1:(L2-2)
            F = [F,'%5.8f '];
        end
        F = [F, '%5.8f\r'];
        label = [('Energy_(eV)')];
        for i = 1:(L2-1)
            num=num2str(i);
            label= [label, ' data',num];
        end
```

```
        newfile1 = regexprep(dat_files(2*j-1).name, '.dat', '_',
'ignorecase');
        if stndv_save_bool == 1
            normfile_name_NoLinStackNoDiv = [pathname, 'Saved
Spectra\', newfile1, 'norm_', 'NoLinStackNoDiv.dat'];
            [fid0, message] = fopen(normfile_name_NoLinStackNoDiv,
'w');
            fprintf(fid0,'%s\r',label);
            fprintf(fid0, F, NoLinNoDivStackData');
            fclose(fid0);

            normfile_name_StackNoDiv = [pathname, 'Saved Spectra\',
newfile1, 'norm_', 'StackNoDiv.dat'];
            [fid1, message] = fopen(normfile_name_StackNoDiv, 'w');
            fprintf(fid1,'%s\r',label);
            fprintf(fid1, F, LinNoDivStackData');
            fclose(fid1);
        end
        if stack_save_bool == 1
            normfile_name_Stacked = [pathname, 'Saved Spectra\',
newfile1, 'norm_', 'Stacked.dat'];
            fid2 = fopen(normfile_name_Stacked, 'w');
            fprintf(fid2,'%s\r',label);
            fprintf(fid2, F, LinDivStackData');
            fclose(fid2);
        end
        if sep_save_bool == 1
            normfile_name_Separated = [pathname, 'Saved Spectra\',
newfile1, 'norm_', 'Separated.dat'];
            fid3 = fopen(normfile_name_Separated, 'w');
            fprintf(fid3,'%s\r',label);
            fprintf(fid3, F, LinDivSepData');
            fclose(fid3);
        end
    end
    % If save booleans are true, it creates column headers for the data
and then saves the specified files with the original name plus a suffix
describing the type of data. File format is .dat.
end
```

7.2.3 Chemical Mapping

```
mainDir = 'Example Directory\';
% Active directory containing sub-directories containing PEEM images

dirList = dir(mainDir); % List all subdirectories

dirCount = 0;

for kk = 1:length(dirList)
    doIT = 0; % Boolean variable to decide if directory should be
analyzed
```

```
    if length(dirList(kk).name) > 3 && isdir([mainDir,
dirList(kk).name]) % Check if variable in dirList is indeed a directory
        if dirList(kk).name(end) == 'C' % Check if directory contains
carbon movie
            % Pt_pathname = [mainDir, 'UNCD_UFL_3_C_Pt_52\'];
            Pt_pathname = [mainDir, 'ta-C_UFL_3_C_Pt_21\'];
            doIT = 1;
            % If so use carbon platinum movie as normalization, go
through with script
        elseif dirList(kk).name(end) == 'O' % Check if directory
contains oxygen movie
            % Pt_pathname = [mainDir, 'UNCD_UFL_3_O_Pt_51\'];
            Pt_pathname = [mainDir, 'Test_O_Pt\'];
            doIT = 1;
            % If so use oxygen platinum movie as normalization, do not
go through with code as current subscripts do not analyze for oxygen
spectra
        elseif dirList(kk).name(end) == 'N' % Check if directory
contains oxygen movie
            % Pt_pathname = [mainDir, 'UNCD_UFL_3_O_Pt_51\'];
            Pt_pathname = [mainDir, 'ta-C_UFL_3_O_Pt_20\'];
            doIT = 1;
            % If so use oxygen platinum movie as normalization, do not
go through with code as current subscripts do not analyze for oxygen
spectra
        end
        if doIT == 1 % If above conditions say go:
            dirCount = dirCount + 1;
            currentDirectoryPathname = [mainDir, dirList(kk).name] %
Create a path name for the current directory containing images to map
            savePrefix = dirList(kk).name(end-3:end);
            [dontuse1, Data_file, dontuse2, testing_start,
testing_stop] = loadDatFile(currentDirectoryPathname);
            % Runs the function loadDatFile.m which will extract the
energy column associated with the images. There's an alternative input
to the function where you can select what range of energies you want to
look at. If this is done, 'testing_start' and 'testing_stop' will give
indeces that relate to the first and last energy you want to look at.
            sample_tif_files = dir(fullfile(currentDirectoryPathname,
'\*.tif')); % List all .tif images in data movie folder
            Pt_tif_files = dir(fullfile(Pt_pathname, '\*.tif')); % List
all .tif images in platinum movie folder
            sample_file_name = [currentDirectoryPathname, '\',
sample_tif_files(1).name]; % Create a variable concatenating the path
name with the first .tif image
            S = double(imread(sample_file_name)); % Load in the image
and call it variable 'S'
            [L1,L2] = size(S); % Find the size of the image
            cutUpSize = 400;
            xFull = floor(L2/cutUpSize);
            yFull = floor(L1/cutUpSize);
            xOver = mod(L2,cutUpSize);
            yOver = mod(L1,cutUpSize);
            if xOver > (cutUpSize/2)
                totalX = xFull + 1;
```

```
            else
                totalX = xFull;
            end
            if yOver > (cutUpSize/2)
                totalY = yFull + 1;
            else
                totalY = yFull;
            end
            % This is that section I talked about that defines a square
size to partition pieces of the images for separate analysis, and
generated depending on cutUpSize.
            dataNorm = zeros(L1,L2);
            ptNorm = zeros(L1,L2);

            index1 = find(Data_file(:,1)>=Data_file(1,1)+1.5,1);
            index2 = find(Data_file(:,1)>=Data_file(1,1)+5,1);

            avgCounter = 0;
            for ii = index1:index2
                sample_file_name = [currentDirectoryPathname, '\',
sample_tif_files(ii).name]; % Same protocol as above, but now looped
for all images
                S = double(imread(sample_file_name)); % Read the
indexed data movie image as 'S'
                Pt_file_name = [Pt_pathname, '\',
Pt_tif_files(ii).name]; % Same as for data, but now for platinum
                P = double(imread(Pt_file_name)); % Read the indexed
platinum movie image as 'P'
                if size(S) == size(P)
                    avgCounter = avgCounter + 1;
                    dataNorm = dataNorm + S;
                    ptNorm = ptNorm + P;
                else
                    [L4,L5] = size(P);
                    if L1 > L4
                        too_long = L1 - L4;
                        start_top = 1;
                        for jj = 1:too_long
                            if start_top == 1
                                P = vertcat(P(1,:),P);
                                start_top = 0;
                            elseif start_top == 0
                                P = vertcat(P,P(length(P),:));
                                start_top = 1;
                            end
                        end
                    elseif L1 < L4
                        too_long = L4 - L1;
                        start_top = 1;
                        for jj = 1:too_long
                            if start_top == 1
                                P(1,:) = [];
                                start_top = 0;
                            elseif start_top == 0
                                P(length(P),:) = [];
```

```
                                start_top = 1;
                            end
                        end
                    end
                    % The above if-statement simply corrects the
platinum image if it is not the same size as the data by either adding
copied rows to the top or bottom (alternating) or removing rows in the
same manner
                    avgCounter = avgCounter + 1;
                    dataNorm = dataNorm + S;
                    ptNorm = ptNorm + P;
                end
            end
            % Same section that creates the normalization images for
the  sample and platinum images.

            if ~isempty(find(dataNorm<=0,1))
                dataNorm(find(dataNorm<=0)) = 1;
            end
            if ~isempty(find(ptNorm<=0,1)) > 0
                ptNorm(find(ptNorm<=0)) = 1;
            end

            dataNorm = dataNorm ./ avgCounter;
            ptNorm = ptNorm ./ avgCounter;

            try
                warning off
                mkdir([currentDirectoryPathname, '\PDFs'])
            catch
            end

            A = zeros(L1,L2);
            B = zeros(L1,L2);
            C = zeros(L1,L2);
            D = zeros(L1,L2);
            E = zeros(L1,L2);
            % A-D or A-E will be used to store the reassembled pieces
of the finished chemical map.

            counter = 0;
            for qq = 1:xFull
                for rr = 1:yFull
                    counter = counter + 1;
                    if qq < xFull && rr < yFull
                        x1 = (qq-1)*cutUpSize+1;
                        x2 = qq*cutUpSize;
                        y1 = (rr-1)*cutUpSize+1;
                        y2 = rr*cutUpSize;
                    elseif qq < xFull && rr == yFull
                        x1 = (qq-1)*cutUpSize+1;
                        x2 = qq*cutUpSize;
                        y1 = (rr-1)*cutUpSize+1;
                        y2 = L1;
```

```
                    elseif qq == xFull && rr < yFull
                        x1 = (qq-1)*cutUpSize+1;
                        x2 = L2;
                        y1 = (rr-1)*cutUpSize+1;
                        y2 = rr*cutUpSize;
                    elseif (qq == xFull) && (rr == yFull)
                        x1 = (qq-1)*cutUpSize+1;
                        x2 = L2;
                        y1 = (rr-1)*cutUpSize+1;
                        y2 = L1;
                    end
                    % Determine range of index values for current piece
of the image to analyze.

                    dataSubset = NaN(y2-y1+1,x2-x1+1,testing_stop-
testing_start+1);
                    % Re-null the variable holding the current piece of
the movie, which should have dimensions (cutUpSize, cutUpSize,
testing_stop-testing_start+1).
                    for mm = testing_start:testing_stop
                        sample_file_name = [currentDirectoryPathname,
'\', sample_tif_files(mm).name]; % Same protocol as above, but now
looped for all images
                        S = double(imread(sample_file_name)); % Read
the indexed data movie image as 'S'
                        Pt_file_name = [Pt_pathname, '\',
Pt_tif_files(mm).name]; % Same as for data, but now for platinum
                        P = double(imread(Pt_file_name)); % Read the
indexed platinum movie image as 'P'
                        normImages = (S./dataNorm)./(P./ptNorm); % If
the same size, index-wise divide the matrices and assign to the correct
location in 'Norm_images'
                        dataSubset(:,:,mm) = normImages(y1:y2,x1:x2);
                    end
                    % Loads each image from the data and platinum,
performs image normalization, and then saves the piece to dataSubset.

                    [chemicalMapPiece, map_type] =
spectraManipulation2(dataSubset, Data_file, currentDirectoryPathname);
                    % Run spectraManipulation2.m subscript that will
extract information from the images and generate chemicalMapPiece
structure with map_type 1 being carbon, 2 being oxygen

                    if map_type == 1
                        A(y1:y2,x1:x2) = chemicalMapPiece.cM1;
                        B(y1:y2,x1:x2) = chemicalMapPiece.cM2;
                        C(y1:y2,x1:x2) = chemicalMapPiece.cM3;
                        D(y1:y2,x1:x2) = chemicalMapPiece.cM4;
                        E(y1:y2,x1:x2) = chemicalMapPiece.cM5;
                    elseif map_type == 2
                        A(y1:y2,x1:x2) = chemicalMapPiece.cM1;
                        B(y1:y2,x1:x2) = chemicalMapPiece.cM2;
                        C(y1:y2,x1:x2) = chemicalMapPiece.cM3;
                        D(y1:y2,x1:x2) = chemicalMapPiece.cM4;
                    end
```

```
                    % Once the subset has been created, analyzed,
the piece is put in the correct position of the final matrix (A-E or A-
D, depending on element).
                end
            end

            if map_type == 1
                Sp2_name = [currentDirectoryPathname, '\', savePrefix,
'_Sp2Frac'];
                Ratio_name = [currentDirectoryPathname, '\',
savePrefix, '_CRatio'];
                Pi_name = [currentDirectoryPathname, '\', savePrefix,
'_CPi'];
                Sigma_name = [currentDirectoryPathname, '\',
savePrefix, '_CSigma'];
                Area_name = [currentDirectoryPathname, '\', savePrefix,
'_CArea'];
                save(Sp2_name, 'A', '-ASCII');
                save(Ratio_name, 'B', '-ASCII');
                save(Pi_name, 'C', '-ASCII');
                save(Sigma_name, 'D', '-ASCII');
                save(Area_name, 'E', '-ASCII');
            elseif map_type == 2
                oxyPiM_name = [currentDirectoryPathname, '\',
savePrefix, '_OPi'];
                oxySigM_name = [currentDirectoryPathname, '\',
savePrefix, '_OSigma'];
                Ratio_name = [currentDirectoryPathname, '\',
savePrefix, '_ORatio'];
                Area_name = [currentDirectoryPathname, '\', savePrefix,
'_OArea'];
                save(oxyPiM_name, 'A', '-ASCII');
                save(oxySigM_name, 'B', '-ASCII');
                save(Ratio_name, 'C', '-ASCII');
                save(Area_name, 'D', '-ASCII');
            end
            % Save chemical maps with appropriate name to folder
containing .tif images
        end
    end
end
```

7.2.4 Subscripts

```
function [C,index1,index2] =
derivative(file_name,energy_step,index_energy_1,index_energy_2)

A = file_name;

[L1,L2] = size(A);

[tf, index1] = findValInd(A, index_energy_1);
[tf, index2] = findValInd(A, index_energy_2);
```

```
deriv_range = int32(0.2/energy_step);

for i = index1:index2
    imin = i - deriv_range;
    imax = i + deriv_range;
    B = polyFitPlus(A(imin:imax, 1), A(imin:imax, 2), 1);
    C(i-index1+1) = B(1,1);
    clear B
end


function [value, index] = findValInd(mat_in, value, col_sel)

if nargin == 2
    col_sel = 1;
end

range_val = mat_in(2,col_sel)-mat_in(1,col_sel);


if value > max(mat_in(:,col_sel))
    index = length(mat_in(:,col_sel));
    value = mat_in(index,col_sel);
else
    index = find(mat_in(:,col_sel) >= (value-0.05*range_val),1);
    value = mat_in(index,col_sel);
end


function [A, x_range, y_range, I] = heightHeaderLoad(fullname)

fid = fopen(fullname,'r');

line_read = fgetl(fid);

if line_read(1) ~= '#' && line_read(1) ~= 'Z' && line_read(1) ~= '\'
    A = load(fullname);
    I = [];
    x_range = 0;
    y_range = 0;

    simple_text = 1;

    fclose(fid);
else
    fid = fopen(fullname,'r');

    line_read = fgetl(fid);

    if line_read(1) == '#'
        header_read_done = 0;
```

```
        while header_read_done ~= 1

            if line_read(1:7) == '# x-pix'
                line_length = length(line_read);
                x_pixels_num = str2num(line_read(14:line_length));
                x = int32(x_pixels_num);
            end

            if line_read(1:7) == '# y-pix'
                line_length = length(line_read);
                y_pixels_num = str2num(line_read(14:line_length));
                y = int32(y_pixels_num);
            end

            if line_read(1:7) == '# x-len'
                line_length = length(line_read);
                x_range = str2num(line_read(14:line_length))/1000;
            end

            if line_read(1:7) == '# y-len'
                line_length = length(line_read);
                y_range = str2num(line_read(14:line_length))/1000;
                header_read_done = 1;
            end
            line_read = fgetl(fid);
        end

        count = 0;
        while count < y
            line_read = fgetl(fid);
            first_symbol = line_read(1);
            if first_symbol ~= '#'
                count = count + 1;
                k = textscan(line_read, '%n', 'delimiter', ' ');
                A(count,1:x) = k{1};
            end
        end
        I = [];

    elseif line_read(1:4) == 'Zygo'

        for ii = 1:7
            line_read = fgetl(fid);
        end

        space_loc = regexp(line_read, ' ');
        intfScaleFactor =
str2num(line_read(space_loc(1)+1:space_loc(2)-1));
        wavelengthIn = str2num(line_read(space_loc(2)+1:space_loc(3)-
1));
        obliquityFactor =
str2num(line_read(space_loc(4)+1:space_loc(5)-1));
```

```
        cameraRes = str2num(line_read(space_loc(6)+1:space_loc(7)-
1))*10^6;

        line_read = fgetl(fid);

        space_loc = regexp(line_read, ' ');
        x_width = str2num(line_read(1:space_loc(1)-1));
        y_height = str2num(line_read(space_loc(1)+1:space_loc(2)-1));

        x_range = x_width*cameraRes;
        y_range = y_height*cameraRes;

        for ii = 1:2
            line_read = fgetl(fid);
        end

        phaseRes = str2num(line_read(1));
        if phaseRes == 0;
            R = 4096;
        else
            R = 32768;
        end

        for ii = 1:4
            line_read = fgetl(fid);
        end

        line_read = ' ';
        row_count = 1;

        C = zeros(ceil(x_width*y_height/10),10);

        while line_read(1) ~= '#'
            line_read = fgetl(fid);

            if line_read(1) ~= '#'
                k = textscan(line_read, '%n', 'delimiter', ' ');
                C(row_count,:) = k{1};
                row_count = row_count + 1;
            end
        end

        B = reshape(C',x_width,y_height);
        I = B';

        line_read = ' ';
        row_count = 1;

        C = zeros(ceil(x_width*y_height/10),10);

        while line_read(1) ~= '#'
            line_read = fgetl(fid);
```

```
            if line_read(1) ~= '#'
                k = textscan(line_read, '%n', 'delimiter', ' ');
                C(row_count,:) = k{1};
                row_count = row_count + 1;
            end
        end

        indMax = find(C == 2147483640 | C == -2147483640);
        C(indMax) = NaN;

        B = reshape(C',x_width,y_height);
        A = B';
        A = A.*(intfScaleFactor*obliquityFactor*wavelengthIn/R)*10^9;

    elseif line_read(1:4) == '\'

        for ii = 1:7
            line_read = fgetl(fid);
        end

        space_loc = regexp(line_read, ' ');
        intfScaleFactor =
str2num(line_read(space_loc(1)+1:space_loc(2)-1));
        wavelengthIn = str2num(line_read(space_loc(2)+1:space_loc(3)-
1));
        obliquityFactor =
str2num(line_read(space_loc(4)+1:space_loc(5)-1));

        cameraRes = str2num(line_read(space_loc(6)+1:space_loc(7)-
1))*10^6;

        line_read = fgetl(fid);

        space_loc = regexp(line_read, ' ');
        x_width = str2num(line_read(1:space_loc(1)-1));
        y_height = str2num(line_read(space_loc(1)+1:space_loc(2)-1));

        x_range = x_width*cameraRes;
        y_range = y_height*cameraRes;

        for ii = 1:2
            line_read = fgetl(fid);
        end

        phaseRes = str2num(line_read(1));
        if phaseRes == 0;
            R = 4096;
        else
            R = 32768;
        end

        for ii = 1:4
```

```
            line_read = fgetl(fid);
        end

        line_read = ' ';
        row_count = 1;

        C = zeros(ceil(x_width*y_height/10),10);

        while line_read(1) ~= '#'
            line_read = fgetl(fid);

            if line_read(1) ~= '#'
                k = textscan(line_read, '%n', 'delimiter', ' ');
                C(row_count,:) = k{1};
                row_count = row_count + 1;
            end
        end

        B = reshape(C',x_width,y_height);
        I = B';

        line_read = ' ';
        row_count = 1;

        C = zeros(ceil(x_width*y_height/10),10);

        while line_read(1) ~= '#'
            line_read = fgetl(fid);

            if line_read(1) ~= '#'
                k = textscan(line_read, '%n', 'delimiter', ' ');
                C(row_count,:) = k{1};
                row_count = row_count + 1;
            end
        end

        indMax = find(C == 2147483640 | C == -2147483640);
        C(indMax) = NaN;

        B = reshape(C',x_width,y_height);
        A = B';
        A = A.*(intfScaleFactor*obliquityFactor*wavelengthIn/R)*10^9;
    end

    fclose(fid);

end


function [InterpData, L3, L4, energy_step] = interpolate(RawData,
energy_step)
```

```
if nargin == 1
    energy_step = 0.02;
end

dupCheck = diff(RawData(:,1));
dupIndex = find(dupCheck == 0);
if ~isempty(dupIndex)
    RawData(dupIndex,:) = [];
end

[L1,L2]= size(RawData); % Ascertain the size of the inputted data
matrix.

if RawData(1,1) > RawData(2,1) % Checks to make sure that the energy
column runs from low to high, and swaps it if it doesn't.
    for i = 1:L1
        RawDatasub(i,:) = RawData(L1+1-i,:);
    end
    RawData = RawDatasub;
end

NewData(:,1) = round(10*RawData(:,1))/10; % This rounds the energy
column of the data to the ones place.

it_run = int32((NewData(L1,1) - NewData(1,1))/energy_step + 1);

InterpData = zeros(it_run,L2);

InterpData(:,1) = [NewData(1,1):energy_step:NewData(L1,1)];

InterpData(:,2:L2) =
interp1(RawData(:,1),RawData(:,2:L2),InterpData(:,1),'linear','extrap')
;

[L3,L4] = size(InterpData);


function [A] = loadWithHeader(file_name_data)

fid1 = fopen(file_name_data,'r');

header = 0;
no_header = 0;
while header ~= 1
    line_read = fgetl(fid1);
    line_read_E = str2num(line_read(1));
    if line_read(1) ~= 'E'
        A = load(file_name_data);
        header = 1;
        no_header = 1;
    end
    header = 1;
end
```

```
first_symbol = 1;

if no_header ~= 1
    count = 0;
    while first_symbol ~= -1
        line_read = fgetl(fid1);
        first_symbol = line_read(1);
        if (first_symbol ~= 'E') && (first_symbol ~= -1)
            count = count + 1;
            k = textscan(line_read, '%n', 'delimiter', ' ');
            A(count,:) = k{1};
        end
    end
end

fclose(fid1);


function [real_peak_pos, sp2ratio, pistarratio, real_peak_hgt] =
main(data, matOrFile)

if matOrFile == 1
    D = data;
else
    [D] = loadWithHeader(data);
end

if D(2,1)-D(1,1) > 0.1
    [Y, L1, L2, energy_step] = interpolate(D);
else
    Y = D;
    [L1,L2] = size(Y);
end

[not_used, index1] = findValInd(Y, 283);
[not_used, index2] = findValInd(Y, 287);

ii = index1+9;

peaks_found = []; %First row is peak energy, second is peak height,
third is intensity at the lower min, fourth is intensity at the upper
min
peaks_counter = 0;
while ii < index2 - 10
    ii = ii + 1;

    if Y(ii,2) > max(Y(ii-10:ii-1,2)) && Y(ii,2) > max(Y(ii+1:ii+10,2))
        peaks_counter = peaks_counter + 1;

        peaks_found(1,peaks_counter) = Y(ii,1);
        peaks_found(2,peaks_counter) = Y(ii,2);
        peaks_found(3,peaks_counter) = min(Y(ii-5:ii-1,2));
```

```
        peaks_found(4,peaks_counter) = min(Y(ii+1:ii+5,2));
        peaks_found(5,peaks_counter) = Y(ii-3,1);
        peaks_found(6,peaks_counter) = Y(ii+3,1);

        for jj = ii-6:-5:index1
            if min(Y(jj-4:jj,2)) < peaks_found(3,peaks_counter)
                peaks_found(3,peaks_counter) = min(Y(jj-4:jj,2));
                peaks_found(5,peaks_counter) = Y(jj-2,1);
            else
                break
            end
        end

        for kk = ii+6:5:index2
            if min(Y(kk:kk+4,2)) < peaks_found(4,peaks_counter)
                peaks_found(4,peaks_counter) = min(Y(kk:kk+4,2));
                peaks_found(6,peaks_counter) = Y(kk+2,1);
            else
                break
            end
        end
    end
end

intensity_mins = min(peaks_found(3:4,:));
peak_diffs = abs(peaks_found(2,:)-intensity_mins);

peak_diffs_mean = mean(peak_diffs);
peak_diffs_std = std(peak_diffs);

outliers = find(peak_diffs < (peak_diffs_mean - 3*peak_diffs_std));

peaks_found(:,outliers) = [];

[not_used, p_start] = findValInd(Y, peaks_found(5,1));
[not_used, p_end] = findValInd(Y, peaks_found(6,1));

[not_used, real_peak_energy, not_used] =
gaussAndCauchyFit(Y(p_start:p_end,1),Y(p_start:p_end,2));

[real_peak_hgt, real_peak_pos] = findValInd(Y,real_peak_energy);

mid_index = p_end;

for k = 2:L2

    x1 = Y(1:mid_index,1);
    y1 = Y(1:mid_index,k);

    [maxy, max_index] = max(y1);

    x_shift = x1-x1(max_index);
```

```
    [sigma, mu, Amp]=gaussAndCauchyFit(x_shift,y1);

    pistararea = Amp * sigma * (2*pi) ^ (1/2); % Exact area from
calculus

    [sigmaarea] = riemannSum(Y,288.6,325);

    data_ratio(k-1) = pistararea / sigmaarea(k-1);

end

if Y(L1,1) >= 325
    graphite_factor = 17.3324;
else
    [graphite_factor] = graphitePiSigmaRatio(Y(L1,1));
end

pistarratio = data_ratio;

sp2ratio = graphite_factor * data_ratio;


function [integrals] = riemannSum(A,StartE,StopE)

[L1,L2] = size(A);

[not_used, ind_start] = findValInd(A, StartE);
[not_used, ind_stop] = findValInd(A, StopE);

for jj = 2:L2
    integrals(jj-1) = sum(A(ind_start:ind_stop-1,jj) +
0.5*diff(A(ind_start:ind_stop,jj)))*(A(ind_start+1,1)-A(ind_start,1));
end


function [B] = smooth(A)

[L1,L2] = size(A);
B = A;

smooth_halfrange = 20;

P = [];

for i = 2:L1-1
    if i - smooth_halfrange < 1
        imin = 1;
        imax = i + smooth_halfrange;
    elseif i + smooth_halfrange > L1
        imin = i - smooth_halfrange;
        imax = L1;
```

```
    else
        imin = i - smooth_halfrange;
        imax = i + smooth_halfrange;
    end

    P = [[A(imin:i-1, 1); A(i+1:imax, 1)].^2 [A(imin:i-1, 1);
A(i+1:imax, 1)] ones(size([A(imin:i-1, 1); A(i+1:imax, 1)]))];
    p = P\[A(imin:i-1, 2); A(i+1:imax, 2)];

    B(i,2) = p(1)*A(i,1)^2+p(2)*A(i,1)+p(3);
end
```